UNIVERSITY OF CALIFORNIA SAN DIEGO

High-Quality Photon Pair Generation in Silicon Photonic Microring and Its Applications

A dissertation submitted in partial satisfaction of the requirements
for the degree Doctor of Philosophy

in

Electrical Engineering (Photonics)

by

Chaoxuan Ma

Committee in charge:

Professor Shayan Mookherjea, Chair
Professor Julio T. Barreiro
Professor Leonid V. Butov
Professor Joseph Ford
Professor George C. Papen

2020

The Dissertation of Chaoxuan Ma is approved, and it is acceptable in quality and form for publication on microfilm and electronically:

_____

_____

_____

_____

_____

Chair

University of California San Diego

2020

DEDICATION

To my significant other who unfolded a brand-new horizon for my life and career.

This work is also dedicated to my parents who have been a loving and supportive company all the time.

EPIGRAPH

靡不有初，鲜克有终。

—《诗经·大雅·荡》

TABLE OF CONTENTS

LIST OF FIGURES

LIST OF TABLES

LIST OF ABBREVIATIONS

Abbreviation	Definition
ASE	Amplified spontaneous emission
CAR	Coincidences-to-accidentals ratio
CMOS	Complementary metal–oxide–semiconductor
CROW	Coupled-resonator optical waveguide
CW	Continuous wave
DBR	Distributed Bragg reflector
DLI	Delay-line interferometer
FCA	Free carrier absorption
FCD	Free carrier dispersion
FSR	Free spectral range
FWHM	Full-width at half maximum
GVD	Group velocity dispersion
HBT	Hanbury-Brown-Twiss
HOM	Hong-Ou-Mandel
MZI	Mach-Zehnder interferometer
NIC	Network interface card
NRZ	Non-return-to-zero
PGR	Pair generation rate
PPLN	Periodically poled lithium niobate
QD	Quantum dot
Q-factor	Quality-factor
QIP	Quantum information processing
QKD	Quantum key distribution
ROADM	Reconfigurable optical add-drop multiplexer
SFWM	Spontaneous four wave mixing
SNSPD	Superconducting nanowire single photon detector
SOI	Silicon-on-insulator
SPAD	Single photon avalanche diode
SPD	Single photon detector
SPDC	Spontaneous parametric down conversion
SPM	Self-phase modulation
TDC	Time-to-digital converter
TE	Transverse electric
TEC	Thermo-electric controller
TIA	Time interval analyzer
TPA	Two photon absorption
UMZI	Unbalanced Mach-Zehnder interferometer

ACKNOWLEDGEMENTS

I would like to thank my advisor, Prof. Shayan Mookherjea, for his generous encouragement and guidance in my pursuit of PhD research. Along this journey, Shayan has been always supportive with his extraordinary expertise in this field and beyond, and genuine in exchanging valuable life experience. Specifically, I would like to express my appreciation for his time spent with us in experiments and discussions, and the high standards he sets to keep us motivated.

My sincere thanks also go to all my labmates: Mr. Forrest Valdez, Mr. Xiaoxi (Josh) Wang, Dr. Peter Weigel, and Ms. Jie Zhao. It is a pleasure to work with each of you. Particularly, I thank Josh for being the most reliable work partner and collaborator. He is always swift in response and ready to help. Without these, I would have missed the delight from teamwork and my works will never be realized. I also thank Jie for sharing my emotions, with all those lovely conversations, about food, gossips, fashion, news and everything else. I cherish the opportunity to work with her on the SPDC experiments and wish her best luck in her remaining PhD program and future career.

I acknowledge all our group partners for their support. I thank Dr. Anthony Lentine and Sandia National Laboratory for their fabrication shuttle runs to realize our design ideas. I thank Intel Labs for providing their hybrid laser. I thank the national science foundation for the financial support of our projects. And most particularly, I would like to express my gratitude to Dr. Vikas Anant for providing the state-of-the-art superconducting nanowire single photon detectors and his prompt support, without which our works would not be possibly demonstrated as successfully.

To my dear parents, I definitely owe you a debt. You missed a lot of time others would have normally enjoyed with their children. But still, you provided unconditional support and caring all the time.

Songyan, thank you. It has been really a long long journey and I feel so fortunate to have you by my side all along the way. Thank you for making it warm and loving when it’s raining dogs and cats.

Thank you for having my back when the path seems to be leading nowhere. Deep there, you are driving me to work hard so that I can proudly say, I deserve you.

Finally, I would like to extend my deepest gratitude to my country, China. Thank you for all the generous educational resources that defines how good I can be, and the rich spirits and cultures that shapes who I am. This is a critical and hard time for all our people, and it is also this time that have convinced me more than anything else that we will come out stronger. Thousands of miles away, my heart is always with you.

Thanks,

Chaoxuan Ma

Sunnyvale, CA

Feb. 24, 2020

Chapter 2 contains the material submitted for publication as it may appear in the following of which the dissertation author was the primary investigator: Chaoxuan Ma, Shayan Mookherjea. "Prospects for photon-pair generation using silicon microring resonators with two photon absorption and free carrier absorption."

Chapter 3 contains the material as it appears in the following of which the dissertation author was the primary investigator: Chaoxuan Ma, Xiaoxi Wang, Vikas Anant, Andrew D. Beyer, Matthew D. Shaw, and Shayan Mookherjea. "Silicon photonic entangled photon-pair and heralded single photon generation with CAR > 12,000 and $g^{(2)}(0) < 0006$." Optics Express 25, no. 26 (2017): 32995-33006.

Chapter 4 contains material as it appears in the following of which the dissertation author was the secondary investigator: Xiaoxi Wang, Chaoxuan Ma, Ranjeet Kumar, Pierre Doussiere, Richard Jones, Haisheng Rong, and Shayan Mookherjea. "Photon pair generation using a silicon photonic hybrid

laser." APL Photonics 3, no. 10 (2018): 106104; Xiaoxi Wang, Chaoxuan Ma, Ranjeet Kumar, Pierre Doussiere, Richard Jones, Haisheng Rong, and Shayan Mookherjea. "Photon pair generation using silicon photonic microring and hybrid laser." In CLEO: Applications and Technology, pp. JTh5C-6. Optical Society of America, 2017.

Section 5.1 of Chapter 5 contains the material as it appears in the following of which the dissertation author was the primary investigator: Chaoxuan Ma, Xiaoxi Wang, and Shayan Mookherjea. "Photon-pair and heralded single photon generation initiated by a fraction of a 10 Gbps data stream." Optics express 26, no. 18 (2018): 22904-22915.

Section 5.2 of Chapter 5 contains the material as it appears in the following of which the dissertation author was the primary investigator: Chaoxuan Ma, and Shayan Mookherjea. "Simultaneous dual-band entangled photon pair generation using a silicon photonic microring resonator." Quantum Science and Technology 3, no. 3 (2018): 034001.

Chapter 6, in full, has been submitted for publication of the material as it may appear in the following of which the dissertation author was the primary investigator: Chaoxuan Ma, Xiaoxi Wang, Shayan Mookherjea. “Progress towards a widely-usable integrated silicon photonic photon-pair source.”

VITA

2014	B.Eng.	Zhejiang University, Hangzhou, China
2016	M.A.Sc.	University of Toronto, Toronto, Canada
2020	Ph.D.	University of California San Diego, La Jolla, US

DOCTORAL RESEARCH PUBLICATIONS

C. Ma, and S. Mookherjea, “Prospects for photon-pair generation using silicon microring resonators with two photon absorption and free carrier absorption.”, 2020 (submitted).

C. Ma, Xiaoxi Wang and S. Mookherjea, “Progress towards a widely-usable integrated silicon photonic photon-pair source.”, 2020 (submitted).

C. Ma, X. Wang, and S. Mookherjea. "Photon-pair and heralded single photon generation initiated by a fraction of a 10 Gbps data stream." Optics Express 26.18: 22904-22915, 2018.

C. Ma and S. Mookherjea. "Simultaneous dual-band entangled photon pair generation using a silicon photonic microring resonator." Quantum Science and Technology 3.3: 034001, 2018.

C. Ma, M. Jere, X. Wang, and S. Mookherjea. "High CAR and low $g^{(2)}(0)$ of 1.55 m entangled photon-pairs generated by a silicon microring resonator." 2018 Conference on Lasers and Electro-Optics (CLEO). paper FTh1G.4, 2018.

C. Ma, X. Wang, V. Anant, A. D. Beyer, M. D. Shaw, and S. Mookherjea. "Silicon Photonic Entangled Photon-Pair and Heralded Single Photon Generation with CAR >12,000 and $g^{(2)}(0)$ <0.006." Optics Express 25.26: 32995-33006, 2017.

J. Zhao, C. Ma, M. Rsing, and S. Mookherjea. "Entangled photon-pair generation in periodically-poled thin-film lithium niobate waveguides." arXiv preprint arXiv:1910.03202, 2019.

J. Zhao, C. Ma, M. Ruesing and S. Mookherjea "High-quality photon-pair and heralded single-photon generation using periodically-poled thin-film lithium niobite." in Frontiers in Optics postdeadline paper FTu6A.3 (2019).

X. Wang, C. Ma, R. Kumar, P. Doussiere, R. Jones, H. Rong, and S. Mookherjea, "Photon pair generation using a silicon photonic hybrid laser." APL Photonics 3.10: 106104, 2018.

X. Wang, C. Ma, R. Kumar, P. Doussiere, R. Jones, H. Rong and S. Mookherjea, "Photon Pair Generation Using Silicon Photonic Microring and Hybrid Laser" CLEO 2017 Proceedings of the Conference on Lasers and Electrooptics, JTh5C.6, 2017. (postdeadline)

PRE-DOCTORAL RESEARCH PUBLICATIONS

C. Ma, W. D. Sacher, Z. Tang, J. C. Mikkelsen, Y. Yang, F. Xu, T. Thiessen, H.-K. Lo, and J. K. S. Poon. "Silicon photonic transmitter for polarization-encoded quantum key distribution." Optica, 3(11): 1274-1278, 2016.

W. D. Sacher, Z. Yong, J. C. Mikkelsen, A. Bois, Y. Yang, J. C. C. Mak, P. Dumais, D. Goodwill, C. Ma, J. Jeong, E. Bernier, and J. K. S. Poon. "Multilayer silicon nitride-on-silicon integrated photonic platform for 3D photonic circuits." CLEO 2016 Proceedings of the Conference on Lasers and Electro-optics, JTh4C.3, 2016. (postdeadline)

ABSTRACT OF THE DISSERTATION

High-Quality Photon Pair Generation in Silicon Photonic Microring and Its Applications

by

Chaoxuan Ma

Doctor of Philosophy in Electrical Engineering (Photonics)

University of California San Diego, 2020

Professor Shayan Mookherjea, Chair

Compact, efficient, high-quality and scalable non-classical photon sources are one of the most critical building blocks for quantum information processing and communications. Photon pair generation via spontaneous four wave mixing is being recognized as an attractive platform for quantum optics which is compatible with the rapidly-maturing classical integrated photonics technology using silicon wafers, which is adopted in industry for its low cost, high performance and scalability. Traditionally, the photon pairs generated from silicon photonic devices, however, have not compared favorably with traditional nonlinear crystals in terms of overall rate, quality and efficiency. This dissertation discusses the factors that affect the quality and efficiency of photon pair generation in silicon integrated photonic microrings, together with their design and characterization. Furthermore, we show

how the microrings can be integrated with other photonic devices on the silicon-on-insulator platform, and using proof-of-concept experiments, discuss the feasibility of using these photon-pair sources with technology that is already present in, or will soon be present in, practical fiber-optic networks, such as integrated lasers and modulated classical data streams.

Chapter 1
Introduction

On October 23, 2019, Google announced a demonstration that their quantum computer had completed a test calculation in 200 seconds which would cost the most powerful classical supercomputer 10,000 years [1]. A heated debate was ignited on whether quantum supremacy had been achieved [2]. Nevertheless, it seems likely that quantum information science has finally come to the spotlight and the pioneering efforts of basic-science researchers during the past two decades are now joined by applied scientists and engineers, governments [3–6] and businesses [7] hoping to exploit an immense potential to revolutionize the fields of computation, communication, simulation, sensing and metrology.

Similar to a classical "bit", quantum information processing (QIP) uses a qubit, or quantum bit, as the basic unit of quantum information. There have already been many physical realizations of qubit, such as trapped ions [8–11] and atoms [12–15], quantum dots (QD) [16–18] , superconducting circuits [19,20], defects [21] and photons [22–24]. While matter-based systems are most popular in industrial demonstrations of quantum computing, they require milli-Kelvin temperature or high vacuum to minimize matter-environment interactions to avoid decoherence issues. Photons, on the other hand, have very weak interactions with transparent materials and among themselves, therefore do not depend harsh environmental requirements. Better still, photons possess multiple degrees of freedom for information encoding: polarization, path, time-bin, etc., which can be easily and finely manipulated.

With scalability and integrability, integrated photonic circuits are ideal platforms for these QIP applications. Current quantum photonic technologies mainly focus on quantum computation and communication for the profound economic and national security values. A relatively high integrability for both applications has been demonstrated on chip [25–27]. Unfortunately, none of them has a true integrated single photon source, which pumps, generates and processes the single photons entirely on chip. Ideally, a true single photon source emits one photon every time it is triggered, have a high repetition rate. It may

require single mode operation, long coherence time, high indistinguishability between photons and purity of states, depending on actual applications. In this chapter, we will look through the available single photon generation technologies and show why photon pair generation in silicon photonic microrings might have a fair chance in the competition.

1.1 Figures of Merit

1.1.1 General

Generation Rate / Source Efficiency / Brightness

Generation rate might be the most relevant feature of a light source, and is defined as the number of photons/ photon pairs generated per second. A lot of works report generation rate in source, which reveals the maximum potential of photon rates a light source can deliver, while others report the overall generation rate that accounts for photon extraction, propagation loss and detector efficiency, which is what actually delivers to the final application. For photon pair sources, pair generation rate (PGR) in source can be calculated as

$$\mathrm{PGR} = \frac{R_s R_i}{C_{si}} \tag{1.1}$$

where $R_s$and R_i are detected singles rates for signal and idler photons, and C_{si} is the detected coincidence rates between the two channels.

While generation rate might be more relevant to continuous wave (CW) sources, source efficiency characterizes a pulsed source in a more straightforward way. It is defined as the probability of generating more than one photon per pulse, which can be calculated as, in the limit of low multi-photon emission probability: $\eta_{\mathrm{source}} = R/f_{\mathrm{pump}}$ (R is the photon emission rate and f_{pump} is the repetition rate of pump).

Another related parameter is the brightness, i.e., photon count rate per unit pump power per unit frequency bandwidth ($\mathrm{cps/nm/mW}$ or $\mathrm{cps/GHz/mW}$). In some of the sources [25,28,29], the photon generation rate is proportional to the square of pump power due to the nature of the physical processes,

hence the unit of the brightness becomes $\mathrm{cps/nm/\ mW^2}$ or $\mathrm{cps/GHz/\ mW^2}$ accordingly. This feature is important since many applications requires highly indistinguishable [30] or involves strong interaction with atoms or molecules [13,31] or includes components that are only functional in a limited bandwidth, thus a high rate of photon generation into a narrow bandwidth is essential.

Second-Order Correlation Function

The second-order correlation function is the main feature to determine how "single photon" a light source is. The second order correlation function between mode i at location $\boldsymbol{r}_1$, time t and mode j at location $\boldsymbol{r}_2$, time $t+\tau$ can be expressed as

$$g^2(\boldsymbol{r}_1,t;\boldsymbol{r}_2,t+\tau)=\frac{\langle E_i^*(\boldsymbol{r}_1,t)E_j^*(\boldsymbol{r}_2,t+\tau)E_j(\boldsymbol{r}_2,t+\tau)E_i(\boldsymbol{r}_1,t)\rangle}{\langle E_i^*(\boldsymbol{r}_1,t)E_i(\boldsymbol{r}_1,t)\rangle\langle E_j^*(\boldsymbol{r}_2,t+\tau)E_j(\boldsymbol{r}_2,t+\tau)\rangle} \tag{1.2}$$

For a single-mode CW light source and two equivalent measurement spots, $g^2(\tau)$ can be written in a more compact form:

$$g^2(\tau)=\frac{\langle \hat{a}^\dagger(t)\hat{a}^\dagger(t+\tau)\hat{a}(t+\tau)\hat{a}(t)\rangle}{\langle \hat{a}^\dagger(t)\hat{a}(t)\rangle^2} \tag{1.3}$$

At the special case of $\tau=0$, it can be further simplified as:

$$g^2(0)=\frac{\langle \hat{n}(t)(\hat{n}(t)-1)\rangle}{\langle \hat{n}(t)\rangle^2} \tag{1.4}$$

Figure 1.1(a) shows the basic setup to measure $g^2(\tau)$, which is called Hanbury-Brown-Twiss (HBT) interferometer [32]. Photons incident on a beamsplitter randomly choose one of the two outputs to exit and detected by single photon detectors (SPDs). The intervals between the photon arrival times of the two outputs are recorded by a time interval analyzer (TIA) or time tagger. A histogram of the time intervals $\mathrm{K}(\tau)$ is then formed to show the distribution and can be converted to $g^2(\tau)$ after proper normalization:

$$g^2(\tau)=\frac{N_{\mathrm{AB}}(\tau;\Delta\tau)}{R_{\mathrm{A}}R_{\mathrm{B}}T\Delta\tau} \tag{1.5}$$

Where N_{AB} is the total coincidences detected by the TIA, $\Delta\tau$ is the time bin of the histogram and T is the total integration time.

In most cases, $g^2(0)$ can be used to distinguish a single photon, anti-bunching source from a classical one. For a perfectly anti-bunching source, there is no possibility that two photons arrive at the same time, thus $g^2(0) = 0$; for a coherent source whose arrival time interval between two consecutive photons is completely random, thus $g^2(0) = 1$; For thermal sources where photons tend to bunch together, $g^2(0) > 1$ [33].

For photon pair sources, since the sense of "single photon" is on the condition of heralding, this definition has been adapted as heralded second-order correlation function $g^2_{\mathrm{H}}(\tau)$. The measurement setup is shown in Figure 1.1(b). Due to the complexity of acquiring the whole function, usually the zero-delay value is calculated as

$$g^2_{\mathrm{H}}(0) = \frac{C_{\mathrm{ABC}} R_{\mathrm{C}}}{C_{\mathrm{AC}} C_{\mathrm{BC}}} \tag{1.6}$$

Where C_{ABC} denotes the triple coincidence rate of heralding and two heralded outputs, R_C stands for the heralding count rate, C_{AC} and C_{BC} are the coincidence rates between heralding and each heralded output respectively.

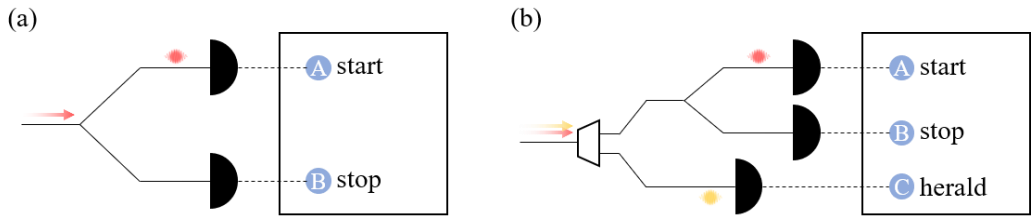

Figure 1.1 (a) HBT interferometer setup to measure the second order correlation function $g^2(\tau)$. Photons enters the beamsplitter and exit from one of the outputs. The photons then are detected by an SPD and the time interval between the arrivals of two consecutive photons are recorded by a TIA and forms a histogram. For an ideal single photon source, no coincidence will be recorded for $\tau = 0$. (b) Setup to measure the heralded second-order correlation function $g^2_{\mathrm{H}}(\tau)$ for photon pair sources.

Purity and Indistinguishability

purity evaluates how pure a quantum state is since quantum states can exist as superposition of mixed states. While the density matrix of a pure quantum state can be expressed as $\hat{\rho}_{\text{pure}} = |\varphi\rangle\langle\varphi|$, a mixed state is a linear superposition of pure states $\hat{\rho}_{\text{mixed}} = \sum \rho_i |\varphi_{\text{i}}\rangle\langle\varphi_{\text{i}}|$. The purity of a quantum state can be quantified as

$$\text{P} = \text{Tr}\{\hat{\rho}^2\} \tag{1.7}$$

where $\hat{\rho}$ is the state density matrix. A pure state has a purity of 1, while that of a mixed state is less than 1, with a lower limit of 1/N, where N is the dimension of the Hilbert space.

Many applications, such as long-range quantum communication [34–36] and linear-optic quantum computing [26,30], involves quantum interference of two consecutive photons or those from separate sources, thus require photons to be indistinguishable. The indistinguishability between two states, whose density matrices are $\hat{\rho}_1$ and $\hat{\rho}_2$, can be expressed as

$$I(\hat{\rho}_1, \hat{\rho}_2) = 1 - \frac{1}{2}\|\hat{\rho}_1 - \hat{\rho}_2\|^2 \tag{1.8}$$

In quantum mechanics, two quantum states are indistinguishable when their density matrices are identical, thus the indistinguishability has a maximum of 1. For pure states $\hat{\rho}_1 = |\psi_1\rangle\langle\psi_1|$ and $\hat{\rho}_2 = |\psi_2\rangle\langle\psi_2|$, the indistinguishability becomes $I(\hat{\rho}_1, \hat{\rho}_2) = |\langle\psi_1|\psi_2\rangle|^2$ [37,38]. Indistinguishability is typically characterized by Hong-Ou-Mandel (HOM) interference [39], as shown in Figure 1.2. If the two photons incident on the two inputs of a beamsplitter is indistinguishable, then quantum interference transforms the input states as

$$|1\rangle_1|1\rangle_2 \rightarrow (R-T)|1\rangle_1|1\rangle_2 + i\sqrt{2RT}|2\rangle_1|0\rangle_2 + i\sqrt{2RT}|0\rangle_1|2\rangle_2 \tag{1.9}$$

where R and T are the reflectivity and transmissivity of the beamsplitter. For an ideal beamsplitter where $R = T = 0.5$, the two photons always exit from the same output, hence no coincidence recorded by the detectors. In order to measure the visibility of the interference, the time delay τ_{12} between the two input

photons will be scanned and you obtain coincidences as a function of τ_{12}. In practice, the setup is usually adapted to simplify the measurement for both pulsed [40,41] and CW [42]-excited photon sources. The visibility of the interference is related to the indistinguishability as [37]

$$V_{HOM} = \mathrm{Tr}\{\hat{\rho}_1\hat{\rho}_2\} = \frac{\mathrm{Tr}\{\hat{\rho}_1^2\} + \mathrm{Tr}\{\hat{\rho}_2^2\} - \|\hat{\rho}_1 - \hat{\rho}_2\|^2}{2} \tag{1.10}$$

Therefore

$$V_{HOM} \leq I(\hat{\rho}_1, \hat{\rho}_2) \tag{1.11}$$

And the two sides are only equal when the input states $\hat{\rho}_1$ and $\hat{\rho}_2$ are pure states. It should also be noted that when the indistinguishability is guaranteed ($\hat{\rho}_1 = \hat{\rho}_2$), V_{HOM} is equal to the purity of the state.

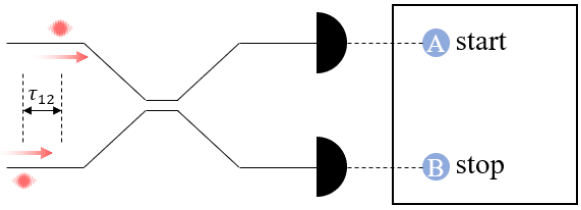

Figure 1.2 HOM interference setup. If the two photons entering the beamsplitter are indistinguishable (also in temporal mode), they always exit at the same output, hence no coincidence at the detection side.

Entanglement

A particularly unique feature in quantum mechanics is quantum entanglement, where two or more quantum states are correlated and cannot be decided independently. A measurement of one quantum state will affect the state of the other instantaneously. Such entangled states are an important resource for quantum key distribution (QKD) and communications protocols [34,43–47], quantum repeaters [35], quantum memories [31,48,49], and schemes for quantum computation [50–53] . Photons can be entangled in many dimensions, such as polarization [34,44,49] and time-bin [28,43,48], which makes photons an ideal candidate for entangled sources. The most used is polarization entangled photon pairs, as polarization of

photons can be conveniently manipulated and measured. The degree of polarization entanglement between the twin photons are usually proved by measuring their density matrix via quantum state tomography.

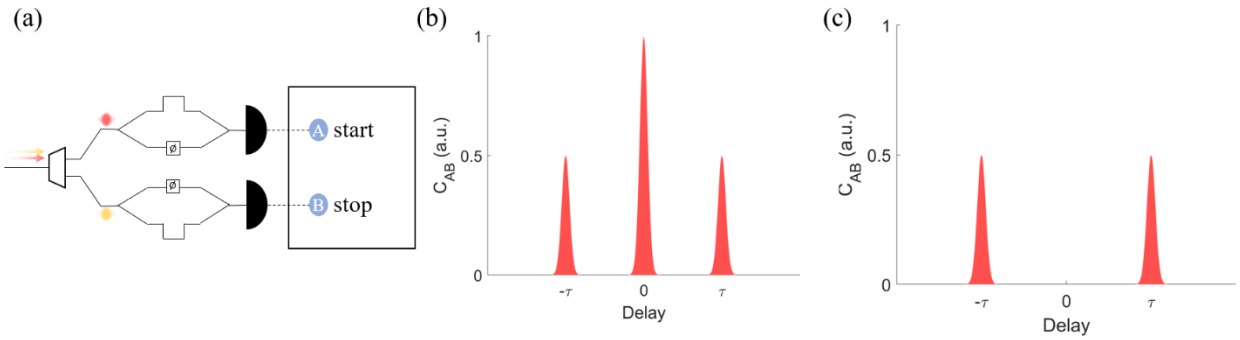

Figure 1.3 (a) Franson interferometer for time-energy entanglement measurement. Both photons in a pair has 50% chance of entering short and long path. The probabilistic amplitudes of $|s,s\rangle$ and $|l,l\rangle$ interfere at zero delay, which forms a coincidence peak with a height corresponding to the sum of phase on each UMZI's arm. (b) There will be three peaks on the histogram. The first and third peaks are formed when the two photons do not arrive together (one takes the short path and the other takes the long path). The central peak is formed by the interference of states $|s,s\rangle$ and $|l,l\rangle$. This figure shows the constructive interference. (c) Destructive interference of the states $|s,s\rangle$ and $|l,l\rangle$.

Another common choice, time-energy entanglement, is measured by two-photon Franson interference [54] as shown in Figure 1.3(a). The signal and idler photons enter each unbalanced Mach-Zehnder interferometer (UMZI). Each photon has 50% chance of entering the short and long paths respectively. Therefore, there are four combinations of the paths the photons will take: $|s,s\rangle$, $|l,l\rangle$, $|s,l\rangle$, $|l,s\rangle$, where s means the short path and l the long path. In the histogram for time intervals between the twin photons, as shown in Figure 1.3(b), there will be three peaks: the first from $|l,s\rangle$, the last from $|s,l\rangle$, and the central peak from states $|s,s\rangle$ and $|l,l\rangle$. The probabilistic amplitudes of $|s,s\rangle$ and $|l,l\rangle$ then interfere with each other on the conditions that the path difference between the arms of UMZI is shorter than the photons coherent length. On the other hand, for it to be measurable, the path difference should be long enough for the three peaks to resolve, since the timing jitter brings a width to the coincidence peaks and they may overlap if the path difference is too short. The number of coincidences in the middle time slot (corresponds to states $|s,s\rangle$ and $|l,l\rangle$), will be a function of the sum of phase on both UMZIs, which forms an interference fringe and its visibility quantifies the degree of time-energy entanglement of photons. A

coincidence fringe visibility higher than 71%, which violates the Bell inequality [54,55], is sufficient to prove the entanglement of the state.

1.1.2 Photon Pair Specific

Coincidences-to-Accidentals Ratio

For photon pair sources, the coincidences-to-accidentals ratio (CAR) is the quantum optical version of signal-to-noise ratio of classical signal. Since SPDs sometimes randomly click without the actual detection of photons (dark counts), there are "accidental" coincidence counts which do not reflect the generation of photon pairs at the source. They can be distinguished from the true coincidences by an analysis of the temporal distribution of such events, which differs substantially from that of the true coincidence counts. Such accidental coincidences might also form because of a coincidence between broken pairs, i.e., one of the "truly paired" photons is lost in propagation or non-unity detection efficiency, and a coincidence is instead detected by the electronics with another photon that happens to be delayed from the original pair by only a short time delay. The probability of such events increases as the detection time window is increased. Furthermore, added optical noise (photons) from the pump's amplified spontaneous emission (ASE) also can generate accidental coincidence counts, since the detectors are wavelength-agnostic, within a certain optical passband (at least several nanometers or tens of nanometers of wavelength wide). All these accidentals are unwanted "noise" that contaminates the real coincidences, and thus, a figure of merit, CAR, is defined as

$$\mathrm{CAR} = \frac{C_{\mathrm{cc}} - C_{\mathrm{acc}}}{C_{\mathrm{acc}}} \tag{1.12}$$

where C_{cc} and C_{acc} are the raw detected coincidences and accidental coincidences, which can be calculated as

$$C_{\mathrm{cc}} = R_{\mathrm{pair}}\eta_{\mathrm{i}}\eta_{\mathrm{s}} \tag{1.13}$$

$$C_{acc} = \Delta\tau\left[\left(R_{\mathrm{i}} + R_{\mathrm{n,i}}\right)\eta_{\mathrm{i}} + D_i\right]\left[\left(R_{\mathrm{s}} + R_{\mathrm{n,s}}\right)\eta_{\mathrm{s}} + D_s\right] \tag{1.14}$$

Here, R_{pair} is the extracted photon pair rate immediately after the source; R_{i} (R_{s}) is the extracted idler (signal) photon rate out of the source; η_{i} (η_{s}) is the channel efficiency for the idler (signal) photons, which may include the channel propagation loss and detector efficiency; D_{i} and D_{s} are the detectors dark count rates. If we compare Eq. (1.5) and Eq. (1.12)-(1.14), we can find that $g^2_{\mathrm{si}}(0) = 1 + \mathrm{CAR}$. In the limit of $g^2_{\mathrm{si}} \gg 1$, $g^2_{\mathrm{si}}(0) \approx \mathrm{CAR}$.

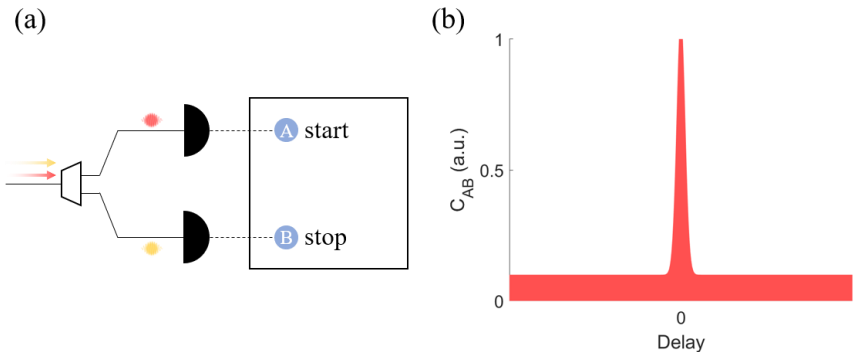

Figure 1.4 (a) CAR measurement setup. The photon pair is demuxed and each is detected by an SPD. The time intervals between the two channels consecutive photon arrivals are recorded by a TIA and binned into a histogram. (b) The histogram showing the distribution between two consecutive photons' arrival times. For photons from a single pair, since they are generated simultaneously, the delay should be zero. With enough photon pairs, a peak will rise at zero delay, whose width corresponds to the timing jitter of detectors. At the same time, accidental counts are random, and form a background floor in the histogram.

Figure 1.4(a) shows a typical experimental setup for measurement of CAR. The time intervals between the clicks of the two detectors are binned into a histogram, where, as the measurement progresses with time, a peak in the coincidence counts will rise above the noise floor at the time bin which corresponds to the time delay between the arrival time of the two photons. The histogram floor is lifted by accidental coincidences, as shown in Figure 1.4(b). In practice, the peak has a width which corresponds to the timing jitter of the detectors, but is sometimes masked by the larger, minimum bin-resolution of some time-to-digital converters (TDCs) (e.g., the quTAU module has a minimum bin width of 81 ps, which is significantly larger than the timing jitter of typical NbN superconducting nanowire single photon detectors (SNSPDs), 20-30 ps full-width at half-maximum (FWHM)).

Heralding Efficiency

Heralding efficiency, or Klyshko efficiency, is defined as the probability of detecting another photon in the pair on the condition of heralding, which can be given as

$$\eta_{\mathrm{h}} = \frac{C_{\mathrm{cc}} - C_{\mathrm{acc}}}{R_{\mathrm{h}}} \tag{1.15}$$

where R_{h} is the heralding rate. Although signal and idler photons are always generated together, several things must happen in sequence for the heralded photon to be detected. First, the herald photon has to be extracted out of the source. Second, the herald photon needs to survive the propagation loss between the source and detector. a high chip-to-fiber (or chip-to-free space) loss results in most photons being lost at this stage. Third, the SPD has a less-than-unity detection efficiency [InGaAs single photon avalanche diodes (SPADs) are significantly worse than SNSPDs at telecommunications wavelengths]. Therefore, the heralding efficiency, or Klyshko efficiency, can be calculated as

$$\eta_{\mathrm{h}} = \eta_{\mathrm{P}}\eta_{\mathrm{opt}}\eta_{\mathrm{det}} \tag{1.16}$$

where η_{P} is the preparation or extraction efficiency from the source, η_{opt} is the transmission loss between source and η_{det} is the detection efficiency of the SPD. In addition, there can be other factors, such as the reset time of the detector after a photon detection event occurs, following which the detection event does not immediately recover, but only gradually does so, following a build-up curve that can last several tens of nanoseconds for superconducting SPDs. InGaAs SPADs are operated with a hold-off of tens of microseconds in order to reduce the probability of after-pulsing. These effects can cause a rate-dependent detection efficiency.

1.2 Types of Single Photon Sources

Ideally, a single photon sources should emit exactly one photon on demand and its emission rate can satisfy the applications requirements. The photons are emitted into a well-defined mode, which can be ~~are~~ easy to collect into a fiber or waveguide and deliver to the intended destination e.g., an interferometer or a detector. There are many realizations of single photon sources, which can be generally divided into two categories: probabilistic and deterministic.

1.2.1 Weak Laser Pulses

The earliest single photon sources are emulated by weak laser pulses, which are attenuated to an average of single-photon level in each pulse (usually < 0.1 to suppress multi-photon emission). Light emitted from a stable single-mode laser can be well approximated by a coherent state

$$|\alpha\rangle = e^{-\frac{|\alpha|^2}{2}} \sum_{n=0}^{\infty} \frac{\alpha^n}{\sqrt{n!}} |n\rangle \tag{1.17}$$

And the photon number in each pulse follow the Poisson distribution

$$P(n) = \frac{e^{-\mu}\mu^n}{n!} \tag{1.18}$$

where μ is the mean photon number per pulse. Despite a pseudo single photon source, it is still widely used in many practical demonstrations of quantum communication links [36,56] and commercial systems [57,58] due to its reliability, high repetition rate, economical cost and easy operation.

1.2.2 Deterministic Sources

Deterministic sources emit one single photon at a time. There are two categories of these sources: single emitter and ensemble-based systems. In these systems, single photons are generated when individual particles or ensemble systems transition between energy states, which ensures no more than one photon can be produced at one time. Single emitters use single particles, such as atoms [59–62], ions [62–64],

molecules [65,66], color centers [67–70] and QDs [71–73]. While these sources are closer to ideal single photon sources, they require more complicated preparation schemes and stringent environmental requirements compared with other photon sources: (1) It is critical for most single emitter systems to ensure that only one particle is trapped as to avoid multiphoton emission; (2) The generation process or tests of photons in systems, like atoms [59–62], ions [62–64] , QDs [71,72] and molecules [65,66], involve harsh conditions like cryogenic temperatures; (3) While the nature does an extraordinary job of making natural particles like atoms, ions and molecules identical, man-made QDs and color centers are not exactly the same, which degrades the indistinguishability of photons and limits the scalability of systems; (4) Unless strongly coupled to a cavity, the spatial mode of these systems are poorly defined, which results in a low collection efficiency. Unfortunately, it is inherently difficult for some systems like charged particles to do so; (5) Limited trapping times of atoms and atomic motion in an ensembled system [74,75] makes it hard to obtain highly coherent photons, which is critical for many applications.

It is also important to note that deterministic sources do not guarantee a unit probability of emitting single photon at every trigger. There are a number of mechanisms: transitions that trap the particles in a nonradiative state, non-unity collection efficiency and detection efficiency. Thus the "deterministic" sources become probabilistic.

1.2.3 Photo Pair Sources

Photon pairs are arguably the most practical sources for entangled photons, which are essential for many applications like quantum communications [34,35,43,48,76,77] and quantum computing [22]. Photon pairs are typically generated from nonlinear crystals through spontaneous parametric down conversion (SPDC) [29,78–81] or spontaneous four wave mixing (SFWM) [25,28,82,83] in a probabilistic manner. Despite the probabilistic nature of their photon statistics, the two photons in a pair are always generated simultaneously thus can be used as a heralded photon source [76] (one of the daughter photons is used to herald the arrival of the other). Another approach is to use photonic cascades from atoms [77,84] or QDs [85–87], which generates photon pairs in a "deterministic" way (i.e., no more than one photon pair

is generated at a time). But this approach is still in an early development stage and not yet ready for practical applications.

SPDC is the standard nonlinear process used to generate photon pairs, which relies on the $\chi^{(2)}$ nonlinear materials such as KDP [37,88] , BBO [80,81,89,90], lithium niobite ($LiNbO_3$) [29,78,79,91,92]. In this nonlinear processes, one pump photons annihilate and give birth to two daughter photons at degenerate or non-degenerate frequencies under the conservation of energy ($\omega_p = \omega_i + \omega_s$) and momentum ($\vec{k}_p = \vec{k}_i + \vec{k}_s$). One of the disadvantages of SPDC is that it is hard to engineer the dispersion property of the materials, thus the wavelengths of the photons are restricted by the material property except for very limited control from temperature. To overcome the drawback, researchers have come up with an approach called "periodic poling" [93], which periodically inverts the polarity of crystal domain to achieve quasi-phase matching between pump photons and generated photon pairs. This method allows the flexibility to tailor the wavelengths of photon pairs.

Recent years has seen a growing interest in SFWM ($\chi^{(3)}$ nonlinear process) which can be optically excited in silica (dispersion shifted fibers [94], photonic crystals fibers [95]), silicon [25,28,83] and silicon nitride [82]. In SFWM, two pump photons annihilate and produce two daughter photons under the conservation of energy ($2\omega_p = \omega_i + \omega_s$) and momentum $2\vec{k}_p = \vec{k}_i + \vec{k}_s$. The theory model of SFWM is discussed in Chapter 2 . The media of SFWM, however, provides a convenient platform to collect and transport photon pairs in optical networks and integrated photonic circuits [27,47].

Waveguide devices have been extensively used to generate photon pairs via SPDC and SFWM. The process benefits from the devices in the various aspects: (1) Waveguide devices are much more compact than bulk crystals and fibers, thus enables scalability of photon sources; (2) Waveguides can be engineered to support single mode operation, which improves the indistinguishability, purity and factorability of the states. A single spatial mode also improves the collection efficiency of photons compared with those bulky nonlinear crystals where photons are typically generated in multimode cones;

(3) Dispersion of the waveguides can be engineered by varying waveguide dimensions, hence more flexibility in the selection of photon wavelengths; (4) Optical modes have a much smaller effective mode area, which greatly enhances the effective nonlinear coefficient

$$\gamma = \frac{2\pi n_2}{\lambda_{\mathrm{p}} A_{\mathrm{eff}}} \tag{1.19}$$

This is a determinant of generation efficiency of photons, which is affected by the nonlinear refractive index n_2, pump wavelength λ_{p}, and optical effective mode area A_{eff}. A simple waveguide, however, has a broad emission spectral span (typically from one to tens of nanometers) which lacks brightness, coherence and purity. To circumvent this problem, it is straightforward to use a very narrow bandpass filter. The resulting spectrum of photons, however, is then subject to availability of these narrowband filters with a low insertion loss. Commercial narrowband filters typically have a bandwidth ranging from 0.1 to several nanometers, with the disadvantages of high cost and limited scalability. On-chip integrated filters might be another option. However, the feature of narrowband never comes as a free meal but usually at an expense of higher insertion loss. Another approach to achieve narrow bandwidth of photons is to build the nonlinear crystal into a relatively high-Q micro-cavity [25,82,83]. Spectrally, the photon pairs modes need to overlap with the cavity modes to be generated. Thus the cavity itself is serving as a narrowband filter, which, if properly designed, usually gives a smaller bandwidth than filters. In addition, the pump intensity is significantly enhanced in the cavity through resonance, which results in a much stronger nonlinear process.

Given that, silicon integrated photonics has seen a good opportunity to implement the photon pair source. Except for all its well-known advantages such as complementary metal–oxide–semiconductor (CMOS) compatibility, low-cost, integrability and scalability, silicon has a very strong $\chi^{(3)}$ nonlinearity as a material. The large index difference between silicon and its native oxide (SiO_2) provides a strong confinement of the optical mode, which results in a very high nonlinear coefficient. Not to mention its large device library thanks to the extensive research in the past two decades, which facilitates the transport and

manipulation of the photons. Long waveguides can be easily and compactly realized on the silicon-on-insulator (SOI) platform [27,96,97], which is transparent in the fiber-optic telecommunication bands of 1310 nm and 1550 nm. As a result, the photons can be efficiently collected by fibers and transmitted in the optical networks. Silicon photonic devices can be integrated with lasers [98], detectors [99] and micro-electronics for future integrated systems. To achieve narrowband photons, silicon photonic resonators can be engineered to achieve a very high quality factor (Q-factor) and a compact footprint [25,83]. The microring provides simultaneous resonances for all three frequencies (pump, signal and idler wavelengths) across adjacent free-spectral ranges with a tight constraint on the narrow bandwidth dictated by the high Q-factor resonance, which improves the generation rate substantially compared with a long silicon waveguide. There are two common types of resonators on this platform: microdisks and microrings. A microdisk usually consists of a disk sitting on a pedestal and coupled to a fiber. The fiber-resonator positioning challenges of the undercut microdisk structure [83] suggest that the microring device may be easier to package and use practically. On the other hand, the approach of [83] also presents an opportunity to optimize the resonator coupling coefficient for a particular application, e.g., improving heralding efficiency insitu, which is not possible in microrings.

Table 1.1 Comparison of single photon sources.

	Statistics	Pump	T (K)	λ (nm)	R_p	BW	η_e[a]	$g^2(0)$[b]	CAR	V_{HOM}[c]	V_F	Refs
WCP	P	-	300	vis-MIR	GHz	GHz	< 0.1[d]	1	-	1	-	-
Single emitter												
Single atom (^{85}Rb) in cavity	D	O	≈ 0	780	100 kHz	10 MHz	0.0406	0.0277	-	-	-	[59]
Single atom (^{87}Rb) in cavity	D	O	≈ 0	795 (780)	10 kHz	5.6 MHz	0.34 (0.56)	-	-	0.64	-	[60]
Single atom (Cs) in cavity	D	O	≈ 0	852.4	100 kHz	8.4 MHz	0.024	0.0018	-	-		[61]
Single ion ($^{138}Ba^+$)	D	O	≈ 0	493	200 kHz	-	0.0556	0.0019	-	-	-	[62]
Single ion ($^{40}Ca^+$) in cavity	D	O	≈ 0	866	10 MHz	2.4 MHz	0.08	1.6×10^{-7}				[64]
Single ion ($^{40}Ca^+$) in cavity	D	O	≈ 0	866	2.4 kHz	0.108 MHz	0.88	3.3×10^{-8}				[63]
Single molecule (DBT[e])	D	O	3	785.6	50 MHz	< 100 MHz	0.48	0.08	-		-	[65]
Single molecule (ZnPc) in cavity	D	E	8	653.9	-	32.9 THz	0.003/e	0.12				[66]
QD (InGaAs)	D	O	4	926.7	82 MHz	-	0.325	0.024	-	0.78 (M)	-	[71]
	D	O	4	926.7	82 MHz	-	0.16	0.0028	-	0.9956 (M)	-	
QD (InAs)	D	O	5	915.2	76 MHz	-	0.72	< 0.008	-	-		[72]
QD (GaN)	D	O	300	291.6	80 MHz	8.71 THz	0.0063	0.13	-	-	-	[73]
Color centers (SiV)	D	O	300	738	CW	2.75 THz	370 kHz/mW	0.7	-	-	-	[70]
Color center (NV)	D	O	4	637	10 MHz	< 100 MHz	0.46	0.24	-	-	-	[67]
Ensemble												
Rb	D	O	300	780	4.1 GHz	1.7 GHz	0.04	0.21	-	-	-	[75]
Photon pairs												
SPDC												
PPLN (waveguide)	P	O	300	1310	CW	87.4 GHz	26.2 MHz/mW	-	-	0.99	0.99	[78]
PPLN (thin film)	P	O	300	1550	CW	97.5 GHz	44 MHz/mW	0.044	6000	-	-	[29]
AlN (microring)	P	O	300	1550	CW	1.1 GHz	5.8 MHz/mW	0.088	300	-	-	[79]
SFWM												
Si (Waveguide)	P	O	300	1550	100 MHz	-	0.04 (0.0013)	-	20 (200)		0.96	[28]
Si (Microring)	P	O	300	1550	CW	3.75 GHz	149 MHz/mW^2	0.11 (0.0053)	12105 (532)		0.98	[25]
Si_3N_4 (Microring)	P	O	300	1550	CW	445 MHz	0.52 MHz/mW^2	-	3780[f]		0.98	[82]

R_p: pumping rate; BW: bandwidth; η_e: emission efficiency; V_F: Franson interference visibility.

[a] The emission efficiency excludes propagation loss and non-unity detection efficiency
[b] For photon pair sources, it's $g_H^2(0)$
[c] The indistinguishability is represented by modal overlap if denoted by "M", otherwise HOM visibility.
[d] For laser pulses with an average photon number below 0.1
[e] DBT: dibenzoterrylene
[f] Highest CAR achieved with a photon pair detection rate of 1200 cps.

1.3 Organization of the Dissertation

The dissertation discusses the design and capability of a silicon photonic microring resonator to produce high-quality single photon pairs, and their integrability and potential in practical applications. The dissertation is organized as follows: Chapter 2 revisits the current theory model of SFWM in photonic microring resonators and discusses its limitations. A new model was established to include the impacts of more factors, e.g. two photon absorption (TPA) and free carrier absorption (FCA) and thermo-optic effects. The capability and the limits on the quality of photon pairs generated by silicon photonic microrings are then investigated. Chapter 3 shows the demonstration of using a silicon photonic microring to generate record-high quality photon pairs with high brightness, high CAR and low $g^2(0)$. Chapter 4 demonstrates the feasibility of integrating silicon photonic microring photon pair source with an on-chip hybrid silicon laser. Chapter 5 presents proof-of-principle demonstrations of using the photon pair source in optical networks with technologies such as demultiplexing of 1310 nm and 1550 nm telecom bands and pumping with modulated classical data streams. Chapter 6 reports on significant progress towards the ultimate goal of a fully integrated silicon microchip for generating entangled photons with multiple stages of tunable optical filtering on the same chip as the pair generation resonator.

Chapter 2
Photon-Pair Generation with Two Photon Absorption and Free Carrier Absorption

Photon pair generation in silicon microring resonators using the process of SFWM is being recognized as an attractive platform for quantum optics and quantum communications using information encoded onto single photons [100–102]. From a technology viewpoint, these devices are compatible with the classical integrated photonics technology fabricated on large-area silicon wafers, which is being rapidly adopted in industry for its low cost, high performance and scalability. However, it has been known from the early days of silicon photonics that, at higher levels of pump powers, especially in the CW regime, silicon photonic devices suffer from not only thermally-induced spectral shifts (which can be compensated by feedback-stabilization to the laser) but also nonlinear impairments such as nonlinear TPA and FCA, which cannot be eliminated, even with carrier sweepout schemes [103,104].

The process of SFWM is itself a nonlinear optical process; however, the "nonlinearity" that is referred to in this chapter is a specific regime of operation that, at the modest levels of pump powers that are typically required for photon-pair generation, is more often encountered in silicon micro-resonator devices. In silicon waveguides, the optical effective mode area A_{eff}, is typically in the range of 100 – 200 W.m^{-1} [105–107], which is inversely proportional to the effective nonlinearity as defined in Eq. (1.19). A simple waveguide, however, has a broad emission spectral span (typically from one to tens of nanometers) [108,109] which lacks brightness, coherence and purity, unless followed by a narrow bandpass filter. The resulting spectrum of photons, however, is then subject to availability of these narrowband filters with a low insertion loss. Narrowband filters typically have a bandwidth ranging from 0.1 to several nanometers, with the disadvantages of high cost and limited scalability [110,111].

In contrast to waveguides, integrated micro-resonators incorporate the nonlinear segment into a relatively high-Q micro-cavity, thus greatly increasing the nonlinear interaction length between the pump,

signal and idler frequencies without increasing the device footprint on the chip [112,113]. Spectrally, the pump and photon-pair modes need to match with the cavity modes; however, very stringent dispersion engineering is not required in typical silicon waveguides around the wavelength of 1550 nm since the group index of refraction is approximately constant, and all the wavelengths are fairly close to each other.

Obviously, the pump intensity is significantly enhanced through resonance, which results in a much stronger nonlinear process. Moreover, the cavity itself serves as a narrowband filter, which, if properly designed, can operate with a smaller bandwidth than external filters, since no "margin" needs to be reserved to keep separate structures aligned through experimental temperature fluctuations. This integrated approach can result in a substantial increase in the overall brightness of pair generation, but the locally-increased intensity of the pump beam, as seen by the silicon material, leads to a number of different physical phenomena brought into play, which result in easily-visible characteristics of the (high pump-power induced) nonlinear regime [114].

In the following sections, we will model the SFWM process with a continuous-wave pump beam, which models a number of recent experimental reports [115–119]. In contrast, waveguide SFWM or SPDC experiments typically shape the pump beam into ultrashort pulses, in order to match the very wide phase-matching bandwidth. For SFWM in silicon microresonators with a fairly narrow passband, pulse widths less than about 50 ps are rarely required, and thus, the CW (or quasi-CW) regime is a useful analytical and numerical approximation to help elucidate the complicated dynamics in the high-power regime.

The pair generation rate (R) in photonic resonators under CW pumping can be calculated by using the following equation [113]:

$$R = \Delta v[\gamma P^{\mathrm{res}} L_{\mathrm{eff}}^{\mathrm{res}}]^2 \mathrm{sinc}^2\left(\beta_2 \Delta\omega^2 \frac{L^{\mathrm{res}}}{2} + \gamma P^{\mathrm{res}} L_{\mathrm{eff}}^{\mathrm{res}}\right) \tag{2.1}$$

where Δv is the FWHM of the ring resonance, γ is the effective waveguide nonlinearity, β_2 is the group velocity dispersion (GVD) coefficient of the waveguide at pump wavelength, $\Delta\omega$ is the pump-signal (idler)

angular frequency separation, P^{res}, L^{res} and $L_{\mathrm{eff}}^{\mathrm{res}}$ resonantly enhanced parameters when unfolding the resonator to an equivalent waveguide:

$$P^{\mathrm{res}}(\lambda) = P_0 \times \frac{1-r^2}{(1-ra)^2} \times \frac{\left(\frac{\lambda_{\mathrm{p}}}{2Q}\right)^2}{\left(\lambda-\lambda_{\mathrm{p}}\right)^2 + \left(\frac{\lambda_{\mathrm{p}}}{2Q}\right)^2} \tag{2.2}$$

$$L^{\mathrm{res}} = L \times \frac{F}{\pi} \tag{2.3}$$

$$L_{\mathrm{eff}}^{\mathrm{res}} = \frac{1-e^{-\alpha L}}{\alpha} \times \frac{F}{\pi} \tag{2.4}$$

Where P_0 is the input pump power in the access waveguide, λ_{p} is the pump wavelength and α is the waveguide propagation loss of the pump, F and Q are the finesse and Q-factor of the resonator. For an all-pass resonator, we have

$$F = \frac{\pi\sqrt{ra}}{1-ra} \tag{2.5}$$

$$Q = \frac{\pi n_{\mathrm{g}} L\sqrt{ra}}{\lambda_{\mathrm{res}}(1-ra)} \tag{2.6}$$

where r is the (amplitude) self-coupling coefficient, $a = \exp(-\alpha L/2)$ is the amplitude round-trip transmission of the cavity, n_{g} is the group index of refraction of the waveguide.

2.1 Photon-Pair Generation and Nonlinear Impairments

In practice, however, Eq. (2.1) does not include all the factors that affects photon pair generation in a resonator cavity. Since these resonators [25,83,120] are usually designed to have a high Q-factor ($\sim 1\times10^4 - 1\times10^5$) in order to enhance the pump power intensity and thus source efficiency, a series of linear or nonlinear processes can be induced by the high intensity in the cavity. Figure 2.1(a) shows a classical measurement of resonator (disk) spectra at different input power levels. The power was recorded

when a tunable laser was swept from short to long wavelengths. The lineshape and position of the resonance was obviously changed with the input power level. The asymmetric lineshape under the swept-wavelength scanning indicated thermal bistability, which makes the photon pair source hard to stabilize. These behaviors of the silicon microring under high input powers are a combined consequence of TPA, FCA, free carrier dispersion (FCD) and thermo-optic effects [121], which will be explained in the following sections.

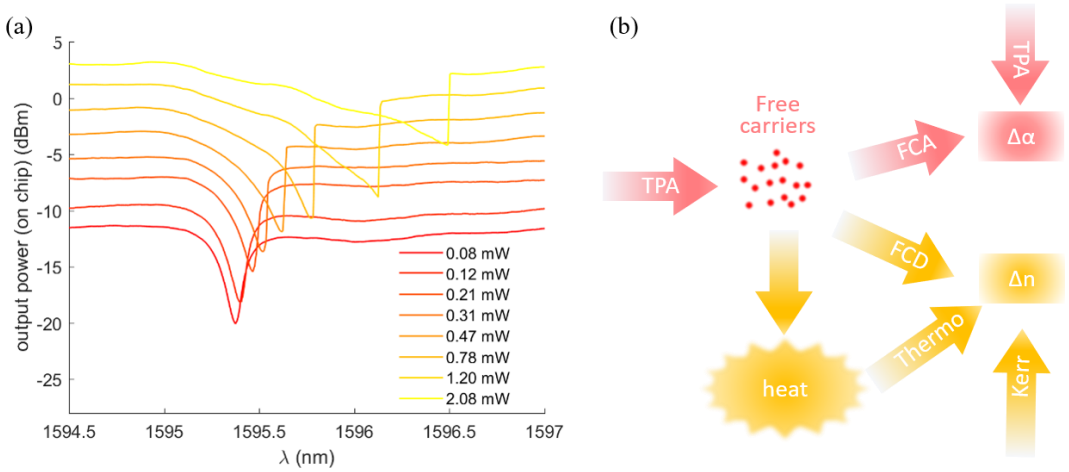

Figure 2.1 (a) Experimentally measured silicon microring resonator spectra, measured using a swept-wavelength tunable laser, at different input power levels. As the input power scales up, the resonance red shifts and extinction degrades. (b) Some of the physical processes impacting pair generation in a silicon photonic device when the pump power is high, which involves two photon absorption (TPA), free carrier absorption (FCA), free carrier dispersion (FCD) and thermo-optic effect.

2.1.1 Two Photon Absorption

The refractive index difference between silicon (the waveguide core) and silicon dioxide (cladding) provides for a strong optical mode confinement in silicon nanophotonic waveguides. The local intensity of light is further increased by the feedback effect in cavity-based devices, when the pump wavelength matches the cavity resonance. For photon pair generation, this enhancement is a boon in terms of the generation efficiency at low pump power, but has the (obvious) consequence of inducing TPA at high pump power level. TPA occurs when the sum of two input photons' energy is higher than silicon's bandgap (1.12 eV) and the local optical intensity is high, thus resulting in a high probability (per second) of optically-induced carrier excitation events across the bandgap, leading to absorption of the pump light, and typically,

generation of heat. Photons that are absorbed also generally create a free carrier, as indicated schematically in Figure 2.1(b). The strength of TPA is described by a coefficient $\beta_{\mathrm{TPA}} = [3\pi/(c\varepsilon_0\lambda\backslash n_0^2)]\mathrm{Im}\{\chi^{(3)}\}$ [122], which depends on crystal orientation and wavelength. The loss induced by TPA can be calculated as

$$\alpha_{\mathrm{TPA}} = \beta_{\mathrm{TPA}} I \tag{2.7}$$

where I is the optical intensity. In a high-confinement waveguide, the average TPA loss across the spatial variation of the mode intensity profile can be expressed as

$$\bar{\alpha}_{TPA} = \frac{\int_{Si} \beta_{TPA} I^2(\boldsymbol{r}) dA}{\int_{\infty} I(\boldsymbol{r}) dA} \approx \frac{\beta_{\mathrm{TPA}} P^{\mathrm{res}}}{A_{\mathrm{eff}}} \tag{2.8}$$

For SFWM in silicon photonic devices, TPA manifests itself as a fairly strong propagation loss of the pump power, especially when reverse-biased carrier sweepout is no longer able to extract the photo-generated carriers [123] and a significant reduction in the interaction length (i.e., number of round trips that the pump light makes in a resonator). This is rarely a beneficial effect and, intuitively, not of any benefit for SFWM. Thus, it is reasonable to suppose that SFWM in silicon micro-resonators should exclusively be performed at low optical pump powers, lest there be a steep roll-off in performance at higher pump powers [124]. However, the results shown here suggest that such intuition is only partially correct.

2.1.2 Free Carrier Absorption and Free Carrier Dispersion

Free carriers are generated by TPA and cause subsequent effects including FCA and FCD. The free carriers generated by TPA can be described by a Drude-like model [125,126]. After the carriers are generated, their spatial density profile is redistributed by diffusion. To simplify the model in our analysis here, we neglect the longitudinal diffusion of carriers along the pump propagation direction, and we only consider lateral diffusion in a waveguide cross section. The time-dependent carrier density in a silicon waveguide can be expressed as [127]

$$\frac{\mathrm{d}N}{\mathrm{d}t} = \frac{\beta_{TPA} I^2}{2h\nu} + D' \frac{\partial^2 N}{\partial^2 x} - \frac{N}{\tau_c} \tag{2.9}$$

where N is the carrier density, $h\nu$ is the photon energy, D' is the effective diffusion constant of the free carriers and τ_c is the effective carrier recombination time. For CW pumping, $\mathrm{d}N/\mathrm{d}t = 0$ and, further setting $\partial^2 N/\partial^2 x = 0$, the steady-state carrier density can be written as [128]

$$N = \frac{\beta_{TPA} I^2 \tau_0}{2h\nu} \tag{2.10}$$

These free carriers result in both a waveguide loss and a plasma dispersion effect, which is related to the induced carrier density by [125]

$$\alpha_{FC} = \frac{e^3 \lambda^2}{4\pi^2 c^2 \varepsilon_0 n} \left(\frac{\Delta N_e}{m_{ce}^2 \mu_e} + \frac{\Delta N_h}{m_{ch}^2 \mu_h} \right) = \sigma N(z,t) \tag{2.11}$$

$$\Delta n_{FC} = -\frac{e^2 \lambda^2}{8\pi^2 c^2 \varepsilon_0 n} \left(\frac{\Delta N_e}{m_{ce}} + \frac{\Delta N_h}{m_{ch}} \right) \approx -8.2 \times 10^{-22} \lambda^2 N(z,t) \tag{2.12}$$

where $\sigma \approx 1.45 \times 10^{-17} [\mathrm{cm}^2] \left(\frac{\lambda(\mathrm{nm})}{1550} \right)^2$ is the FCA cross section area. The average FCA induced loss is then calculated as

$$\bar{\alpha}_{\mathrm{FC}} = \frac{\int_{\mathrm{Si}} \sigma N(z,t) I(\boldsymbol{r}) dA}{\int_{\infty} I(\boldsymbol{r}) dA} = \frac{\sigma \beta_{TPA} \tau_0}{2h\nu} \frac{(P^{\mathrm{res}})^2}{A'_{\mathrm{eff}} A_{\mathrm{eff}}} \tag{2.13}$$

where A'_{eff} is an effective area defined as

$$A'_{\mathrm{eff}} = \frac{\int_{\infty} I(\boldsymbol{r}) dA \int_{\infty} I^2(\boldsymbol{r}) dA}{\int_{\mathrm{Si}} I^3(\boldsymbol{r}) dA} \tag{2.14}$$

2.1.3 Thermal-Optic Effect

The loss mechanisms including TPA (α_{TPA}), FCA (α_{FC}) and material absorption (α_{m}) also result in a temperature increase in silicon waveguides (and, obviously, resonators), which in turn causes an index change of the optical mode via thermo-optic effect:

$$\Delta n = \frac{\mathrm{d}n}{\mathrm{d}T}\Delta T \tag{2.15}$$

where $\mathrm{d}n/\mathrm{d}T$ for silicon is quite high (~ 2×10^{-4} K^{-1}) compared to other materials. The time-dependent temperature change induced by TPA can be expressed as

$$\frac{\mathrm{d}\Delta T}{\mathrm{d}t} = \frac{(\alpha_{\mathrm{TPA}} + \alpha_{\mathrm{FC}} + \alpha_m)I}{\rho_{\mathrm{Si}} C_{\mathrm{Si}}} - \frac{\Delta T}{\tau_{\mathrm{th}}} \tag{2.16}$$

where ρ_{Si} is silicon's mass density, C_{Si} is the specific heat capacity of silicon and τ_{th} is the heat dissipation time. For complex, multi-layer devices, computational models are being investigated which can solve for the steady-state temperature distribution efficiently [129]. Here, under CW pumping when $\mathrm{d}\Delta T/\mathrm{d}t = 0$, the temperature shift of the device is calculated using

$$\Delta T(z,t) = \frac{\tau_{\mathrm{th}}(\alpha_{\mathrm{TPA}} + \alpha_{\mathrm{FC}} + \alpha_{\mathrm{m}})}{\rho_{\mathrm{Si}} C_{\mathrm{Si}}} I(z,t) = \frac{\tau_{\mathrm{th}}(\beta_{\mathrm{TPA}} I(z,t) + \alpha_{\mathrm{FC}} + \alpha_m)}{\rho_{\mathrm{Si}} C_{\mathrm{Si}}} I(z,t) \tag{2.17}$$

2.1.4 A Numerical Model for SFWM in Microrings

The optical characteristics of the resonator cavity are driven by the input power P_0, which causes a change in the resonantly enhanced quantities: P^{res}, $L_{\mathrm{eff}}^{\mathrm{res}}$, L^{res}. A full spatio-temporal numerical solution is too complex and slow to be useful for obtaining insights. Our key simplifying assumptions are: (1) The wavelength of the pump is always positioned at the resonance (in practice, this is achieved by monitoring for the resonance); (2) The absolute change in the waveguide refractive index, which is induced by the steady state contribution of the combination of the Kerr nonlinearity, the FCD and the thermo-optic effect,

can be neglected since it can be compensated for, by an active control circuit using thermal tuning of the microring [130,131]; (3) Due to (2), the change of waveguide-cavity coupling strength is negligible; (4) For a fair comparison between sources with different bandwidths, the photon pairs will be filtered by a 1-nm (approximately 100 GHz) bandwidth optical filter (assumed to have no insertion loss) which will ensure the spectral purity of the photons. (5) Photons are transmitted in loss-free channels and detected by SPDs with a detection efficiency of 95%, comparable with state-of-the-art superconducting SPDs.

Then the total loss in the cavity is now a combination of material absorption (α_{m}), TPA (α_{TPA}) and FCA (α_{FC}):

$$\alpha_{\mathrm{total}} = -(\alpha_{\mathrm{TPA}} + \alpha_{\mathrm{FC}} + \alpha_{\mathrm{m}}) \tag{2.18}$$

According to Eq. (2.2), we have

$$P_0 = \frac{P^{\mathrm{res}}(1-ra)^2}{1-r^2} \tag{2.19}$$

Note that the round-trip amplitude transmission a is a function of P^{res}, which makes the right side of the equation to be monotonic function of P^{res}. Eq. (2.19) can be numerically solved and the cavity loss can also be determined. The photon PGR can then be calculated using Eq. (2.1), which quantifies the intra-cavity generation rate. The extracted (i.e., output) PGR also includes the extraction efficiency, i.e., the fraction of the photon pairs which are coupled out of the microring into the bus waveguide. We approximate the on-resonance extraction efficiency as [83]

$$\eta_{\mathrm{p}} = \frac{1 \pm \sqrt{T_{\mathrm{c}}}}{2} \tag{2.20}$$

where T_{c} is the transmissivity at resonance, the plus and minus signs correspond to over-coupled and under-coupled conditions. The probability of coupling both photons in a pair out of cavity is η_{p}^2. Note that the number of extracted photon pairs is less than the extracted idler or signal photons, i.e., photon pairs are

broken due to the non-unity extraction efficiency. These photons remaining out of broken pairs may later contribute to the accidental coincidences if they propagate all the way to the SPDs.

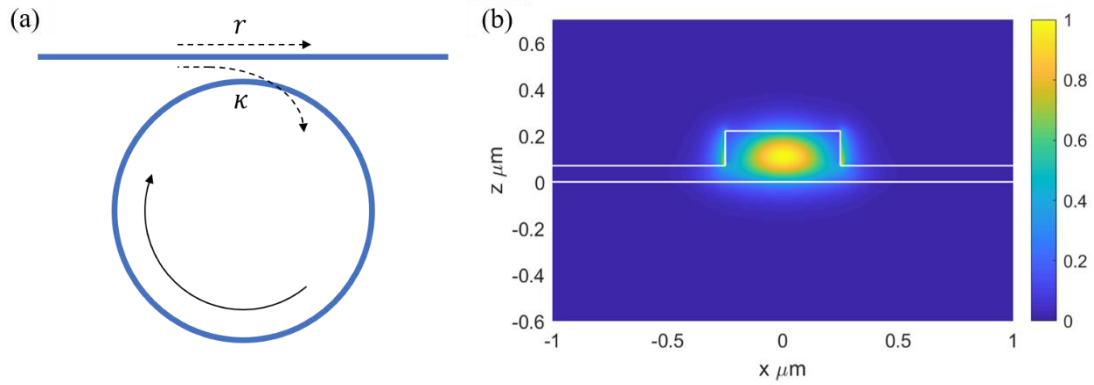

Figure 2.2 (a) Schematic drawing of an optical ring resonator, where r and κ are the electric-field amplitude transmittance and cross-coupling coefficients of the waveguide-cavity coupler, respectively. (b) Optical mode profile (magnitude) for a transverse-electric (TE) mode in a typical single-mode silicon rib waveguide. The waveguide cross section is 220 nm thick and 500 nm wide, with a slab height of 70 nm.

We simulated a silicon photonic microring whose cavity consists of a rib waveguide with a radius of 10 μm. The SOI platform has a 220 nm-thick silicon layer sandwiched between buried and cladding oxide. The rib waveguide is 500 nm wide with a slab height of 70 nm. This is a typical design of single-mode silicon waveguide which, unlike a fully-etched waveguide, can be heated efficiently by contacting a section of the (high-resistivity) slab at some distance safely off to the side of the optical mode with metal vias and traces, and driving an electrical current. The optical mode was calculated using the finite-difference eigenmode solver in Lumerical Mode Solutions™; a representative mode is shown in Figure 2.2(b). The characteristics of the optical mode and other relevant parameters are listed in Table 2.1.

Table 2.1 Values of relevant parameters used in calculations

Parameters	Value
α_{m}	0.7 dB/cm
A_{eff}	0.171 μm^2
A'_{eff}	0.124 μm^2
GVD	-1223 ps/nm·km
n_{eff}	2.53
n_{g}	4.0
n_2	6×10^{-18} m^2/W
β_{TPA}	0.8 cm/GW [105]
τ_{c}	0.8 ns
τ_{th}	1 μs
$\mathrm{d}n/\mathrm{d}T$	1.84×10^{-4} /K
C_{Si}	705 J/(kg·K)
ρ_{Si}	2.3×10^{-3} kg/m^3
η_{det}	0.95
D	100 Hz
Laser SSE[a] Ratio	60 dB/nm
$\Delta\tau$	10 ps

Based on the numerical solutions, the change in the cavity is shown in Figure 2.3. Here, we simulated a microring resonator with a coupling strength $|\kappa|^2$ of 0.01. Initially, the waveguide was assumed to have a linear propagation loss of 0.7 dB/cm, which typically includes the loss contributions from material absorption, waveguide bending and scattering due to the roughness of waveguide walls. The Q-factor of the ring was then calculated to be 9.2×10^4. As the input power scales up, TPA was observed to become more significant, as expected, and both TPA and TPA-induced FCA increase. For input power higher than about 0.37 mW in our simulations, FCA was observed to take over as the dominant loss mechanism. This results in a reduced cavity loaded Q-factor, which drops quickly once FCA dominates the cavity loss, as shown in Figure 2.3(b).

In the same figure, we have shown how the intracavity resonant power scales with the input power. While the intracavity power scales linearly in a TPA-free cavity as shown in blue dashed line (the resonant

[a] SSE: sidemode suppression ratio

enhancement factor is constant), the benefit of increasing input power becomes smaller in a nonlinear cavity for the high-power regime, as a consequence of the degraded loaded Q-factor.

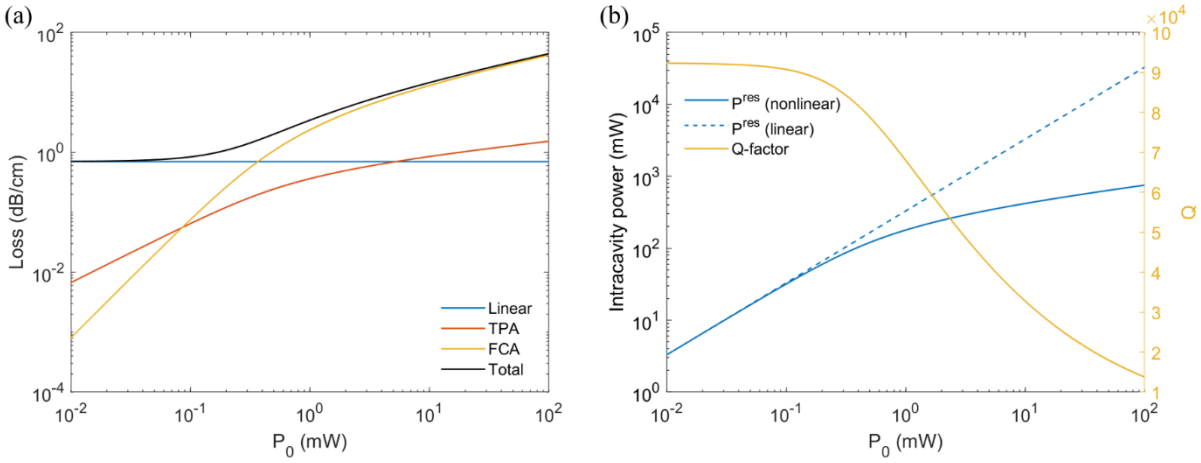

Figure 2.3 Change inside the microring cavity consisting of waveguide shown in Figure 2.2(b), assuming a constant (amplitude) coupling strength in the coupling region of 0.01. (a) Loss composition as a function of input power. To start with, there is linear absorption losses such as material absorption loss and scattering loss. As the input power increases, TPA produces free carriers which induce FCA. FCA becomes dominant at high input power levels. (b) Intracavity resonant power and Q-factor of the cavity as a function of input power. The blue dash line is the resonant power in an ideal linear cavity. The blue solid line is the power inside a nonlinear cavity. As the input power increases, Q-factor of the cavity degrades, and the resonant enhancement effect is not as strong. The rate gap between a nonlinear and linear cavity widens.

2.2 Pair Generation Characteristics in the Nonlinear Regime

PGR reflects the trend shown in Figure 2.4. In a TPA-free cavity, PGR as a function of input power exhibits the same trend as PGR as a function of $|\kappa|^2$ [113], i.e., the increasing intracavity power increases the self-phase modulation (SPM) term in the phase matching 'sinc^2' term in Eq. (2.1), hence leading to the multiple dips in the high power regime. In practice, the optical power would have to very carefully adjusted and stabilized, in order to not result in significant swings in the PGR. (Long integration times in an experiment will typically average out these fluctuations, but result in a low average rate, overall.)

In a nonlinear cavity, TPA and TPA-induced FCA prevent the intracavity power to scale with the input power as fast as in a linear cavity, thus the change in the SPM term has been slowed down significantly. In fact, with these simulated values of the key parameters, the first dip of the phase-matching term does not

appear within the reasonable pump power regions (< 1W). In this respect, these loss mechanisms have actually stabilized the cavity for pair generation, which would otherwise have been highly sensitive to the input power level and exact value of the waveguide-cavity coupling strength $|\kappa|^2$. Of course, this benefit comes with some penalty in PGR, relative to what could have been achieved if nonlinear loss was absent. Moreover, the extraction efficiency is also decreased when the coupling condition goes from over-coupling to under-coupling, which can impact the heralding efficiency. Nevertheless, since nonlinear loss cannot be avoided in silicon, the stabilization is expected to be of considerable benefit practically. Furthermore, the predicted PGR, despite the penalty, is quite high: a maximum PGR (extracted) of 55 MHz may be obtained at an input power of 1.7 mW for this ring design ($|\kappa|^2$ = 0.01), which would be comparable to many state-of-the-art SPDC devices, in a much more compact footprint, at lower pump powers, and using only simple materials such as silicon and oxide, which have no requirement for poling.

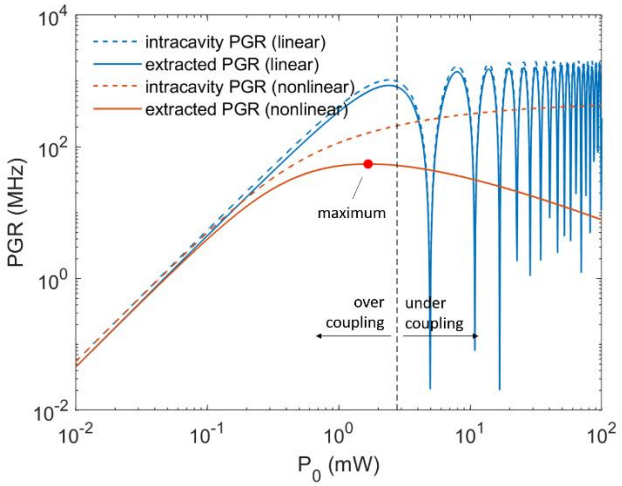

Figure 2.4 PGR inside the microring cavity consisting of waveguide shown in Figure 2.2(b), when $|\kappa^2| = 0.01$. TPA and its-induced FCA prevent the intracavity power from scaling with the input power as fast as it is in a linear cavity, Thus the increase in the SPM term in phase matching term also slows down significantly, which prevents the sinc^2 term to appear in the high power region. As the input power increases, the cavity changes from over-coupled to under-coupled, thus the extraction efficiency of the photon pairs are also compromised. The overall extracted PGR reaches a maximum of 55 MHz at the input power of 1.7 mW.

2.3 Discussion

A more comprehensive sweep of all κ and P_0 combinations, as shown in Figure 2.5(b) and (d) obtained a maximum PGR (extracted) of 75 MHz with a CAR of 577 at $|\kappa|^2 = 0.089$ and $P_0 = 31.6$ mW. Figure 2.5(a) and (c) shows the otherwise PGR if the cavity is TPA-free. In the lower-right corner, that is, high Q-factor and high power region, PGR is ultra-sensitive to the input pump power and waveguide-cavity coupling ratio, which manifests itself in the dips that are too dense to see clearly. The TPA and its-induced FCA effects removes most of the dips in the reasonable pump power levels (<1 W), which significantly relaxes the requirements for fabrication and power level accuracy.

Another distinction from the two types of resonators is the mechanisms for reaching an optimum PGR when ramping up the input pump power: for an ideal TPA-free cavity, the local optimum PGR is caused by the phase matching "sinc^2" terms, while in a practical cavity, the PGR is limited by the cavity extraction efficiency. Although increasing the input pump power can, in theory, always increase the intracavity PGR, the extraction efficiency of the photon pairs degrades as the cavity loss scales up. Therefore, the extracted PGR can not grow infinitely.

The CAR is mainly decided by the relative strength of true coincidences and accidentals. The ASE noise and residual pump scales linearly with the input pump power, while the rate of noise photons from broken pairs generally increases quadratically with the pump power in the lower power region (and slowly saturates and then declines as the power increases further), so does the true coincidence rates. However, given Eq. (1.14), the relationship between the input pump power and accidentals coincidences should be further "squared" which allows the accidentals to increase faster than true coincidences.

In Figure 2.5(d), the two most bright regions where CAR is ultrahigh are where pump powers are lowest. The first region is where photon pair generation are most efficient. Interestingly, the second region sits in the valley of the phase matching "sinc^2" term, which indicates that the broken-pair-related accidentals are suppressed more by the dip of the sinc term when compared to the true coincidences. On the contrary,

the other end of the $P_0 - |\kappa|^2$ dip line becomes the local minimum of the CAR map in Figure 2.5(d), where accidentals quickly scale up with the input pump power.

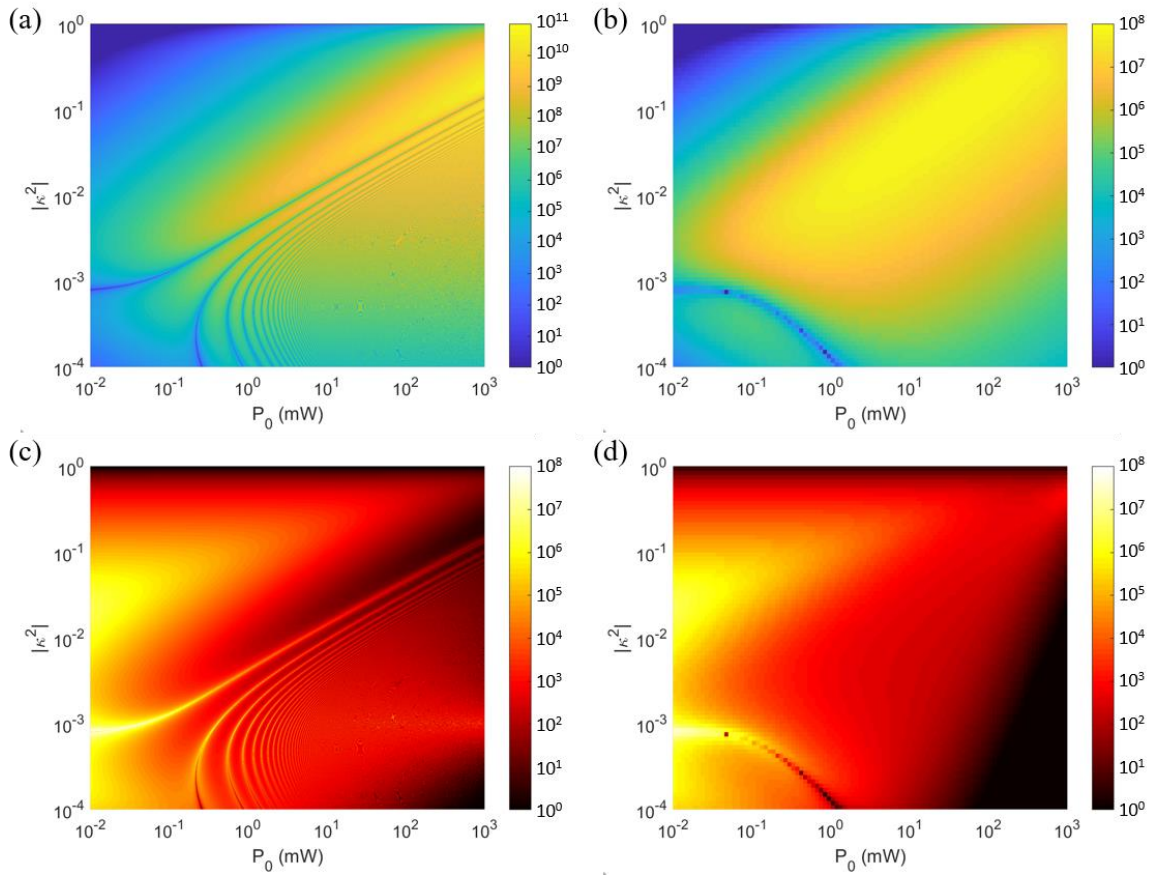

Figure 2.5 Extracted PGR (a) (in Hz) and CAR (c) (in log scale) as a function of input power and $|\kappa|^2$ in a TPA-free cavity. The right lower corner contains very fine and dense ripples representing the fast oscillating phase matching term (sinc^2) induced by high intracavity power. Extracted PGR (b) and CAR (c) (in log scale) as a function of input power and $|\kappa|^2$ in a nonlinear cavity. All calculations are based on the microring cavity consisting of waveguide shown in Figure 2.2(b).

Figure 2.6(a) shows the choice of $|\kappa|^2$ that maximize extracted PGR for each input pump power level. Figure 2.6(b) shows the photon pair characteristics, CAR and FWHM, for each combination of $|\kappa|^2$ and P_0. With TPA, the extracted PGR reaches maximum at $|\kappa|^2 = 0.089$ and $P_0 = 31.6$ mW. The relative fast drop at the high power regime is due to the 1-nm filtering after pair generation, which ensures the bandwidth of the photon pairs does not go extra broad. Within the pump power range from 0.5 mW ($|\kappa|^2 = 0.0075$) to 630 mW ($|\kappa|^2 = 0.316$), the extracted PGR is always higher than half of the maximum and the

CAR is relatively stable (1245 for 0.5mW, 616 for 630 mW). The only thing that changes drastically is the FWHM of photon pairs, which scales from 16 pm all the way up to 1 nm (restricted by the filter).

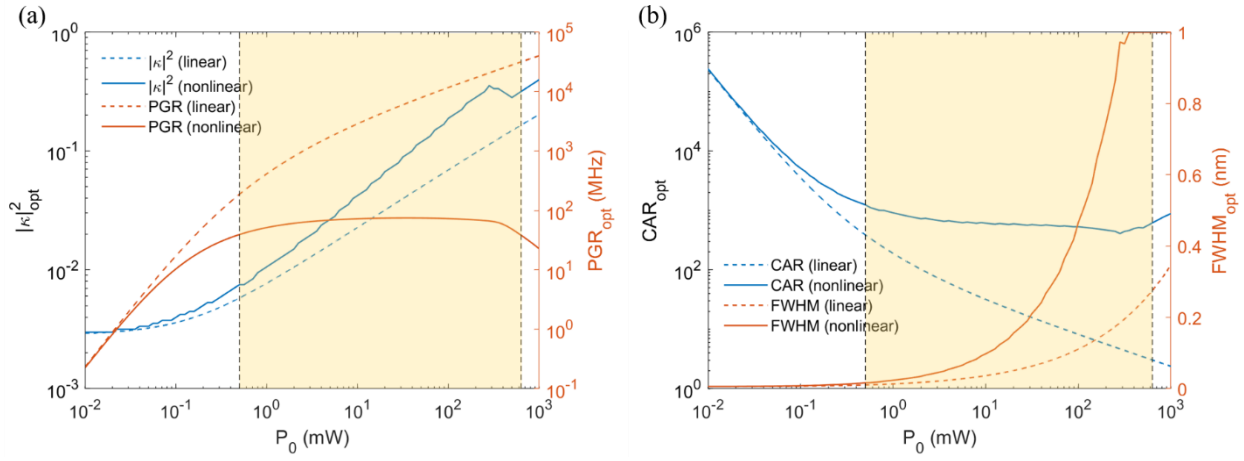

Figure 2.6 Photon pair characteristics for the combinations of $|\kappa|^2$ and P_0 to maximize PGR. (a) Optimum $|\kappa|^2$ as a function of input pump power to maximize the PGR (extracted). The dash lines are reference $|\kappa|^2$ (dash blue) and PGR (dash orange) for a TPA-free cavity. The solid lines are reference $|\kappa|^2$ (solid blue) and PGR (solid orange) for a nonlinear cavity where TPA can occur. (b) CAR and the resonance's FWHM as a function of the input pump power for the maximized PGR (extracted). The dash lines are reference CAR (dash blue) and FWHM (dash orange) for a TPA-free cavity. The solid lines are reference CAR (solid blue) and FWHM (solid orange) for a nonlinear cavity where TPA can occur. The shaded area (light yellow) is where the extracted PGR is within half of its maximum for a TPA-enabled cavity.

In most cases, one would prefer to operate in the low pump region (in this case, 0.5 mW) with a higher CAR and narrower FWHM of photon pairs without sacrificing much PGR. On one hand, the ring has a much higher photon pair generation *efficiency* in the lower power region, although not necessarily the highest overall generation *rate*. From a practical perspective, the linear regime is also more stable and amenable to feedback-stabilization.

A larger waveguide-resonator coupling coefficient strength is required to match a high pump power (e.g. $|\kappa|^2 \sim 0.316$ for a pump power of 630 mW). There may be some technical difficulties to realize this level of coupling: The ring is usually too small to realize a long-enough coupling region. Although one can reduce the gap between waveguide and the ring cavity to reduce the required coupling length, it usually cannot be made smaller than about 150 nm, based on typical fabrication tolerances in a foundry silicon

photonics process. Different in-plane coupler designs [132], or vertical inter-layer couplers [133,134] may be interesting designs for further study and generation of actual device layouts.

To further explore the potential of silicon photonic microrings as photon pair sources, we discuss here the various aspects where these devices can be improved to have a higher PGR, generate better-quality photon pairs and operate more reliably. For example, achieving high CAR depends on low detector noise, suppression of pump and scattering noise, improvement of the stability of pair generation, and improving factors such as loss in the device and the experimental setup, which lead to broken pairs and increase the rate of accidental coincidences.

2.3.1 Waveguide Engineering

The design of waveguide affects the photon pair generation process in the following ways: (1) the dispersion of the waveguide in the phase matching "sinc^2" term determines the sensitivity of the device performance to design parameters, fabrication errors and input pump power; (2) The waveguide propagation loss, together with the waveguide-cavity coupling strength, decides the Q-factor of the cavity, hence the pair generation efficiency; (3) The size of the optical mode effective area is inversely proportional to the strength of the waveguide nonlinearity.

Given that the dispersion, loss and mode confinement of the waveguide are usually inter-dependent, it is not straightforward to tell which waveguide cross section best optimizes PGR or photon quality, or the best combination of the two. To give an example, we search here for a waveguide cross section that maximizes PGR. Part of the results are shown in Figure 2.7, which contains PGR as a function of input pump power (P_0) and waveguide-cavity coupling strength ($|\kappa|^2$). (Simulations at other thicknesses give qualitatively similar observations.) The dash line in each subfigure is optimum $|\kappa|^2$ to maximize PGR for each input pump power. The white dots enclose the half-maximum region where PGR is more than half of the maximum. And the GVD is shown in the upper-left corner of each subfigure.

While obviously there are more dips (from the phase matching term in Eq. (2.1)) for the high-Q, low power regions in a more dispersive waveguide, it might not be a concern if the coupling strength can be designed within the half-maximum region, which keeps a distance from the 'oscillating' area and has an appreciable tolerance toward fabrication errors. Once the coupling strength is higher than a threshold (the starting value of the black dash line), it is guaranteed that you would not fall into the dips whatever the pump power level. One may want to choose the lowest pump power point on the border of the half-maximum region (which is the intersection of the black dash line and the white-dotted boundary) to optimize the generation efficiency the photon pairs. It also gives a general rule that the pair generation microring should always be designed as over-coupling to optimize the pair generation efficiency. At the same time, over-coupled microring has a higher extraction efficiency that not only improves the CAR but also the heralding efficiency of the photon pairs.

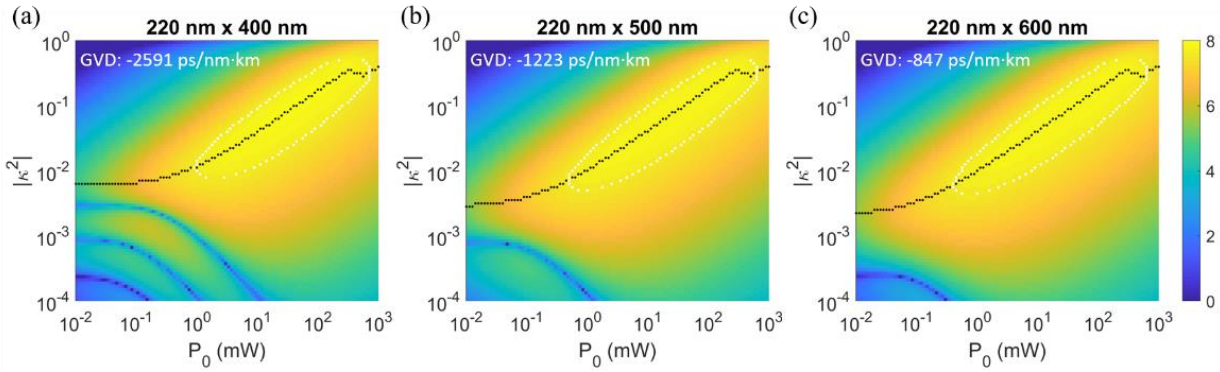

Figure 2.7 PGR (in Hz) as a function of input pump power P_0 and waveguide-cavity coupling strength $|\kappa|^2$ for different waveguide cross sections. The group velocity dispersion (GVD) is shown in the upper-left corner of each subfigure. The dash line in each subfigure is optimum $|\kappa|^2$ to maximize PGR for each input pump power.

We then scanned the cross section of a silicon rib waveguide to obtain its maximum PGR. Typically, SOI platform has a silicon layer that is 200 – 400 nm thick. And we have also swept the width of the rib from 300 to 800 nm for each thickness. The height of the slab is kept at 70 nm. It is shown in Figure 2.8 that a smaller cross section is more favorable to obtain a higher pair generation capacity. The maximum PGR is obtained in the smallest waveguide cross section (200 nm thick, 300 nm wide) with a value of 120

MHz at an input of ~90 mW and CAR of 343. While this number might neglect a lot of factors in practice, e.g. the tuning capability of the resonance stabilization system and channel propagation loss, it gives an upper bound of the pair generation capability of a silicon photonic microring.

However, most of the current demonstrations are focused on sub-milliwatt pumping of the silicon photonic microrings [25,113,120,135–137]. In the low pump power region, TPA and the induced FCA effects are not as significant and the power generation efficiency as well as CAR are much higher, as shown in Figure 2.6(b). We then simulated the maximum PGR that can be obtained by 1 mW input pump power for each cross sections, which is show in Figure 2.8(c). When the TPA and its induced FCA are mitigated in lower power region, the results are more intuitive: generally, increasing the cross section lifts the pair generation capability. And the reasons are obvious: smaller mode effective area and dispersion. A maximum PGR of 58 MHz can be obtained at 1 mW input pump power with a waveguide cross section of 340 nm-thick and 650 nm-wide (a slab height of 70 nm).

The difference between Figure 2.8(a) and Figure 2.8(c) are more clearly manifested in Figure 2.8(d), where the maximum PGR as a function of input pump power is calculated for 220 nm-thick cross sections. While larger cross sections have higher pair generation efficiencies due to smaller mode effective area and dispersion (in lower power regime), PGR saturates earlier due to stronger TPA effects, which limits the highest PGR they can achieve. It is also noted that after increasing the width to 500 nm for a 220 nm thick rib waveguide, the benefit of increasing the width further is minimal. Thus the waveguide cross section can be designed at a relatively smaller cross section to maintain single mode operation without sacrificing the pair generation capacity, which can also be shown in Figure 2.8(c).

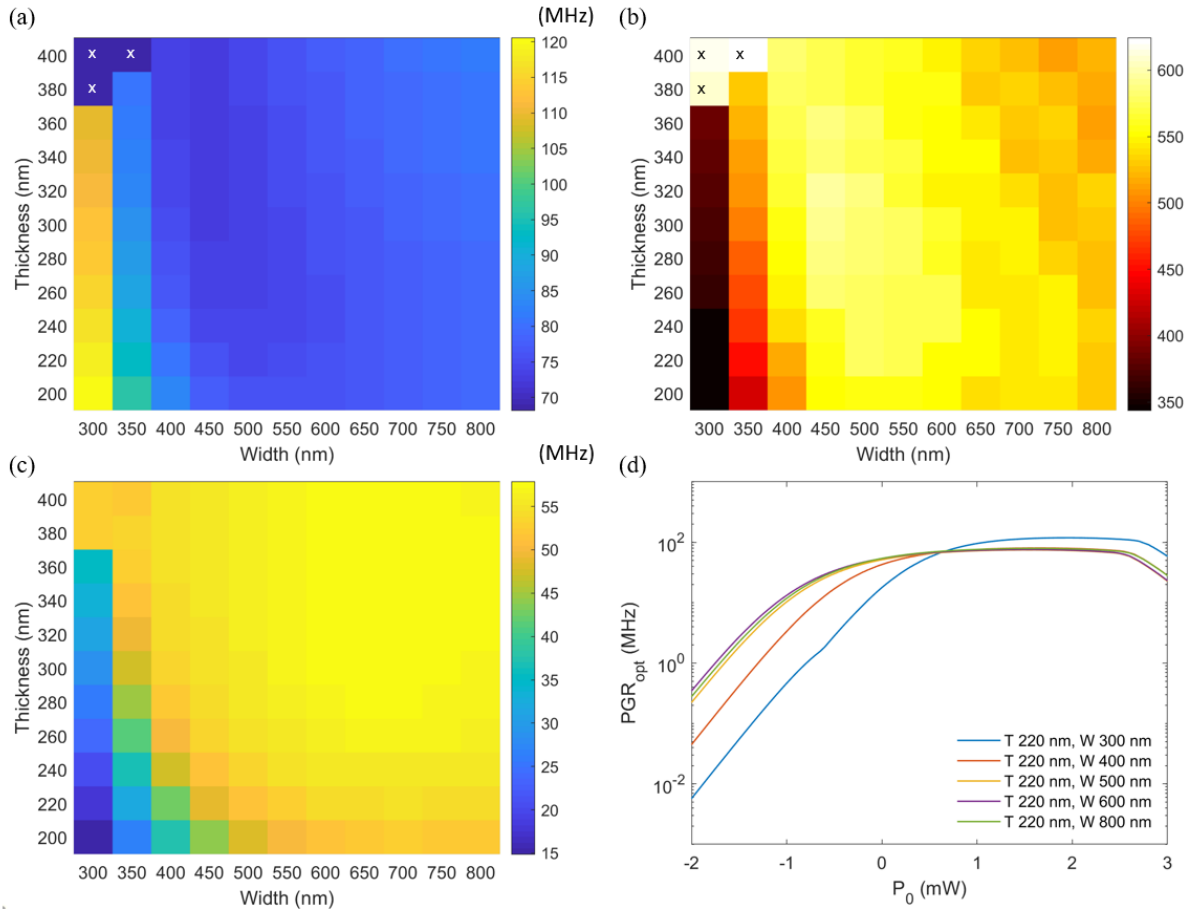

Figure 2.8 (a)-(b) Maximum PGR (a) and its corresponding CAR (b) as a function of waveguide cross section geometry. The cells denoted by crosses correspond to waveguide cross sections whose fundamental mode is TM mode. (c) Maximum PGR for input pump power of 1 mW as a function of waveguide cross section geometry. (d) Maximum PGR as a function of each input pump power level for 220 nm-thick cross sections.

2.3.2 Filtering

Loss management is critical to achieve high rate and quality of photon pairs. Not only does it reduce PGR, as channel loss break pairs and consumes true coincidences, CAR will also be degraded (see Eq. (1.12) – (1.14)). Given that the greatest contribution to loss usually comes from fiber-chip coupling (typically ~ 3-5 dB/facet for grating couplers and ~2-3 dB/facet for edge couplers), on-chip integration with functionalities such as pump laser, filters and detectors are desired. In addition, a fully integrated quantum sources significantly improves the scalability of the devices or circuits, which unfortunately has yet been realized. With demonstrations of photon sources integrated with SNSPDs [138,139] and their demonstrated

compatibility with on-chip hybrid silicon lasers [98], a high contrast on-chip filter with required extinction and low insertion loss is still out of reach.

Multiple stages are needed in the photon pair generation process. First, optical pumps always come with ASE. After pair generation, the ASE with spectral overlap with photons can never be removed. Therefore, one needs to remove the ASE before the pair generation process. Second, in many occasions, signal and idler photons need to be separated based on their spectral modes. The extinction and insertion loss of the filters would directly translate to the crosstalk and loss of photons. Third, the pump needs to be dumped completely after pair generation. Due to the much brighter pump compared to the generated photons, ultrahigh extinction ratio is required to suppress the pump to detector noise level. Let's assume an SNSPD with a detection efficiency of 95%. The pump power (1550 nm) reaching the SNSPD should be kept under -100 dBm to avoid overwhelming the detectors (let's say, 1 MHz) and -140 dBm to be comparable to detector noise level (~100 Hz). For a pump power of 1 mW (which is typical for silicon microrings), the filters have to provide a filtering extinction ratio of ~90 dB to keep power under -100 dBm and ~130 dB to 100 Hz (The microring itself serves as a filter and usually gives ~10-20 dB extinction).

A lot of efforts have been focused on achieving the on-chip high extinction filters for quantum photonics. Those filters reported in recent publications (see Table 2.2) are typically distributed Bragg reflectors (DBR) [137], arrayed-waveguide gratings [140], cascaded Mach-Zehnder interferometers (MZIs) [111,141], and coupled-resonator optical waveguides (CROWs) [110,142,143]. Although a ~100 dB extinction has been demonstrated by DBR [137] (with the assistance of add-drop rings), the size of DBR (typically millimeters long) may not be favorable for scalability. AWG has the same problem, and its extinction ratio is not competitive, which could only be used for photon pair demultiplexing. CROWs have the advantages of compact footprint, flat-top passbands and high extinction, but are sensitive to fabrication variations and environmental perturbations.

In practice, however, extinction ratio of filters is limited by the on-chip scattering of pump photons via the substrate. Filter chips are usually cascaded to demonstrate > 100 dB suppression of pump

photons [110,111,143], resulting in much higher transmission loss of photons. Gentry et. al. [142] has obtained 95 dB extinction from one single chip, with a filter cascading four 2nd -order CROWs. To avoid the pump scattering noise, the photon pair output direction was placed perpendicular to the pump input direction. The filter loss is relatively high compared to the best class. Without the addition of off-chip filters, the CAR was limited by ~3. In a word, a good solution of on-chip high-contrast filtering is still awaiting.

Table 2.2 Comparison between the recent demonstrated high-extinction filters on silicon integrated photonics platform for quantum photonic applications.

Year	Ref	Type	Size	BW (nm)	FSR (nm)	Extinction[a] (dB)	IL (dB)
2014	Harris et. al. [137]	DBR + ring	2.6 mm (DBR)	1 - 2	n/a	95-100	4.5
2014	Matsuda et. al. [140]	AWG	-	0.64	n/a	~30	7.7
2017	Piekarek et. al. [111]	MZI	-	> 1	6.4	65	1.5
2019	Lee et. al. [141]	MZI	-	-	~20	55	1.4
2013	Ong et. al. [110]	CROW	~30 μm × 100 μm	1.69	7.3	50	1.4
2018	Gentry et. al. [142]	CROW	-	0.8	14.6	95	>3
2019	Kumar et. al. [143]	CROW	~20 μm × 400 μm	-	9.7	74	~3

2.3.3 P-I-N Diode for Pair Generation Enhancement and Resonance Monitoring

In section 2.1.4, we assume that the pump is always perfectly aligned to the ring resonance, which is not quite true in reality, As shown in Figure 2.1(a) and discussed in Section 2.1, resonance red-shifts as a result of the competition between FCD (blue shift) and thermo-optic (red shift) effects. The asymmetric lineshape of the resonance when sweeping the laser wavelength indicates the bistability of the ring cavity, which makes the ring unstable when operated close to resonance with high pump power. An active resonance tuning system is therefore essential to keep the pair generation process stable. While thermal-optic effects can be used for tuning, a native monitoring photodetector used to be lacking on the SOI platform due to its transparency in the bands of interest (i.e., 1310 nm and 1550 nm telecommunication bands).

While germanium and AlGaInAs photodetectors have satisfactory responsivity and have been used for power monitoring in silicon, they require additional processes that increase the cost and complexity of the devices. Instead, silicon p-i-n diode is found to provide a non-invasive way of probing the power inside

[a] Extinction here is the best number achieved for a single chip.

the cavity based on defects [144], surface-state absorption [145] or TPA [146,147]. Particularly for photon pair generation, defect-enhanced detection by ion-implantation might not be suitable due to the extra loss that degrades the Q-factor of the cavity, which is important for photon pair generation efficiency and quality. A detailed discussion of the p-i-n diode used in this dissertation can be found in [130], where a readily-detectable photocurrent on the scale of micron-Ampere under a reverse bias of -1 V was provided by the silicon waveguide comprising the ring without ion-implantation or defect-enhancement of the waveguide, or the introduction of other materials such as germanium or III–V semiconductors. Besides, the reverse-biased silicon p-i-n diode also contributes to the pair generation process by sweeping out the carriers generated by TPA, which mitigates the perturbation to the cavity characteristics and enhance the PGR. A two-fold enhancement has been reported [148].

2.4 Conclusion

A set of detailed simulations have been performed for the photon pair-generation process, based on SFWM in high-Q silicon microring resonators. Such devices are known to exhibit nonlinear behavior in the high optical pump power regime, when the optical power level in the feeder waveguide typically exceeds a few milliwatts. While the thermal effects can possibly be compensated for by feedback and tuning, the nonlinear loss effects can be quite severe. Our simulation results show that, in this nonlinear regime, the pair generation capability (in terms of the rate of photon pairs that can be extracted from the device) is surprisingly tolerant to the design of the coupler between the waveguide and resonator, which happens to be the main contribution of fabrication errors in these devices. Certain other parameters, e.g., the spectral FWHM of the two-photon state, may, however, increase continuously with pump power. Since this is also important for indistinguishability and purity of the quantum state, the coupling strength need still be carefully selected. Taken together, these results suggest that the notorious sensitivity to the exact design parameters of a high-Q microring resonator may, at least in the case of silicon, be fortuitously stabilized, rather than destablized, by the predominant nonlinear effects of TPA and FCA, which may benefit the

process of photon-pair generation at fairly high rates, exceeding several tens of millions of photon pairs per second.

Chapter 2 contains the material submitted for publication as it may appear in the following of which the dissertation author was the primary investigator: Chaoxuan Ma, Shayan Mookherjea. “Prospects for photon-pair generation using silicon microring resonators with two photon absorption and free carrier absorption.”

Chapter 3
Generation of High-Quality Entangled and Correlated Photon Pairs

3.1 Introduction

The reported performance of photon pairs generated from silicon photonic microrings—in terms of the usual metrics such as CAR, $g^2(0)$ and Franson two-photon interference visibility (V_F)—has been significantly inferior to those of traditional pair-generation devices formed using optical fiber or crystals such as periodically poled lithium niobate (PPLN) and KTP, where CAR > 10,000, $g^{(2)}(0) < 0.01$ and V ≈ 99% are common [91,92,149,150]. Silicon-photonic-based pair generation devices may not be able to generate a comparable number of photon pairs per second because of the weaker nonlinearity compared to crystal, and length limitations compared to fiber. Thus, it is desirable at this time that a high quality of photon pairs be demonstrated, with high pump efficiency. There are applications, such as detector calibration and short-range communications, where a very large number of photons per second is perhaps not essential, but a source that is neither bright nor of high quality is probably not of much use, even if cheap. The objective of this chapter is to report record performance numbers achieved (at room-temperature, in an "open" setup, i.e., not sealed off from the laboratory environment) using optically pumped SFWM in a high-Q silicon microring resonator. Previous reports have shown saturation / roll-off of parameters such as CAR at much lower values than measured here; therefore, these results present a more optimistic prospect for using silicon photonic devices for pair generation in quantum optics experiments than may have been expected by the wider community so far.

3.2 Experiment Details

A microscopic image of the ring resonator together with a schematic of the waveguide cross-section is shown in Figure 3.1. The microring was fabricated using a foundry silicon photonic process on SOI

wafers, using ridge waveguides of width 0.65 μm, height 0.22 μm, and slab thickness 70 nm, designed for low loss transmission in the lowest-order mode of the transverse electric (TE) polarization defined relative to the device plane. The microring resonator was designed with a radius of 10 μm, side-coupled to the feeder waveguide. The slab regions of the ridge waveguides were doped, followed by contact and via formation and metallization, to form a p-i-n diode for monitoring, under reverse-bias, the optical power circulating in the microring. The Si waveguides used in the feeder waveguide and microring had a propagation loss (measured on test sites) of approximately 0.7 dB/cm, resulting in a microring intrinsic quality factor of approximately 9×10^5, and a resonance lifetime $\tau \approx 76$ ps (loaded quality factor of 9.2×10^4 at 1550 nm, with a measured spectral FWHM of approximately 2.1 GHz).

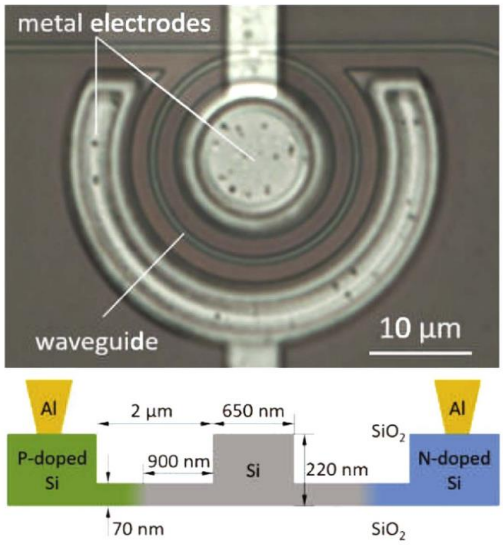

Figure 3.1 Upper: microscope image of the ring resonator side-coupled to a waveguide, with metal traces connecting to a p-i-n diode fabricated across the microring to monitor its resonance [130]. Lower: a schematic of the waveguide section. Figure reproduced from [130], with the permission of AIP Publishing.

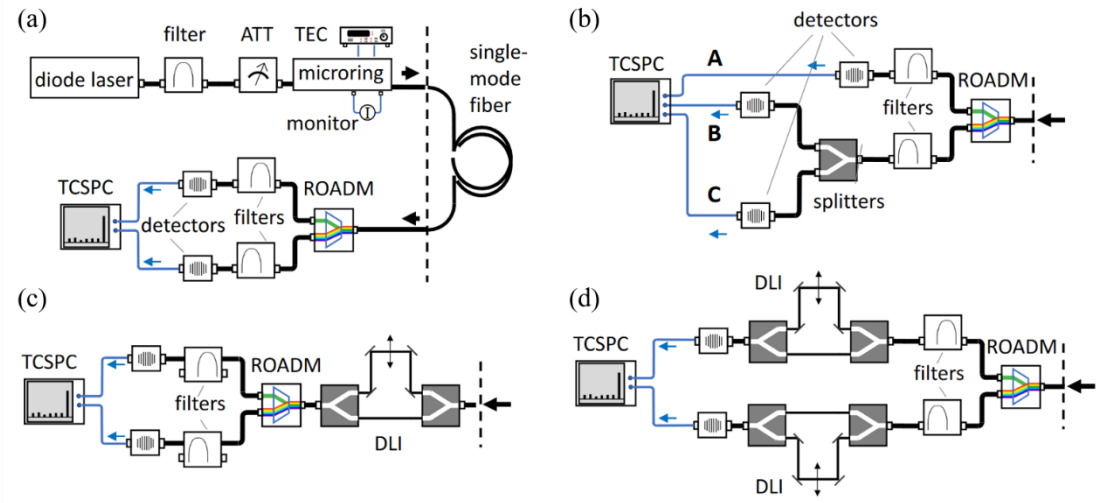

Figure 3.2 (a) The experimental configuration for pair generation, and measurement of CAR. ATT: variable optical attenuator, TEC: thermo-electric controller, TCSPC: time-correlated single-photon counter. ROADM: 3-port reconfigurable optical add-drop multiplexer. (b) Modifications to the detection setup for measurement of the conditional (heralded) self-correlation, $g^2(0)$. (c) Measurement of two-photon Franson interferometric visibility using the folded configuration. DLI: delay-line interferometer. (d) Measurement of two-photon Franson interferometric visibility using the un-folded configuration.

Measurements reported here used the experimental configuration shown in Figure 3.2. The bare-die chip was mounted on a temperature-controlled stage with a thermo-electric controller (TEC) in feedback with a thermistor on the stage mount. To establish a stable resonance, the silicon photonic chip with the microring was heated until the selected resonance aligned with the pump laser. The spectral alignment was continuously monitored during measurement using the reverse-biased photo-current of a silicon p-i-n junction diode fabricated across the microring [130], and confirmed using high-magnification infrared camera images of the microring. Polarization-maintaining fibers, fiber-loop paddles and lensed tapered fibers with anti-reflection coating were used to couple light to and from the silicon chip, and nano positioning stages with piezoelectric actuators were used for accurate positioning of the fiber tips to the waveguide facets. An automated software program attempted to continuously optimize the coupling. The insertion loss of each fiber-to-waveguide coupler was estimated as 3.5 dB averaged over the wavelengths of interest based on previous experiments. Light was coupled to and from the chip using lensed tapered polarization-maintaining fibers. Output light from the chip was routed through cascaded filters to select one

pair of spectral lines of Stokes (also called idler) and anti-Stokes (signal) photons positioned symmetrically around the pump wavelength.

The pump wavelength was positioned at 1554.9 nm and signal and idler photons were detected at 1535.5 nm and 1574.7 nm, respectively. External tunable filters (benchtop components) were used at these three wavelengths with FWHM's of approximately 1 nm, 0.6 nm and 0.8 nm, respectively. The spectral width of the microring resonance was approximately 0.03 nm, much narrower than the filter widths. Thus, the filters do not reshape the joint-spectral intensity, as maybe a concern with broadband SFWM in waveguides. Photons were detected using fiber-coupled superconducting (WSi) SNSPDs, cooled to 0.8 K in a closed-cycle Helium-4 cryostat equipped with a sorption stage. The detection efficiencies for the SNSPDs were about 90% for two detectors and about 65%for the other two detectors; these detectors were not gated and were operated in a simple dc-biased mode with an RF-amplified readout. Coincidences were measured using a multi-input TDC instrument, with 0.16 ns minimum bin width, in start-stop mode.

3.3 Measurement

Since the purpose of this chapter is to demonstrate that high CAR values and low $g^2(0)$ values can be experimentally achieved using off-the-shelf, foundry-fabricated silicon photonic devices, we focus mainly on the low pump-power case; nevertheless, an appreciable rate of pairs and single photons was measured because of the relatively high brightness of the source.

3.3.1 Single and Coincidence Counts

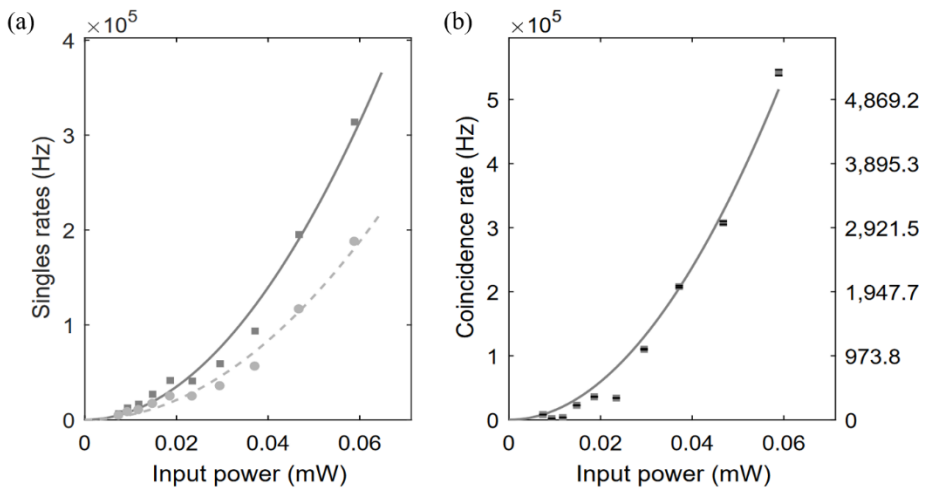

Figure 3.3 (a) Singles count rates (in Hz, raw measurements, not scaled) versus CW optical pump power in the feeder silicon waveguide. The difference in single counts between the signal and idler channels stems from the slightly different losses through the filters (5.0 dB and 7.2 dB respectively). (b) Coincidence rate (in Hz), using the setup shown in Figure 3.2(a). The left-hand side vertical axis shows the scaled coincidence count rates, accounting for chip coupling loss, filter insertion loss and detection efficiency. The right-hand side vertical axis shows the raw measured coincidence count rates (Hz).

Figure 3.3(a) shows the measured singles rates as a function of pump power, with differences in the values based on the slightly different losses through the filters (5.0 dB and 7.2 dB at the signal and idler wavelengths). Both sets of data are fitted by a quadratic function of the input pump power P_0 (in the feeder waveguide before the microring). The on-chip PGR was calculated from the measured coincidence rate by accounting for the insertion loss of the filters, and chip-waveguide coupling (3.5 dB), and the efficiency of the detectors (0.9). In Figure 3.3(b), the (on-chip) PGR is shown, and the fitted line, following the functional form $\mathrm{PGR} = R \times P_0^2$, agreed with the data (The right-hand side axis shows the raw measured coincidence rates). The fitted generation efficiency is $\mathrm{R} = 149 \pm 6\ \mathrm{MHz/mW^2}$ (one standard deviation uncertainty). This is a good value for silicon microrings, which improves upon previous experimental results ($R = 1 - 10\ \mathrm{MHz/mW^2}$ tabulated in [113]). As a comparison, on-chip SPDC sources formed using PPLN or aluminum nitride [79,151] report typical pair generation efficiencies of about 6−14 MHz/mW.

3.3.2 CAR

Figure 3.4(a) shows the measurements of CAR versus input (CW) pump power. Raw two-fold coincidence counts (C_{cc}) and accidental coincidence counts (C_{acc}) between the generated photon pairs were measured for typical acquisition times of 30-300 seconds[a] and binned into a histogram (one for each input pump power level). The uncertainties in C_{acc} are one standard deviation values of counts in bins away from the peak (start-stop delays were measured up to 100 ns time difference), and were propagated to generate the error bars in the CAR plot. Coincidences due to dark counts were measured separately, but since their contribution was negligible (~100 Hz), they were not subtracted from the measurements. Each histogram peak was fitted by a Gaussian function, whose FWHM was typically 0.31 ns. The histogram of start-stop coincidences (measured bin counts divided by the measurement time in seconds) which resulted in the highest CAR is shown in Figure 3.4(b), along with a segment of the accidental coincidences in the inset figure. As shown in Figure 3.4(c), the peak was well fit by a Gaussian function.

[a] The complete list of integration times is (from highest pump power to lowest power): 30, 30, 30, 120, 120, 180, 240, 600, 2100, and 3000 seconds.

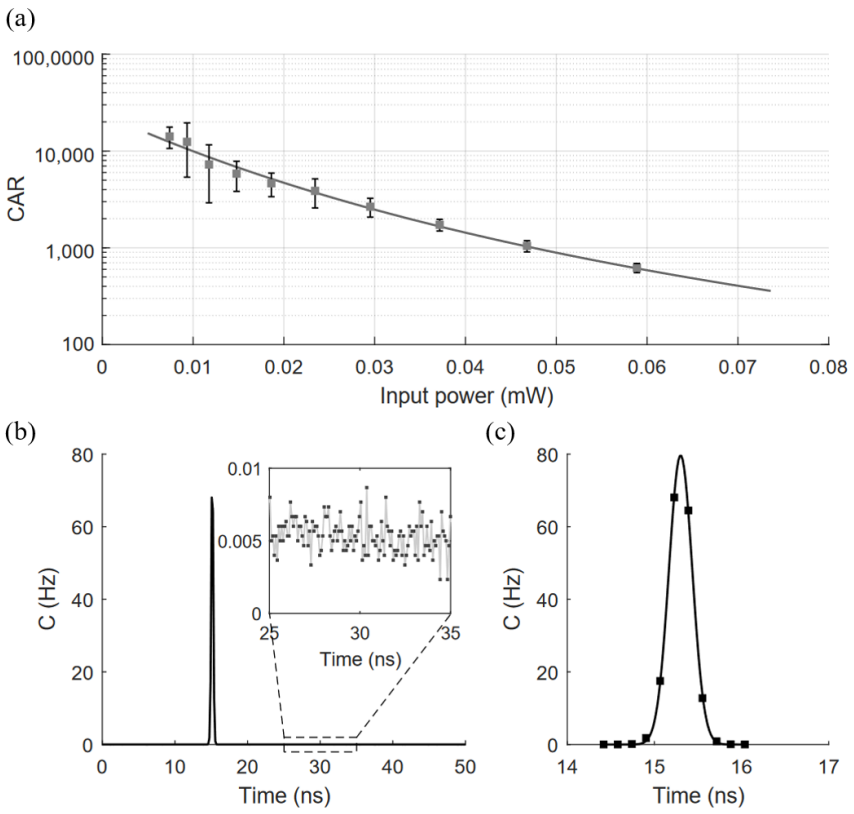

Figure 3.4 Pair generation. (a) CAR versus (CW) optical pump power in the feeder waveguide before the microring. The error bars are one standard deviation, calculated as described in the text. The highest measured CAR was 12,105 ± 1,821. (b) The start-stop coincidence counting histogram for the highest CAR value. The inset shows a segment of the accidental coincidences. (c) Fit of the coincidence peak using a Gaussian function, with FWHM of 0.315 ns.

The highest CAR was 12,105 ± 1,821 measured using an integration time of 3,000 seconds, when the pair generation brightness was 8×10^3 cps/GHz. At the highest power values used here, $\mathrm{CAR} = 532 \pm 35$ with an integration time of 30 seconds, at a pair generation brightness of 550×10^3 cps/GHz. Dividing further by the square of the optical pump power in the feeder waveguide calculates the spectral brightness of the source, equal to 1.5×10^8 cps/GHz/mW^2 at the highest CAR value and 1.6×10^8 cps/GHz/mW^2 at the lowest CAR value (the two numbers are approximately the same, as is expected). The spectral brightness of this microring device is two orders of magnitude higher than reported by other groups [152], a factor of twenty four higher than our previous results [113], and is a factor of two greater than that of the silicon microdisk [112]. CAR decreased at higher pump powers, as expected, and since the PGR was higher, a

shorter integration time was required to achieve reasonably small uncertainty error bars. CAR values in the tens of thousands have been measured in SPDC pair generation [149], but not yet shown in silicon photonics where values have been in the few thousands [83,153]. (The CAR metric can be inflated by un-naturally narrowing the coincidence window, e.g., less than the timing jitter of the detectors [153].) Achieving high CAR depends on low detector noise, suppression of pump and scattering noise, improvement of the stability of pair generation, and improving factors such as loss in the device and the experimental setup, which lead to broken pairs and increase the rate of accidental coincidences.

3.3.3 Heralded single-photon generation

Figure 3.5 shows the heralded (i.e., conditional) single-photon second-order self-correlation function, $g_{\mathrm{H}}^2(0)$. The arrival times of events at the TDC module were synchronized by selecting appropriate lengths of BNC cables. Coincidences were defined as simultaneous detections within a 5 ns time window, measured directly by the TDC hardware. Counting times varied from 100 seconds for the higher pump powers to 600 seconds for the lowest pump power. The fitted line in Figure 3.5 has the sigmoidal functional form, $g_{\mathrm{H}}^2(0) = aP_0^2/(1 + aP_0^2)$, where $a = 6.3\ \mathrm{mW}^{-2}$ is the fitted coefficient. This fitting form is based on the fact that $g^2(0)$ is proportional to the biphoton rate [154], which, in SFWM, is quadratic in the pump power, P_0, at low values, but saturates (to 1) as P_0 increases. Values as low as $g_{\mathrm{H}}^2(0) = 0.0053 \pm 0.021$ were directly measured, for a measured heralding rate of $R_A = 18$ kHz. Even at the highest power values used in this sequence of measurements, $g_{\mathrm{H}}^2(0) = 0.11 \pm 0.051$, well below the classical threshold, at a heralding rate of $R_{\mathrm{A}} = 340$ kHz.

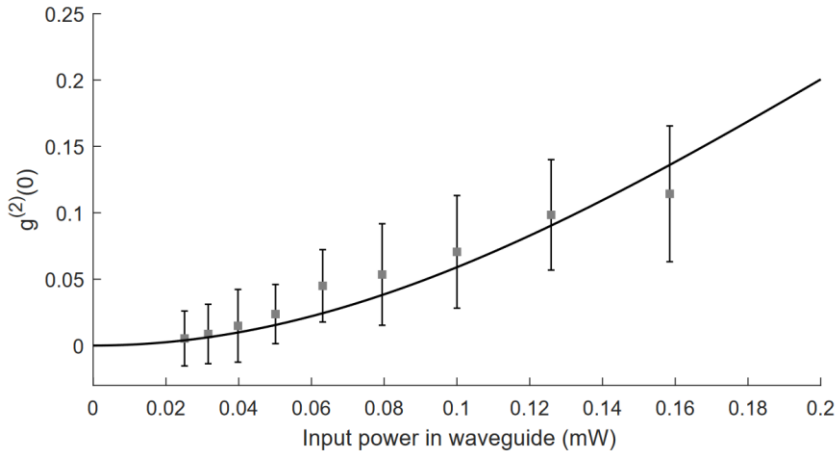

Figure 3.5 Heralded single photon generation. Conditional self-correlation (heralded auto-correlation) $g^2_{\mathrm{H}}(0)$ measured using the setup shown in Figure 3.2(b). The error bars are one standard deviation. The lowest measured $g^2_{\mathrm{H}}(0)$ was 0.00533 ± 0.021.

The Klyshko efficiency was calculated to be between 3% and 4% for the input powers shown in Figure 3.5. These are typical values for silicon photonic SFWM sources, and are about a factor of 10 inferior to those of SPDC based pair sources or glass integrated optics (at 700 nm wavelengths) [155]. The main reason for the lower efficiency is loss: the sum of the fiber-to-waveguide loss and the insertion loss of the filters is about 7-10 dB for each of the photons in the current experimental configuration. Improving the Klyshko efficiency is a topic of current research, e.g., using active delay/multiplexing schemes to raise the heralding rates significantly [80]. Another approach is to adjust the coupling efficiency between the micro-resonator (in the reported case [83], a microdisk resonator with an under-cut "pedestal") and the input waveguide (in the reported case, a tapered optical fiber) by adjusting their relative positioning. A high-Q resonator could go from under-coupled condition to over-coupled condition by moving the input waveguide closer to the resonator, thus improving the extraction efficiency of the photon pairs generated inside the resonant cavity. In our device, the position of the waveguide near the microring is fixed during lithography, thus requires iterative fabrication to optimize.

3.3.4 Energy-time entanglement

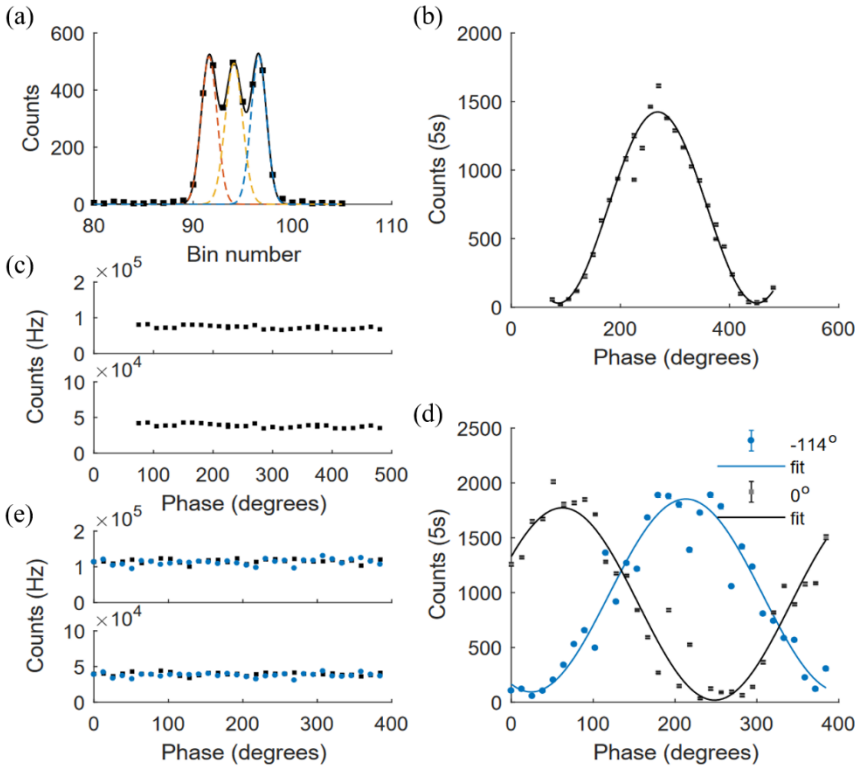

Figure 3.6 (a) Representative histogram for the measurement of energy-time entanglement (at a particular phase setting of the DLIs), with an acquisition time of 5 s. The solid blackline, showing the sum of the three Gaussians shown in red, blue and green dashed lines, fits the black dots which show the binned coincidence measurements. (b) Two-photon interference pattern measured using the folded Franson interferometer configuration. Grey dots (with errorbars): measured experimental data (coincidence counts), black line: fit. (c) The singles counts for the folded interferometer, measured at the same time as the two-photon coincidences. (d) Two-photon interference pattern measured using the un-folded Franson interferometer configuration. The interference pattern for two different phase settings on the second delay-line interferometer are shown. Grey and blue dots (with errorbars): experimental data, black solid and dashed lines: fit. (e) The singles counts for the unfolded interferometer.

The generated photon pair is expected to demonstrate energy-time entanglement. Such measurements have already been shown for several silicon photonic pair-generation devices [28,152,156–159], and high values of visibility are confirmed for the microring device measured here. Figure 3.6(b) shows the measurement of visibility fringes using a folded Franson interferometer configuration, in which both the signal and idler photons co-propagate through the same delay-line interferometer (DLI) [160]. Figure 3.6(d) shows the measurements of the unfolded Franson interferometer configuration, in which two

separate DLIs were used, one for the signal photons and one for the idler photons. Two fiber-coupled, polarization-maintaining, piezo-controlled DLIs, each with a free spectral range (FSR) of 2.5 GHz and peak-to-valley extinction ratio approximately 25 dB were used in these measurements. Unlike in other experiments [152,159], no active DLI stabilization was required, considerably simplifying the experimental requirements. Approximately the same number of counts were measured here in 5 seconds as took nearly 50 times longer in other experiments [152]. Data scatter in the fringes was caused by fluctuations of photon pair flux coupled to the DLIs, which was mainly a result of polarization drifting (of both pump and generated photons) and fiber-to-chip misalignment.

The histogram is shown in Figure 3.6(a), where the three peaks corresponding to $|l,s\rangle$, $|l,l\rangle$ (or $|s,s\rangle$), and $|s,l\rangle$ were fitted. The fitting uncertainty (one standard deviation) is shown as the errorbar in Figure 3.6(b) and (d) and is too small to be visible. In the unfolded interferometer, the phase of one of the DLIs (i.e., the phase delay between the short arm and the long arm of that DLI) was held constant, and the phase of the other DLI was swept over approximately one FSR. The DLIs were tuned by voltage; as expected, the voltage required to tune the folded Franson interferometer, where both signal and idler photons experience the phase tuning, over a full period (3.86 V) was almost exactly one-half that of the unfolded Franson interferometer (7.82 V), where only the signal photon experiences the phase tuning. Although the signal and idler photons are at different wavelengths, separated by about 40 nm, the differential group delay accumulated over a few meters of fiber is negligible, compared to the timing jitter of the detectors. The fitted measurements showed V clearly in excess of this threshold value (70.7%), measured using a pump power in the feeder waveguide of about 50 μm, resulting in a PGR of about 68 kHz. From the raw data, $V_{\text{data}}^{(\text{f})} = 98.8 \pm 0.6\%$ for the folded Franson interferometer measurement, and $V_{\text{data}}^{(\text{uf})} = 98.2 \pm 0.9\%$ and$97.1 \pm 0.5\%$ for the two phase settings of the unfolded configuration. From a fit to the measurements based on the non-linear least-square curve fitting algorithm in Matlab, $V_{\text{fit}}^{(\text{f})} = 95.9 \pm 5.5\%$ for the folded configuration, and $V_{\text{fit}}^{(\text{f})} = 97.8 \pm 14\%$ and $90.3 \pm 14\%$ for the unfolded configuration. In

each case, the stated uncertainty is one standard deviation, but there are differences in the source of the uncertainty. For the data points, the uncertainty arises from the goodness-of-fit of the parameters of the Gaussian function used to fit the central peak [see Figure 3.6(a)]. When the ensemble of points shown in Figure 3.6(b) and (d) is fitted with a sinusoid function, the uncertainty then arises from the goodness-of-fit of those fitted parameters. These measurements confirmed the energy-time entanglement properties of the pairs, as shown by the sinusoidal variation of coincidences with phase, and in both cases, the flat singles rates (versus phase), shown in Figure 3.6(c) and (e), show the absence of single-photon interference, as desired [54,55].

3.4 Discussion

Table 3.1 summarizes recent pair generation results using silicon photonic microring resonators. In only about five years, the reported maximum measured CAR values for pair generation, using equipment that is commercially readily available, have improved greatly from about 10 to over 10,000 (In fact, we measured a record CAR of 19,000 in the work of Section 5.2, which is the highest CAR value yet reported for pair generation in silicon photonic microrings, at any wavelength). The measured $g^2(0)$ values for heralded single-photon generation have decreased from about 0.2 to about 0.005, and Franson interferometry visibility has increased to about 98-99%. The spectral brightness of our device, about 1.6×10^8 cps/GHz/mW^2, was significantly higher than reported for other silicon microrings, and in fact, a factor of two higher than the micro disk resonator [112]. Measurements reported here took between a few seconds and a few minutes per data point.

These experiments benefited from advances in single-photon detectors, and several other experimental improvements compared to our earlier experiments: Readout from an integrated monitoring photodiode across the microring helped align the resonance to the laser wavelength; The temperature of the microchip was accurately stabilized; The polarization state of the input light and fiber-waveguide alignment were actively monitored and controlled; The residual ASE from the pump was cleaned for the detection

stage. We expect that with better packaging and higher levels of integration, performance may improve further, and devices may be tested for extended durations. The performance of the microring itself may still improve; the resonator coupling coefficient can be optimized, according to the discussion in Chapter 2 , for a particular feature, e.g., desired PGR and characteristics.

Table 3.1 Recent results of photon pair generation using silicon microring resonators (comparison: recent silicon microdisk results)

Year	Ref.	Dimensions[a] (nm)	Radius (μm)	Q	PGR	Avg. pump	CAR	$g^2(0)$	V_F[b]
2009	Clemmen et al. [135]	500×200	7	4.5×10^4	300 kHz	400 μW	30	-	-
2012	Davanco et al. [161]	500×200	13	1×10^4[c]	220 kHz	1.7 mW	15	0.19	-
2012	Azzini et al. [136]	500×220	5	7.9×10^3	200 kHz	200 μW	250	-	-
2013	Engin et al. [148]	450×220×50	11	3.8×10^4	123 MHz	5 mW	37	-	-
2014	Harris et al. [137]	500×220	15	4×10^4	600 kHz	300 μW	50	-	-
2015	Silverstone et al. [120]	500×220	15	9.2×10^3	4.6 MHz	150 μW[d]	10	-	-
2014	Guo et al. [114]	450×220×50	21	8.1×10^4	14 kHz	100 μW	180	-	-
2015	Suo et al. [158]	450×220×50	21	8.1×10^4	-	500 μW	920	-	92%, 92%
2015	Grassani et al. [156]	500×220	10	1.5×10^4	400 kHz	250 μW	132	-	95%
2015	Wakabayashi et al. [157]	400×220	7	2×10^4	21 MHz	410 μW	352	-	93%, 96%
2017	Fujiwara et al. [162]	400×220	10	-	10 MHz	500 μW	350	-	82%, 95%
2015	Gentry et al. [101]	1080×sub-100	22	3.1×10^4	165 Hz	5 μW	37	-	-
					29 kHz	50 μW	55		
2015	Steidle et al. [153]	500×220	19	5×10^4	60 kHz[e]	200 μW	1984	-	-
2015	Preble et al. [163]	500×220	19	1.5×10^4	-	700 μW	80	-	93%
2016	Savanier et al. [113]	650×220×70	10	9.6×10^4	83 kHz	79 μW	65	-	-
2016	Mazeas et al. [152]	600×220	60	4×10^4	2.6 MHz	500 μW	-	-	99%, 98%
2017	This work [25]	650×220×70	10	9.2×10^4	1.1 MHz	59 μW	532	0.098	98%, 97%
					16 kHz	7.4 μW	12,105	0.005	-
2015	Jiang et al. [112]	[Microdisk]	5	5×10^5	855 kHz	79 μW	274	-	-
2016	Lu et al. [83]	[Microdisk]	5	5×10^5	1.2 kHz[f]	12 μW	2,610	0.003	-

3.5 Summary

Taken together, the measurements reported here support and augment the growing evidence in favor of silicon (i.e., semiconductor) microring resonators as a viable architecture for optically-pumped photon pair and heralded single photon generation at telecommunications-compatible wavelengths, and establish a new level of performance of silicon-photonics devices, which (we hope) may now be considered

[a] Width × height × slab height.
[b] Energy-time entanglement, measured visibility (i.e., without subtracting accidentals, re-scaling etc.) Multiple entries indicate different reference phase settings.
[c] Effective Q calculated from the measured group delay
[d] Peak power = 0.25 W.
[e] From the stated brightness.
[f] Detected pairs; stated rate: 4×10^{-4} pairs/pulse×3 MHz rep. rate.

seriously for potential implementation in experiments and deployed systems. The optical pump requirements are simple, and the pump could also be integrated into the silicon photonics manufacturing platform [98]. Such devices may be inexpensive to manufacture (in volume) and could, for some applications, conveniently replace the crystal- or fiber-based instruments / assemblies used today both in the laboratory and in the field.

Chapter 3 contains the material as it appears in the following of which the dissertation author was the primary investigator: Chaoxuan Ma, Xiaoxi Wang, Vikas Anant, Andrew D. Beyer, Matthew D. Shaw, and Shayan Mookherjea. “Silicon photonic entangled photon-pair and heralded single photon generation with CAR > 12,000 and $g^{(2)}(0) < 0006$.” Optics Express 25, no. 26 (2017): 32995-33006.

Chapter 4
Photon Pair Generation Using a Silicon Photonic Hybrid Laser

4.1 Introduction

The standalone silicon photon pair generation devices, e.g. waveguides, microrings, microdisks, are far from a complete scalable quantum photonic toolkit [164,165]. Despite the large device library in silicon photonics, an efficient monolithic on-chip laser is still missing because of the indirect bandgap of silicon. Therefore, discrete lasers are still used to pump the silicon chips in most experiments, which are laboratory-grade instruments (including, in some instances, optical parametric oscillators and mode-locked lasers) with cost and size thousands of times higher than that of a silicon chip. Doped-silica [30], nitride [79], and poled-crystal waveguide [166,167] platforms for quantum photonics also all rely on external lasers.

III-V integrated optics can be used as an integration platform [168–171], but PGR and quality are currently superior in silicon photonics technology and the manufacturing costs of the latter are likely to be lower as well. Hybrid III-V/Si lasers can be fabricated in a CMOS-compatible process on larger-area SOI wafers, which leads to manufacturing scalability, potential cost reduction, and silicon micro-electronic integration. This technology leads to the potential to have an on-chip pump source to excite our microring for pair generation. Expanding on an earlier conference presentation [98], we show here that electrically pumped hybrid silicon lasers (a micro-chip scale device, fabricated at wafer-scale) can be used to generate photon pairs and heralded single photons at room temperature (the heralding detector is cryogenically cooled) from a silicon microring resonator. The hybrid laser used here was designed for high volume (classical) optical communications, rather than being customized for these quantum optics experiments, and is supported by cost-effective large-scale manufacturing in industry [172,173]. In this section, we investigate the feasibility of using silicon photonics wafer-scale fabrication technology to create both the

micro-resonator in which SFWM occurs and the optical pump laser needed to initiate the process by comparing pair generation metrics under optical pumping with the hybrid laser and those achieved with a desktop reference laser.

4.2 Experimental Details

Both the silicon microring resonator and the hybrid silicon/III-V laser were fabricated using wafer-scale processing on SOI wafers in a CMOS manufacturing process. The microring was designed using the same waveguide design as in Chapter 3 but in a racetrack configuration, with radius R = 10 μm and directional coupler length $L_c = 10$ μm; an image of the racetrack resonator is shown in Figure 4.1(a). In 1310 nm, the Si waveguides had a propagation loss (measured on test sites) of approximately 1 dB/cm, resulting in a microring intrinsic quality factor of approximately 9×10^5 and a resonance lifetime $\tau \approx 75$ ps (loaded quality factor of 1.1×10^5 at 1307 nm, with a spectral FWHM of 2.1 GHz). As reported in [98], the hybrid silicon laser was created by wafer bonding technology and processed in a CMOS fab [172,173]. The basic principles of such devices are described in [174]. It was used in a bare-die (unpackaged) microchip configuration to generate optically pumped photon pairs and heralded single photons in an external silicon photonic microring resonator. The comparison with a laboratory-grade laser instrument was performed using a narrow-linewidth single-mode tunable diode laser with very low ASE noise (Yenista Optics, Tunics T100-HP-O+). The hybrid laser was used under the same operating conditions as may be expected for classical optical communications, i.e., electrically driven, at room temperature, generating either CW light, or carved into data-carrying pulses, and without frequency locking between the laser and the pair generation (microring) stages. The linewidth of the laser was less than 1 MHz and is much narrower than the ring resonance width, approximately 2 GHz.

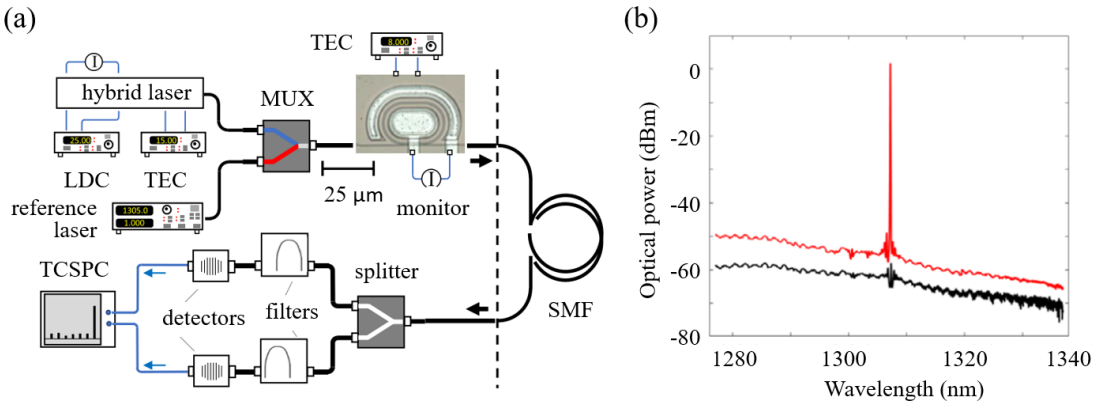

Figure 4.1 (a) The experimental configuration for pair generation. LDC: laser diode controller, TEC: thermo-electric controller, MUX: wavelength-division multiplexer which also acts as a passband filter, and TCSPC: time-correlated single-photon counter. (b) Optical spectrum measured from the hybrid laser (after some coupling losses), operated slightly below (black line) and above (red line) the threshold, shows an amplified spontaneous emission (ASE) floor that is too high for detecting photon pairs generated by the microring. To lower the ASE floor in the desired wavelength windows where pairs will be generated, the MUX shown in panel (a) also acts as a passband filter, as described in the text.

Measurements reported here used the experimental configuration shown in Figure 4.1(a). As shown in Figure 4.1(b), the laser wavelength was around 1307.5 nm, in the "O-band" wavelengths used in short-range (e.g., data-center network) optical communications. The laser delivers more-than-adequate optical power (several milliwatts) for photon-pair generation in silicon microrings. However, the ASE level (even below threshold, black line) was much higher than the optical power of a few mega cps of photons that are typically generated in silicon photonics using milliwatt-level pump powers (10^6 cps corresponds to approximately −100 dBm). Photons generated by SFWM using the peak cannot be detected if they are buried in the sea of ASE noise. Therefore, we need to filter out the ASE by at least 40 dB at the spectral windows where we will generate photons, before the SFWM-generation stage. (It is much harder to reduce the ASE floor of a laser itself by the same magnitude). Since off-the-shelf tunable narrow-band optical filters in the O-band currently show significant insertion loss (2-3 dB), we used a coarse wavelength division multiplexing component, as labeled "MUX" in Figure 4.1(a), which has 6 nm passbands around each "add" input to the "common" port and suppresses out-of-band light by 60 dB. This component filters

the broadband ASE from the hybrid laser outside of the add window, 1308 nm ± 3 nm, and has an insertion loss of about 1 dB (including spliced single-mode fiber connectors).

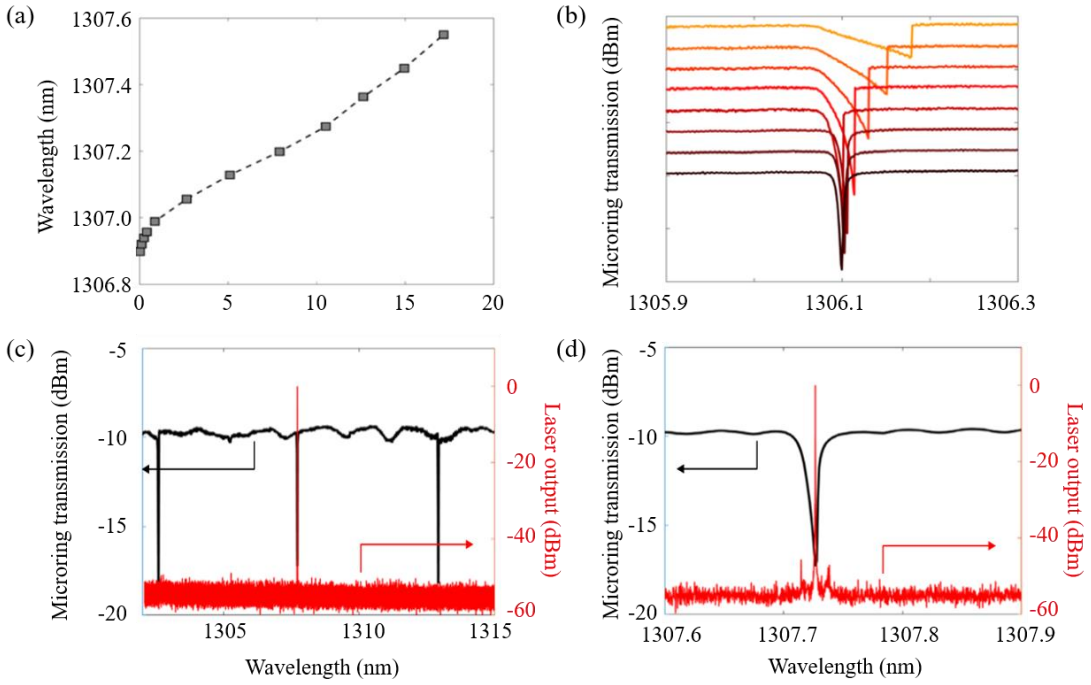

Figure 4.2 (a) Varying the optical power by changing the injection current to the hybrid laser also resulted in changing the output wavelength. (b) Changing the input power to the microring resulted in shifting its transmission spectra, measured at out-coupled power levels ranging from 0.03 mW (−15 dBm: lowest trace) to nearly 1 mW (0 dBm: highest trace) [input powers are 12.6 times (11 dB) higher]. (c) During measurement, the laser wavelength was aligned to one of the microring resonances [shown, over a smaller wavelength range, in panel (d)]; black line: microring spectrum; red line: laser spectrum; both at 1 mW.

The bare-die chips (both the laser and the microring) were mounted on temperature-controlled stages with a TEC in feedback with a thermistor on the stage mount. The hybrid silicon laser was operated using a laser diode controller in constant-current mode. Increasing the optical power via increased injection current also shifted the wavelength as shown in Figure 4.2(a) as is typical for semiconductor microchip lasers. A silicon microring resonator whose quality factor is high enough to align to only the central laser peak [Figure 4.2(d)] and generate a high rate of photon pairs efficiently also shows a power-dependent transmission lineshape [Figure 4.2(b)] in the relevant range of optical powers. To establish a stable resonance, the microring was heated until the selected resonance aligned with the pump laser, as shown in

Figure 4.2(c) and (d). The spectral alignment was continuously monitored during measurement using the reverse-biased photocurrent of the silicon p-i-n junction diode fabricated across the microring [130] and confirmed using high-magnification infrared camera images of the microring. At the same time, the wavelength of the light emitted by the bare-die hybrid laser was monitored from a 10% tap at the output using a wavelength meter, with stability at the single-digit picometer level typically being required in our experiments. Electrical signals were applied to the contact pads on the chips using signal-ground probes controlled by micro positioners. Polarization-maintaining fibers, fiber-loop paddles, and lensed tapered fibers with anti-reflection coating were used to couple light to and from the silicon chip, and nano positioning stages with piezoelectric actuators were used for accurate positioning of the fiber tips to the waveguide facets. The insertion loss of each fiber-to-waveguide coupler on the silicon photonic chip with the microring resonator was estimated as 5 dB averaged over the wavelengths of interest based on transmission through simple waveguides. The output loss of the chip with the hybrid laser is not known since it was cleaved specially for this project (i.e., one-off fabrication). Light was coupled to and from the chips using lensed tapered SMF-28 fibers. Output light from the chip with the microring was split by a wavelength-insensitive 3 dB splitter and routed through cascaded filters (off-the-shelf telecommunications-grade components, albeit with some customization for computer-controlled tunability) to select one pair of spectral lines of Stokes (also called idler) and anti-Stokes (signal) photons positioned symmetrically around the pump wavelength. The desktop filter assembly provided more than 130 dB passband-stopband contrast, and 1.8 nm FWHM bandwidth, with 7 dB insertion loss in each of the two filtering channels. Four single-photon detectors were available for the measurements: two gated InGaAs SPADs and two WSi SNSPDs. The former was thermo-electrically cooled to 233 K, whereas the latter were cooled to 0.8 K in a closed-cycle Helium-4 cryostat equipped with a sorption stage. Characteristics for the InGaAs detectors were as follows: detection efficiency 15%, dead time 10μs, and gated at 50 MHz. The detection efficiencies for the SNSPDs were about 90%; these detectors were free running and operated in a simple dc-biased mode with two-stage RF amplified readout using off-the-shelf

electronics. Coincidences were measured in the same way as in Chapter 3 with acquisition times of 300 s when using the free-running SNSPDs and 900 s or 1500 s when using the gated InGaAs SPADs.

4.3 Measurement

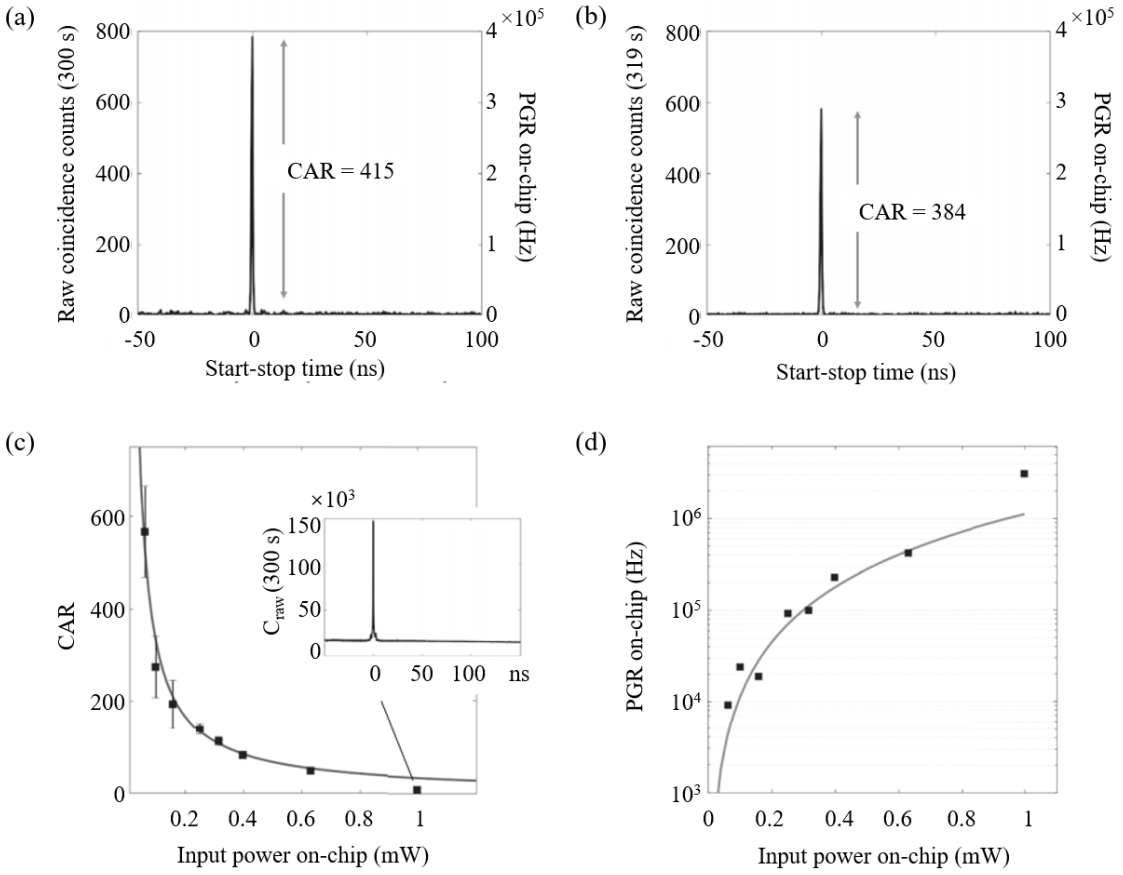

Figure 4.3 (a) CAR for pair generation using the hybrid laser with 1 mW average power, modulated into 80 ps pulses at a repetition rate of 1 GHz and an on-off ratio of about 10. (b) Similar CAR and PGR were measured using the reference laboratory laser. (c) CAR versus power measured using the hybrid laser in the CW mode. The fitted line has the expected functional form P_0^{-1}, except for the last point (highest power) at which the background accidental rate was higher (see inset). (d) The measured coincidence count rate was scaled by losses incurred after pair generation to infer an on-chip PGR. Excluding the last point, fit PGR $= R \times P_0^2$ calculates the pair-generation rate $R = 1.12 \pm 0.11 \times 10^6$ Hz/mW^2.

The characterization measurements compared PGR and two-photon correlation measurements when using the externally filtered hybrid III-V/Si laser to using a reference laboratory laser. As a representative example, Figure 4.3 shows the CAR of photon pairs generated when pumped with 1 mW

(in-fiber power) from the filtered hybrid laser [Figure 4.3(a)] or from the reference laboratory laser [Figure 4.3(b)]. SNSPDs were used for the measurements. In both cases, the pump light for initiating SFWM in the microring was carved using an electro-optic modulator driven by a step-recovery diode [175] into short pulses of duration approximately 80 ps (matching the photon lifetime in the microring resonator). The CAR and PGR for the hybrid laser were comparable to those measured using the reference laser, at similar raw coincidence rates of 1.56 Hz and 1.30 Hz (respectively). The on-chip PGR was calculated from the measured coincidence rate by accounting for the insertion loss of the filters (7 dB), chip-waveguide coupling (5 dB), 3-dB splitter between the chip and filters, and the efficiency of the detectors.

Figure 4.3(c) shows the scaling of CAR and the coincidence count rate versus the input power (P_0) in the bus waveguide on the chip (−5 dB insertion loss was incurred to couple light from the fiber to the waveguide). The uncertainties in C_{acc} and D are one standard deviation values and were propagated to generate the error bars in the CAR plot. The fitted line has the expected [28,135] functional form P_0^{-1}, followed by the measurements except for the last point (highest power) at which the background accidental rate was higher (see inset), indicating an increased likelihood of broken pairs due to free-carrier absorption [33]. Converting the on-chip power to in-fiber power levels (i.e., accounting for the 5 dB loss in coupling from fiber to chip), the horizontal axis of Figure 4.3(c), reported as in-waveguide (on-chip) power, corresponds to measured power levels of 0.3–3 mW in fiber.

In Figure 4.3(d), the (on-chip) PGR is shown as a function of input power in the bus waveguide before the microring. The fitted line, following the functional form $\mathrm{PGR} = R \times P_0^2$, agreed with the data, except at the last point of highest input power, where the accidentals contributed significantly to the peak coincidence value, as shown in the inset to panel (c). The fitted PGR is $R = 1.12 \pm 0.11 \times 10^6$ cps/mW^2. This is a typical value for silicon microrings and is slightly lower than the experimental results tabulated in [113].

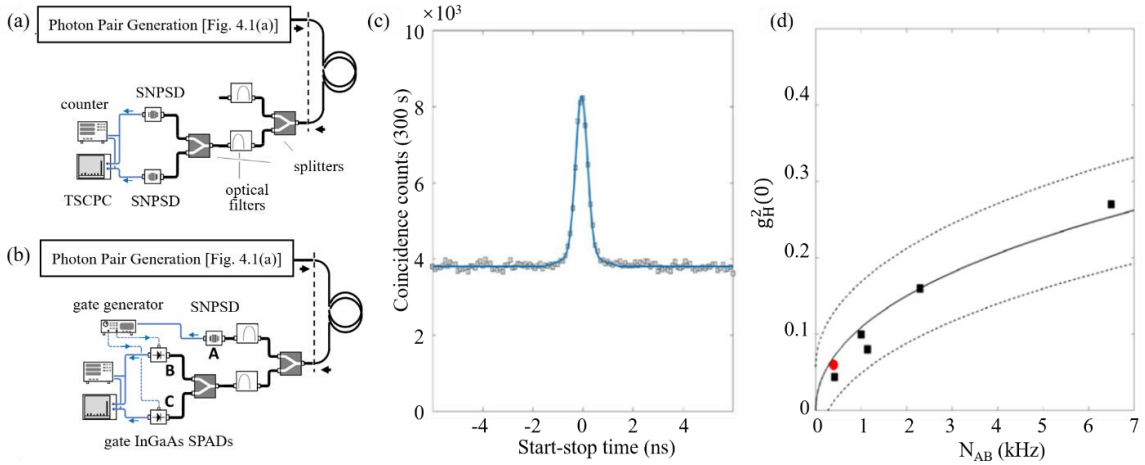

Figure 4.4 (a) HBT measurement of photon bunching of the signal photons, without being conditioned on the detection of the idler (Stokes) photon. (b) Measurement of the (time-averaged) heralded second-order self-correlation function, using gated detectors to reduce the number of accidentals. (c) The measured data and fitted line resulted in $g^2_{\mathrm{HBT}}(0) = 2.09 \pm 0.03$. (d) $g^2_{\mathrm{H}}(0) = 0.06 \pm 0.17$ measured for the hybrid microchip laser (red circle: 0.9 mW power on-chip) agreed with the trend established using the reference laser (black squares). The dashed lines show 90% confidence intervals of the fitted trend.

Figure 4.4(a) shows the experimental configuration for the HBT measurement of photon bunching of the signal photons. For an ideal single-mode source generated by a spontaneous optical nonlinearity in which the heralds are not measured, one should measure $g^2_{\mathrm{HBT}}(0) = 2$, consistent with thermal statistics [33,176]. The measurement was performed with the hybrid laser providing 3 mW in-fiber power, and the fitted data resulted in $g^2_{\mathrm{HBT}}(0) = 2.09 \pm 0.03$, as shown in Figure 4.4(c). A value close to 2 generally confirms the single-mode character of the pair-generation process and absence of pump-induced noise. The coherence time calculated by fitting the peak of Fig. 4(c) with a Gaussian function was $\tau_c = 240$ ps. This value comprises contributions of the coherence time of the cavity SFWM process (150 ps), the effects of the finite binning resolution (100 ps), and the timing jitter of the measurement.

Figure 4.4(b) shows the experimental configuration for measuring the heralded single-photon second-order correlation function, $g^2_{\mathrm{H}}(0)$. The measurement was also performed with the hybrid laser providing 3 mW in-fiber power. Because the InGaAs detectors have a low detection probability, the total number of triple coincidence counts is low and requires several-hour-long integration times with free-

running detectors [176]. We used a gated configuration, in which SPADs were biased for detection only upon the successful detection of a herald photon, thus greatly reducing the number of accidental coincidences, which would otherwise dominate the data [176,177].

Results for the reference laser (black squares) and the microchip hybrid laser (red dot) are shown in Figure 4.4(d), with the latter point being $g^2(0) = 0.06 \pm 0.17$ and being consistent with the trend established by the reference laser. The errorbar is one standard deviation uncertainty in the fit to the lineshape of $g^2(\tau)$, using the functional form defined by Eq. (12) in [154]. At present, only a single measurement value could be reliably obtained for the hybrid laser because of wavelength drifts over the relatively long acquisition times, a problem not present in the reference laser. The raw heralding efficiencies were 0.05% for hybrid laser and 0.15% for the reference laser, showing heralding efficiency was about a factor of 3 worse for the hybrid laser. After accounting for the additional loss incurred by photon "(B)" in the filters and out-coupling from the chip, the heralding efficiencies were 1.4% (hybrid laser) and 4.3% (reference laser). These are typical values for SFWM sources and require active multiplexing schemes to raise the heralding rates significantly [80,178–181].

4.4 Discussion

Taken together, these measurements establish that the microchip hybrid silicon laser, after ASE filtering, can generate photon pairs and single-mode heralded single photons in silicon photonics with a low multi-photon probability and has the obvious advantages of small size and wafer-scale manufacturability for applications that may need these attributes.

Summarizing the results discussed here, 130×10^3 photon pairs per second can be generated, with CAR > 100, at about 0.34 mW optical pump power and anti-bunching upon heralding with a low value of the second-order intensity correlation function. SFWM in a resonant Si micro-resonator only needs a small fraction of the pump power that can be generated from the hybrid laser, whereas typical optical pump power levels used in the crystal waveguide or fiber-based SFWM pair sources are higher than a few milliwatts and

may not be compatible with hybrid lasers. Thus, the silicon microring resonator is well-matched to the silicon hybrid laser for creating an integrated pair source device. These measurements also highlight the need, if complete chip-scale integration is to be achieved, for optical filtering before the pair generation stage, which has not yet received as much attention as filtering after pair generation [137]. Integrated silicon optical filters have been used in pair-generation experiments at telecommunication wavelengths [137]; however, less attention has been paid to the design and integration of the high extinction ratio, large free spectral range tunable integrated filters at 1310 nm (corresponding to the laser used here and used in data center networks), rather than at 1550 nm. In these experiments, we used a separate fiber component (a passband filter) between the laser chip and the microring chip.

4.5 Summary

In conclusion, the characteristics (e.g., the optical power level, laser linewidth, etc.) of the bare-die hybrid laser were adequate for SFWM in our microring resonators and required only modest, table-top temperature and drive current stabilization using off-the-shelf instruments. However, the hybrid laser required filtering of the broad-spectrum ASE before initiating SFWM in the microring resonator, with an out-of-band extinction ratio of 40 dB or more and a single passband (see Section 4.2). Without filtering, the ASE was at too high of a background level to measure the generated rate of photons.

Given that, photon pairs and heralded single photons at fiber-communication wavelengths may be generated at room-temperature using the same technology for electrically pumped hybrid silicon lasers as intended for classical optical transceivers. Large-scale quantum communication and computing systems will require hundreds to thousands of elemental components such as sources, logic gates, and detectors [165,182]. It is infeasible to divide and distribute a photon stream from a single source to such a high degree. Compact, electrically driven, high-quality photon-pair and heralded single photon sources built using integrated optics may help realize large-scale distributed quantum communication and computing systems. Using a single manufacturable silicon-based photonic platform may help meet these goals using

cost-effective high-volume manufacturing and provide a pathway to integration with microelectronics for overall system functionality.

Chapter 4 contains the material as it appears in the following of which the dissertation author was the secondary investigator: Xiaoxi Wang, Chaoxuan Ma, Ranjeet Kumar, Pierre Doussiere, Richard Jones, Haisheng Rong, and Shayan Mookherjea. "Photon pair generation using a silicon photonic hybrid laser." APL Photonics 3, no. 10 (2018): 106104; Xiaoxi Wang, Chaoxuan Ma, Ranjeet Kumar, Pierre Doussiere, Richard Jones, Haisheng Rong, and Shayan Mookherjea. "Photon pair generation using silicon photonic microring and hybrid laser." In CLEO: Applications and Technology, pp. JTh5C-6. Optical Society of America, 2017.

Chapter 5
Photon Pair Sources in the Network

QKD might be the most mature quantum information technologies today, which guarantees the unconditional security of key distribution via quantum mechanics. A lot of recent research efforts have been devoted to integrating QKD and other quantum communication technologies into the existing communication infrastructures. In this chapter, we investigate the feasibility of integrating silicon microring photon pair sources into the current optical fiber networks by leveraging a fraction of high-speed optical transceiver as pump in the SFWM process (Section 5.1) and exploiting the device's capability of multiplexed generation of photon pairs at both telecommunication bands, i.e., 1310 nm and 1550 nm bands (Section 5.2).

5.1 Photon Pair Generation by a Fraction of a 10 Gbps Data Stream

While some integrated microchip QKD transmitters have been demonstrated, those based on silicon photonics rely on a separate external laser [56,183–186] whereas integrating the laser either requires advanced active-passive III-V semiconductor fabrication [171] or hybrid Si photonics [172]. External-cavity laser diodes and mode-locked lasers which are used in many SFWM experiments are large, expensive and power-hungry devices, compared to the microring resonator, or the small integrated-optics components inside a typical optical communications transceiver used in fiber-optic networks. Wafer-scale fabricated hybrid III-V/Si lasers have been used as the pump (see Chapter 4 or [187]), which makes the implementation more compact and less expensive, but the fabrication is a specialized process and complete integration yet has to be achieved [172]. Co-packaging a laser with integrated optoelectronics is difficult and is one of the most expensive parts of optical transceiver technology [188].

Here we shows that it is possible to do so without a dedicated laser, using instead a fraction of a 10 Gbps non-return-to-zero (NRZ) data stream as an optical pump source for photon pairs and heralded single photons, which have applications in entanglement-based QKD, quantum repeaters, memories and quantum

optical computing. There are millions of such channels in optical communications and data center networks, many of which can spare a bit of extra headroom, at least for brief durations. A fraction of a classical communications channel between two off-the-shelf SFP+ transceivers was tapped (i.e., a small fraction was diverted) and used for photon-pair generation in a silicon microring device (see Figure 5.1). The average power level of the pump before the microring was -5.5 dBm, which is a small fraction of the typical 0 dBm power level used in a classical communication link. The untapped light is free to continue to establish the classical link. Our result shows that many of today's optical networks may be able to conveniently generate quantum resources such as heralded single photons on a massive scale, without requiring purchase, installation and maintenance of dedicated lasers, which are among the most costly and least reliable components in an optical communications link.

5.1.1 Experimental Details

The two computers involved in the classical communication were PC workstations [see Figure 5.1(a)], running a standard operating system, with plug-in PCI-e network interface cards (NICs) supporting plug-in 10 Gbps SFP+ transceivers with single-mode fiber pigtails for optical communications near 1.55 μm wavelengths. The eye diagram of the classical channel is shown in Figure 5.1(b) (receiver jitter has not been deconvolved) and exhibits a few tens of picoseconds of jitter, typical in transceivers compliant with IEEE 802.3 and similar standards. Off-the-shelf DWDM-grade SFP+ transceivers were used in both NICs, whose wavelengths were discretely tunable in steps of 50 GHz. The discrete wavelength step is much larger than the linewidth (approximately 2 GHz) of the silicon microring resonators used in this experiment, and therefore, the precise wavelength alignment was achieved by tuning the microring, not the transceiver. The microrings can be tuned thermally over several tens of nanometers in wavelength, so the precise wavelength of the transceiver is not important. The design of the silicon microring can be found in Section 3.2. The micro-resonator's loaded-cavity photon lifetime (76 ps) approximately matches the pulse duration of a 10 Gbps NRZ data stream, and the classical bits have the appropriate time duration for SFWM pumping.

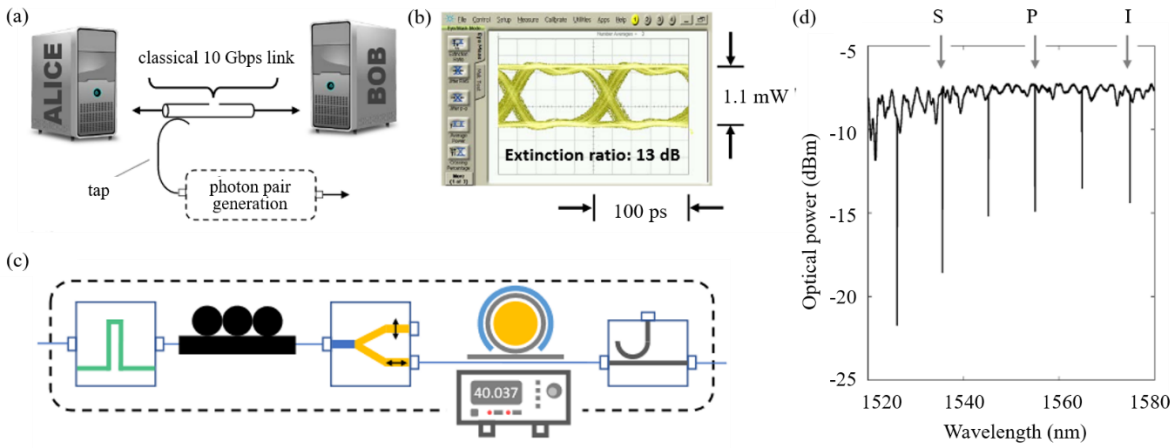

Figure 5.1 (a) A fraction of a 10 Gbps NRZ data stream is used to perform photon-pair generation using a silicon microring. (b) Eye diagram of the classical data stream. (c) Microring transmission resonances showing the locations of the pump (P), signal (S) and idler (I) resonances used in this experiment. (d) The experimental setup for photon pair generation. ASE: amplified spontaneous emission. TEC: thermo-electric controller.

The experimental configuration including ancillary telecommunications components is shown in Figure 5.1(d). Details of the edge-coupling setup is the same with that in Section 3.2. Filters and polarization controllers have already been integrated into a silicon photonics platform for classical optics applications, and may be a convenient future simplification. The temperature of the microchip was maintained slightly above room temperature and the TEC was used to bring the microresonator into stable spectral alignment with the wavelength of the incoming data stream used as the optical pump for SFWM. The state of polarization of the input data stream, though not actively controlled, was quite stable over a duration of several tens of minutes. Variations in the state of polarization change the generated rate of the signal and idler photons similarly, and may not affect certain applications such as QKD except in time-to-completion. For applications where a uniform brightness of photon pairs must be sustained, an active polarization controller or tracker should be incorporated into the chip or system design. The ASE background of the input light from the transceiver was suppressed at the wavelengths to be used for pair generation (i.e., the signal and idler wavelengths) using a relatively broad bandpass filter (FWHM of 1 nm at 1550 nm). The level of ASE background in a communications link varies widely with the specific implementation; however, let us assume, for the sake of performing a quick estimation, that the ASE level is about -50 dBm.

A rate of generated photons at 1.55 μm wavelengths of 100 MHz translates to an average power level of about -79 dBm. Thus, it is important to suppress the ASE background at the signal and idler wavelength spectral windows by at least 40 dB, in this representative example, in order to be able to detect the photon pair above the background of photons already present from ASE. While a dedicated optical filter was used in this experiment, a WDM add/drop element, widely used in practical networks, would achieve the same result [98]. For these experiments, signal and idler wavelengths near 1535nm and 1575 nm, respectively, were selected for convenience, since such photons can be easily separated using a standard telecommunications C/L band splitter component. Photons were detected using two fiber-coupled SNSPDs with detection efficiencies measured to be about 90% at 1550 nm wavelengths, with a timing jitter FWHM of about 130 ps. Cryogenically-cooled detectors are expensive to build and operate, but quantum communication protocols such as MDI-QKD can be implemented by placing detectors (without transmitters) only at interior nodes of the network, and inexpensive transmitters (without detectors) at the edges. Coincidences were measured using a multi-input TDC instrument, with a 0.16 ns bin width.

5.1.2 Measurements

5.1.2.1 Singles and Coincidence Rates

Figure 5.2(a) shows the scaling of the singles rates for the signal and idler photons as a function of the average pump power, i.e., the average power of the 10 Gbps NRZ data stream used as the pump. These are the raw measured singles rates, and include uncompensated experimental loss contributions (-5 dB loss for coupling from the microchip to fiber, -7 dB insertion loss from filters, -1.9 dB detector efficiency); the on-chip singles rates are about 14 dB higher. As expected [33], the scaling of the singles rates is quadratic with the average pump power. The scaling of the (loss-compensated) coincidence rate is shown in Fig. 2(b) and follows the expected quadratic trend (the vertical axis is shown on a logarithmic scale), until a drop-off was noticed at higher pump powers, most likely due to free-carrier absorption and /or thermal detuning of the microring resonator. The fitted efficiency of pair generation was 14.6 MHz/mW^2, which is not the record result [25], but is comparable to most other reports of SFWM in silicon microrings (see Table 3.1).

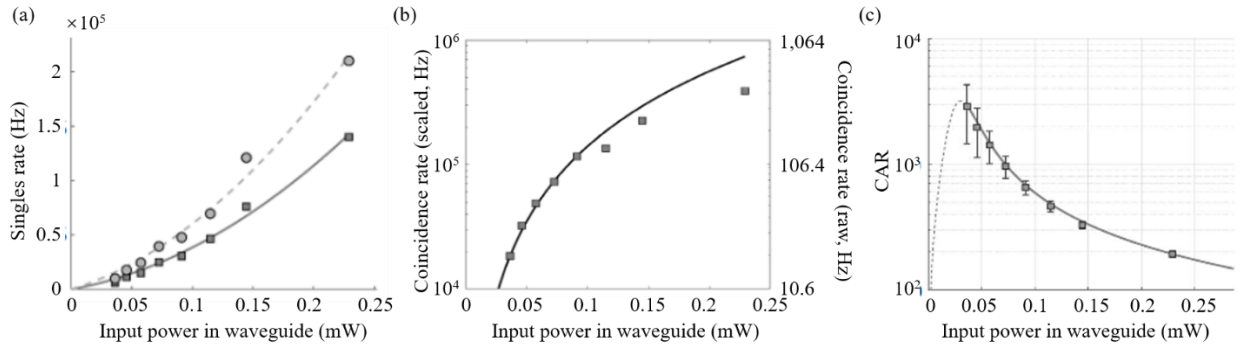

Figure 5.2 (a) Singles rates (raw measurements) versus average input power in the bus waveguide. (b) Coincidence rate (scaled by losses, approximately -14 dB in each of the signal and idler photon pathways) versus average input power in the bus waveguide. The indicated fit, excluding the last few points, and shown by the solid line, is used to infer the PGR. The right-hand side vertical axis reports the measured (raw) coincidence rates. (c) CAR versus average input power in the bus waveguide.

5.1.2.2 CAR

Figure 5.2(c) and Figure 5.3 report the measurements of CAR versus input average pump power. Each histogram peak was fitted by a Gaussian function, whose FWHM was typically 0.31 ns, as shown by the representative example in Figure 5.3(b). The histogram of start-stop coincidences (measured bin counts divided by the measurement time in seconds) which resulted in the highest CAR is shown in Figure 5.3, along with a segment of the accidental coincidences in the inset figure. The highest CAR was 3,000 ± 500 measured using an integration time of 3,000 seconds. As expected, CAR decreased at higher pump powers, with a fitted trend shown in Figure 5.2(c). The fit is based on the ratio-of-polynomials functional form $\mathrm{CAR} = P(aP^2 + bP + c)^{-1}$ which, at low pump powers, saturates at a certain maximum value and then drops to zero [161]. Other fitting forms have been used in the literature, which do not show evidence of CAR saturating at low P values, and sometimes, the saturating and non-saturating behavior can be seen for the same device at different wavelength regimes [189]. Here, we use the functional form that recognizes that, in an optical communications network, "true" coincidences generated by very low pump powers are likely to be masked out by the imperfectly-filtered background ASE level, since optical filters do not have infinite extinction ratio, and thus CAR should be low as P_0 decreases further. For clarity, the extrapolation of the fit to the regime of lower pump powers than was actually used is shown in Figure 5.2(c) by the dotted

line. At the higher end of the pump powers used in these measurements (which were much less than 1 mW, or 0 dBm, the typical average power level of a data stream in an optical network), the error bars in the calculation of CAR were lower because the singles counts were higher. At an average input pump power of 0.23 mW, a CAR of 193 ± 11 was measured. While there is no fixed rule on what CAR values should be, values in excess of 50 have been recently considered satisfactory for typical applications of photon pairs in communications and QKD [137]. These measurements, based on optical pumping by a 10 Gbps data stream, are reassuringly similar to well-known trends and quantitative values in pair generation using silicon photonic microrings pumped by laboratory-grade diode laser instruments [83,137,153]. These measurements show that high-quality pair generation can be obtained by tapping a 10 Gbps NRZ data stream from an optical network, with sub-milliwatt average power levels, to serve as the pump.

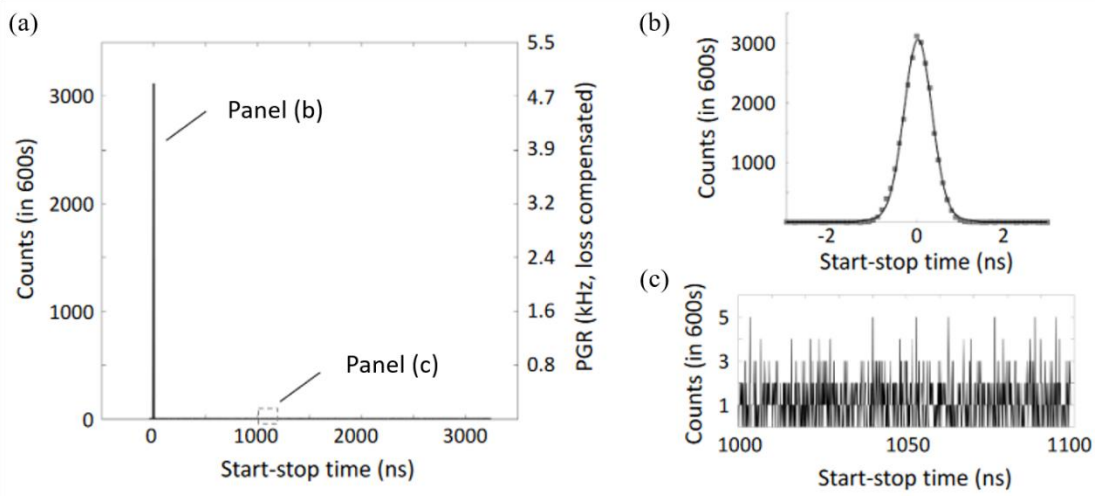

Figure 5.3 (a) Start-stop histogram for the measurement with the highest CAR value, 2873 ± 1415. (b) Plot of the coincidence peak. (c) A section of the accidental coincidences trace, showing the low level of background noise in the measurement.

5.1.2.3 HBT Measurement

Figure 5.4(a) shows the schematic for the measurement of the single-photon second-order self-correlation function, $g^2(\tau)$. Coincidences were defined as simultaneous detections within a 5 ns time window. One of the photons in the SFWM pair is detected in path 'A' as labeled in the figure, and may, or may not, be used as a 'herald' for a coincidence measurement. If heralded, the remaining single photon is

expected to be anti-bunched, whereas when the signal arm is measured without regard to a herald, the photon is expected to be bunched [79] as shown by the start-stop statistics in Figure 5.4(b). The peak value, $g^2(0) = 2.21$ is close to the expected value $g^2(0) = 2$ for a single-mode thermal state [190]. Generally, the impact of SNSPD timing jitter is to lower the peak value of $g^2(0)$ [191]. Evidence of weak super bunching indicates that some of the two-photon coincidences arise from more than one path way, and have been observed in experiments on pseudothermal light generated by intensity-modulated, rather than CW, light incident on rotating-glass plates [192]. The TDC instrument performs these calculations in real-time with no post-selection; however, a very long acquisition time is needed for an accurate $g^2(\tau)$ measurement, which is currently limited here by the polarization and/or coupling drifts of the fibers to the unpackaged silicon photonic microchip. For comparison, Figure 5.4(c) shows the HBT measurement for the SFP+ light (without pair generation) attenuated to the single-photon level (-100 dBm), resulting in singles count rates of about 1.25×10^5 cps, and no evidence of bunching is seen.

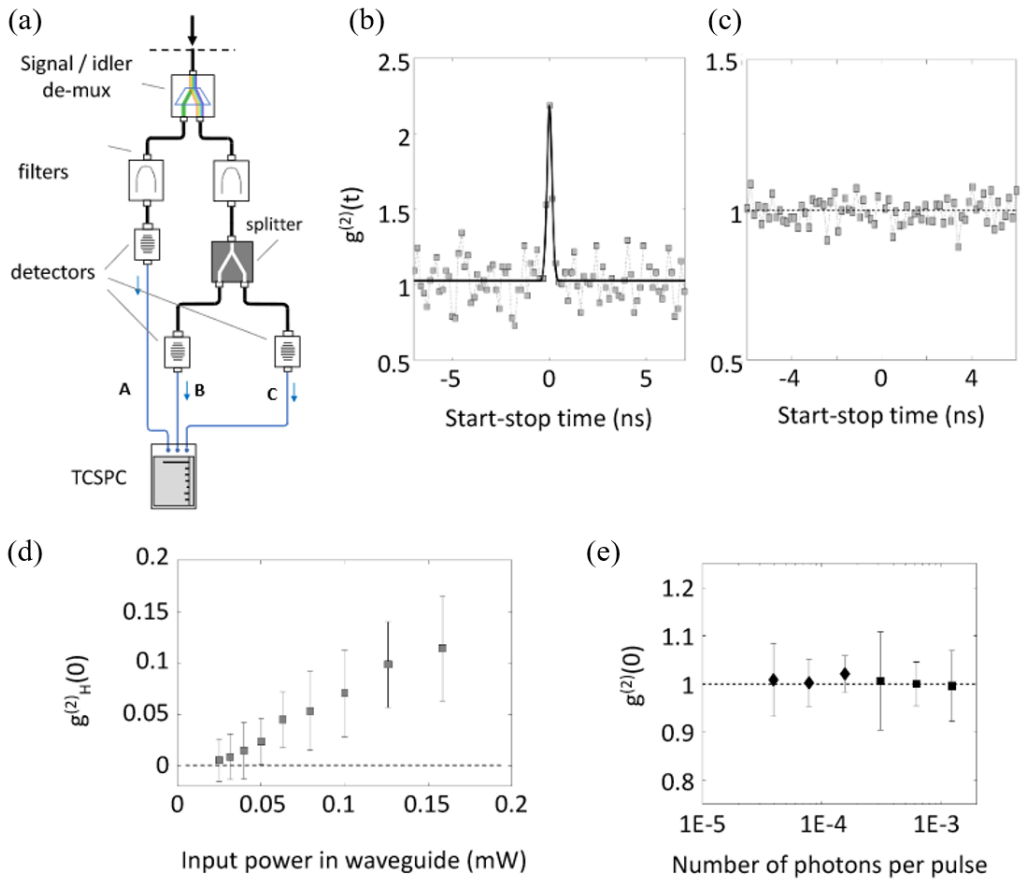

Figure 5.4 (a) Schematic of the measurement setup for second-order auto-correlation statistics on the signal photon. (b) For the unheralded measurement, $g^2(\tau)$ shows characteristic bunching, with a peak value slightly exceeding the expected value of 2.0. (c) No bunching is seen for the light from the transceiver data stream, attenuated to single-photon levels. (d) The heralded (by the idler photons) second-order autocorrelation of the signal photons at zero time difference, $g^2(0)$, decreases with pump power and since $g^2(0) \ll 0.5$, shows evidence of (heralded) single-photon character. (e) In comparison, $g^2(0) \approx 1.0$ for the light from the transceiver data stream itself, as expected.

5.1.2.4 Heralded Single-Photon Generation

Figure 5.4(d) shows the scaling with pump power of the heralded (i.e., conditional) single-photon second-order self-correlation function, $g_{\mathrm{H}}^2(0)$. Counting times varied from 100 seconds for the higher pump powers to 600 seconds for the lowest pump power. The scaling trend seen in Figure 5.4(d) is consistent with results obtained for pumping SFWM in the microring resonator with a laboratory CW laser, and $g^2(0)$ is proportional to the biphoton rate [154], which, in SFWM, is quadratic in the pump power, P, at low values. At the highest average power values (0.15 mW) used in this sequence of measurements, $g_{\mathrm{H}}^2(0) = 0.11 \pm$

0.051 at a heralding rate of $R_{\mathrm{A}} = 340$ kHz, showing deeply sub-Poissoinian statistics. This is already well below the classical threshold. Even lower values, as low as $g_{\mathrm{H}}^{2}(0) = 0.005 \pm 0.02$ were directly measured for a measured heralding rate of $R_{\mathrm{A}} = 18$ kHz. The heralding efficiency is about 3–4%, unchanged from our previous experiments for this microring [25] and can be improved by changing the coupling coefficient between the microresonator and the bus waveguide, and lowering the insertion losses of the filters and detectors [83]. For comparison, Figure 5.4(e) shows the $g^{2}(0)$ statistics of the light from the data stream itself, attenuated using external fiber-coupled attenuators to the single-photon regime, as would be used in a BB84-type QKD protocol and similar applications. Data shown using squares were obtained by measuring photons using the setup and calculation procedure resulting in panel (d) and described in the preceding paragraphs. Data shown using diamonds were measured from the setup used in panel (c), i.e., the HBT measurement which resulted in a feature-less $g^{2}(\tau)$ profile, as shown in Figure 5.4(c), and whose values were averaged over the central 10 ns time window. The number of photons "per pulse" was calculated from the average power level (average power levels before the detector for the indicated points range from -94 dBm to -106 dBm) and with respect to the bit period (100 ps) of the 10 Gbps data stream, multiplied by 2 since one-half of the bits are '0' and do not contribute to the average power). These measurements show Poissonian statistics. Thus, heralded single photons can be generated by pumping a silicon microring resonator with a tapped fraction of a classical 10 Gbps NRZ data stream. As Figure 5.4(d) shows, about one-tenth of a milliwatt needs to be extracted from the classical data stream, leaving the rest of the light to complete the classical link. Together with the high CAR values, this suggests that information for optical communications can be cleanly encoded on single photons, with only a small possibility that a receiver will detect two or more signal photons when triggered by a single herald, or that the detected signal and herald (idler) photons will be counted across the "wrong" time bins. These observations suggest that such photon pairs could be useful resources for quantum communications in optical networks.

5.1.2.5 Comment on Energy-time Entanglement

The generated photon pair could be used in energy-time entanglement; however, we do not yet have a simple method of verifying such entanglement. One popular method is through a Franson-type two-photon interference experiment, by violating Bell's inequality [54,55] (see details in Section 1.1.1). However, we cannot verify entanglement when pumping the SFWM process with a 10 Gbps NRZ data stream. As shown by the eye diagram in Figure 5.1(b), the average duration of the pump pulse which performs SFWM in the microring is somewhat shorter than 0.1 ns, the bit period, and thus, the time difference between the "short" and the "long" arms of the time-bin Franson interferometer would have to be significantly shorter than 0.1 ns, and the histograms of the two bins would also need to be cleanly resolved. However, the binning resolution of the apparatus used in these measurements is 0.16 ns, and the timing jitter of the detectors is about 0.13 ns. Consequently, the fitted FWHM values of the coincidence peak, shown in Figure 5.3, is currently about 0.3 ns, which is much larger than the bit period. We cannot yet measure the visibility of the coincidence fringe (as a function of the phase delay) in the Franson interferometer, but hope to report on it in the future by using reduced-jitter detectors and electronics, which have already been reported in the literature [193,194]. Using the silicon microring with CW or slower repetition-rate pumping (e.g., 1 GHz), high values of Franson visibility (>98%) have been demonstrated for the same microring resonator used in Chapter 3 .

5.1.3 Conclusion

These results show that the photon pairs generated by initiating SFWM using a 10 Gbps NRZ data stream as the pump were sufficient in quantity and quality in comparison with results previously obtained using a stand-alone laser. Si microring resonators can be designed such that their pump power requirements for SFWM are compatible with a tap fraction of a typical classical communications data stream, which has an average power of about 0 dBm. The microresonator photon lifetime approximately matches the pulse duration of the 10 Gbps data stream, and thus, the NRZ classical bits are already carved into the appropriate time duration for near-optimal SFWM pumping. SFWM itself is a random process, and therefore, it is not

of concern that a PRBS classical bitstream serving as the pump does not have a “1” pulse deterministically in every time slot, unlike, say, a mode-locked laser serving as the pump. The use of (relatively inexpensive) silicon photonics and the elimination of the separate pump diode requirement show progress in the same spirit of cost reductions and simplifications of practical quantum photonics devices using existing telecommunications technology.

5.2 Dual-Band Photon Pair Generation at 1550 nm and 1310 nm

Since there are two spectral bands which are widely used in classical communications, a pair generation device should ideally be able to operate in both spectral ranges where initial applications of quantum communication (e.g., QKD) may be implemented. Moreover, an argument has been made, in the context of fiber experiments, for generating and using quantum photons at 1310 nm [195,196] which is less widely studied than the 1550 nm band. Traditional entangled photon pair generation devices are formed using optical fiber [94] or crystals such as PPLN, KTP, lithium tantalite, etc. [81,91,149,150,197]. Crystals themselves have a wide transparency range, and can be used at various wavelength ranges including visible, near-infrared and portions of the mid-infrared spectrum as well. In crystals, the generation of photon pairs at both bands simultaneously and without cross-correlations has not been shown. Operation at distinctly different wavelength bands in the same device is difficult, since periodically-poled gratings phase-match efficiently over only a narrow band of wavelengths, and gratings, in general, have higher-order resonances that may scatter light and impair the performance. For quantum communications using integrated photonics components, it is not yet clear which spectral band is preferred in the deployed fiber links where both C/L-band (approximately 1530–1600 nm) and O-band (1310 nm) wavelengths are used. Some communications schemes, such as passive optical networks, use both wavelength bands [198]. As discussed in [199], the Raman noise incurred in fiber propagation at 1310 nm wavelengths can be significantly (about 4000 times) weaker than at 1550 nm; however, the propagation loss (fiber attenuation) can be higher. In terms of device technology, there are more WDM components (splitters, filters, MUX/de-MUX etc.) available at 1550 nm, but the standard channel spacing at O-Band is wider, making filtering easier, which is one of the most

challenging requirements for integrated photonics. Thus, it is not clear which is the preferred wavelength regime for operation of a microchip pair-source intended for compatibility with short-distance fiber communications. The detector efficiency of single-photon detectors, particularly, avalanche diode detectors, also varies strongly with wavelength, and dark-count reduction may be achieved by operating in the O-band. Hence, researchers have developed pair sources at both wavelengths, for example [200] in the C-band and [201] at the O-band. In fact, devices using SPDC can generate a photon pair with one photon at 1550 nm and the other at 1310 nm, and thus, one photon can serve as the herald for the other [202–204]. While this is not possible in silicon photonics because of the comparatively-narrow band nature of SFWM phase-matching, we demonstrate that a single microring resonator can, in fact, generate entangled photons of high quality at each wavelength band separately. This is not an obvious result, in the sense that the modal properties of silicon nanophotonic waveguides, and the coupling behavior of micro-resonators to waveguides, are strongly wavelength-dependent in high-index-contrast silicon photonics [205]. The use of a single device which can operate at either wavelength regime, as desired, is important to reduce the device fabrication/yield variability, which is still a significant concern in foundry-fabricated silicon photonics, especially with high-Q micro-resonators that require an optimized coupling to a waveguide for optimum operation [113]. Here, we address one of the existing limitations of silicon photonic pair generation devices: the difficulty in generating high-quality entangled photon pairs at both 1310 and 1550 nm wavelength bands that are widely used in optical communication networks and components.

In this section, a simple device is measured and characterized which generates a high quality of entangled photon pairs at both these wavelengths simultaneously, when two optical pumps are introduced. The structure also works as a “regular” pair generation device when only one pump is used, and in fact, one of the measurements reported here is that of a CAR of 19 000 which is the highest CAR value yet reported for silicon photonics pair generation in any device, at any wavelength. Moreover, by separating the two pump wavelengths by more than 200 nm, this device helps meet the ongoing challenges of multiplexing and scaling up photon pair generation, and avoid the difficulties and impairments (such as cross-pump

interactions) faced in two pump SFWM processes when the two pump wavelengths are close to each other [153]. The underlying technical challenge is to design a silicon photonic pair generation structure that can operate at these rather different wavelengths. Firstly, compared to diffused/ion-exchanged waveguides in glass, or optical fiber, the GVD of silicon waveguides is very high (by three or four orders of magnitude). Thus, not only is a Si waveguide much less efficient than a PPLN waveguide, but it is more dispersive as well. Secondly, dual-band micro-resonators with a clean transmission spectrum (showing suppression of multi-mode effects) are uncommon (but, as shown here, not impossible), since components, materials and cross-sections are typically optimized around one wavelength. What is required is six-fold resonance at pump, Stokes, and anti-Stokes wavelengths of SFWM process at both bands, which would be very difficult to design and to operate in a stable manner for traditional nonlinear resonator devices using III–V semiconductors [206] or periodically-poled crystal waveguides. As shown here, the high-index contrast of silicon photonics, coupled with the ability of silicon microfabrication techniques which allow for precise and repeatable fabrication, results in devices that show clean, essentially single-mode transmission spectra at both 1310 and 1550 nm wavelength bands. Also, the ability of silicon (a semiconductor) to incorporate microelectronic components such as monitoring p-i-n diodes within the microring itself allows for monitoring and alignment of the resonance to the pump wavelengths, was essential for stable operation and the measurements reported here.

5.2.1 Experimental Details

The simple device used for simultaneous dual-band entangled photon pair generation is a high Q-factor all-pass microring, side-coupled to a single waveguide, with an appropriately-chosen coupling coefficient as described below. The design details of the microring can be found in Section 3.2. Simulations of $|\kappa|$ versus wavelength (λ) at both the 1550 nm and 1310 nm wavelength bands are shown in Figure 5.5(a) and (c), respectively, for the lowest-order quasi TE polarized electrical field. A small value of $\kappa \ll 0.05$ is one of the two necessary components for achieving a high loaded Q-factor, and thereby, bright pair generation, with the other factor being the loss of the waveguide.

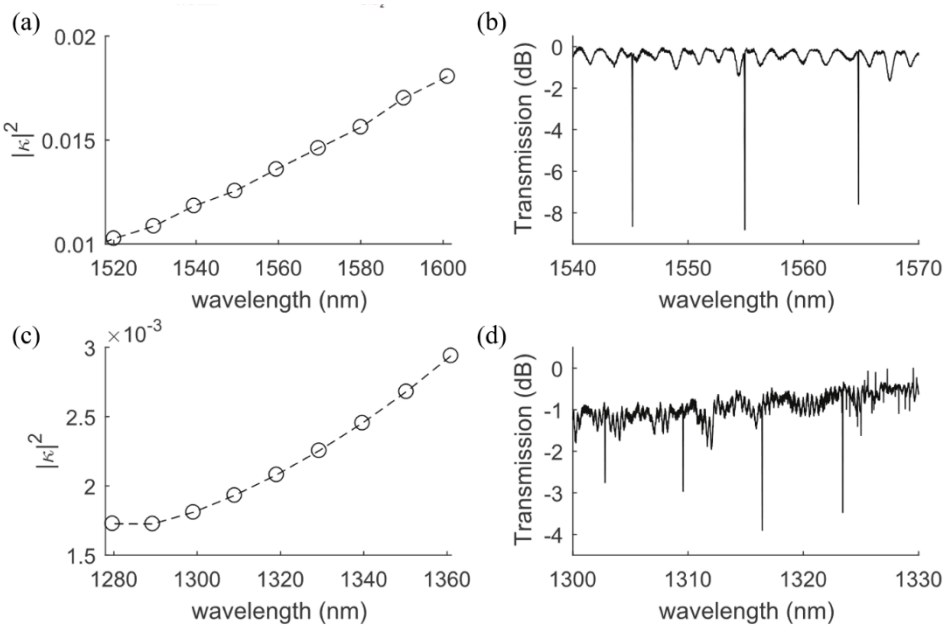

Figure 5.5 (a) and (c) are FDTD-simulated coupling efficiency calculations $|\kappa|^2$ as a function of wavelength at 1550 nm and 1310 nm bands respectively. (b) and (d) are the measured transmission spectra at 1550 nm and 1310 nm bands, respectively, showing a single-mode-family set of resonances at both bands in the same device.

The silicon waveguides used in the feeder waveguide and microring had a propagation loss (measured on test sites consisting of waveguides of different lengths) of approximately 0.74 ± 0.02 dB/cm at 1550 nm and 1.13 ± 0.12 dB/cm at 1310 nm, resulting in: (a) at 1550 nm, an intrinsic Q-factor of approximately 9×10^5, and a resonance lifetime $\tau \approx 76$ ps (loaded Q-factor of 9.2×10^4, with a spectral FWHM of approximately 2.1 GHz); and (b) at 1310 nm, an intrinsic Q-factor of approximately 3×10^5, and a resonance lifetime $\tau \approx 40$ ps (loaded Q-factor of 5.7×10^4, with a spectral FWHM of approximately 4.0 GHz). A "clean" transmission spectrum was measured at both wavelength bands, as shown in Figure 5.5(b) and (d). Recall that the overall Q-factor depends on both the intrinsic propagation loss of the waveguide forming the microring and the coupling coefficient between the microring and the waveguide. Here, the slightly higher propagation loss at 1310 nm is somewhat compensated for by the smaller waveguide-to-ring coupling coefficient, as shown in Figure 5.5(a) and (c). Thus, a similarly high Q-factor is achieved at both wavelength bands.

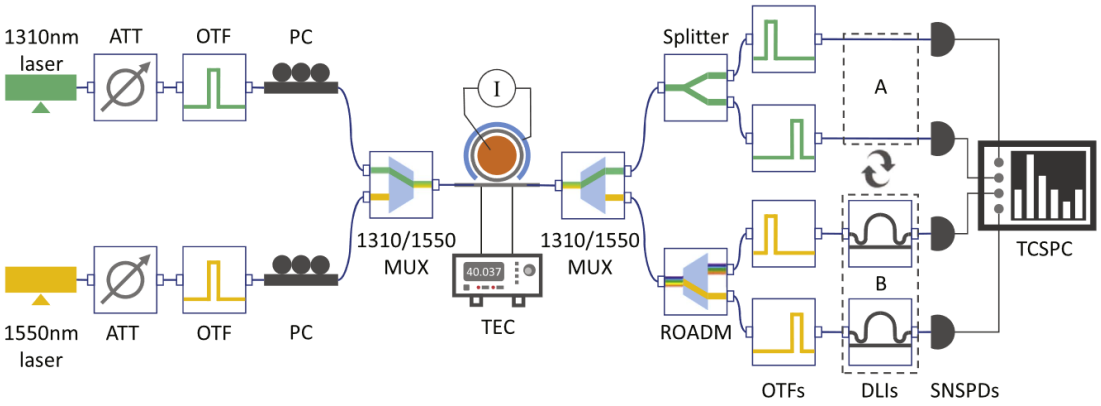

Figure 5.6 Experimental setup for pair generation and measurements of the cross-correlation between signal and idler photons i.e., CAR, and two-photon Franson interferometry visibility. For the CAR measurement, all the SNSPDs connected directly to the filters (Box B was replaced by another Box A). For the visibility measurement, Box B was used to measure the fringe visibility of photon pairs generated by one pump, as described in the text, while Box A simply connected filters and detectors to monitor the photon count rates generated by the other pump and measure their CAR. ATT: variable optical attenuator, OTF: optical tunable filter, PC: polarization controller, MUX: multiplexer, TEC: thermoelectric controller, ROADM: 3-port reconfigurable optical add-drop multiplexer, DLI: delay-line interferometer, SNSPD: superconducting nanowire single-photon detector, TCSPC: time-correlated single-photon counter.

Photon pair generation measurements reported here used the experimental configuration shown in Figure 5.6. The bare-die chip was mounted on a temperature-controlled stage with a thermoelectric controller in feedback with a thermistor on the stage mount. The spectral alignment of the pump laser(s) to the microring was continuously monitored during measurement using the reverse-biased photocurrent of a silicon p-i-n junction diode fabricated across the microring [130], and confirmed using high-magnification infrared camera images of the microring. Figure 5.7(a) shows infrared camera images of the microring at the resonance conditions of the two pump lasers, operated individually and simultaneously. Because of the limited dynamic range of the camera, it was difficult to quantitatively distinguish the third case from the first two; however, the photocurrent readout with two pump lasers was seen to be a linear sum of the photocurrents for the two individual lasers.

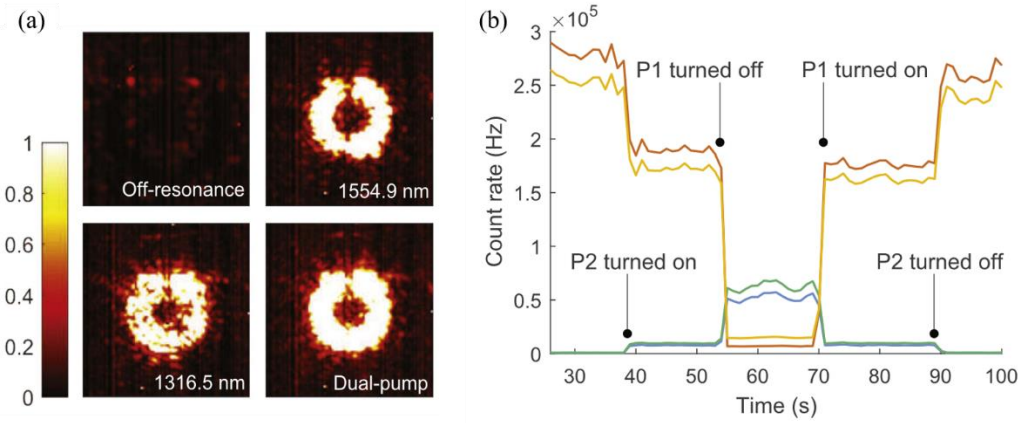

Figure 5.7 (a) Infrared camera images, acquired using a top-view microscope and a high-magnification objective lens, of the microring off-resonance and resonating with 1554.94 nm pump light, with 1316.52 nm pump light, and with both wavelengths simultaneously. (b) Measured singles count rates as the second pump is turned on and off, after the first. P1 and P2 are 1550 nm and 1310 nm pumps respectively. Red and yellow lines are single counts for 1550 nm signal and idler photons; green and blue lines are those for1310 nm signal and idler photons.

Light was coupled to and off the silicon chip using polarization-maintaining fibers, polarization controllers, and lensed tapered fibers with anti-reflection coating. The latter was designed for C-band, but functional for O-band as well. The insertion loss of each fiber-to-waveguide coupler was estimated as 3.5 dB. Nanopositioning stages with piezoelectric actuators were used for accurate positioning of the fiber tips to the waveguide facets. Input light from the O-band and C-band pump wavelengths, after filtering out the ASE background with a relatively broad bandpass filter (FWHM of 1.8 nm at 1310 nm and 1 nm at 1550 nm), was combined using a WDM fiber component. An identical WDM component was used to spectrally separate the output light at the chip output, which was then routed through cascaded filters to select one pair of spectral lines of Stokes and anti-Stokes photons positioned symmetrically around each pump wavelength. Limited by phase matching condition, the range of frequencies over which this occurs is limited to a few terahertz around each pump frequency because of the dispersion of the coupler and the waveguides. In each band, the same microring provided simultaneous resonance for all three frequencies across adjacent free-spectral ranges with a tight constraint on the narrow bandwidth dictated by the high-Q resonance.

We used commercially available, telecommunications grade fiber-coupled optical filters for these measurements. Two distinct sets of filters were used for the 1310 and 1550 nm bands; in the latter case, the

availability of reconfigurable optical add-drop multiplexers (ROADMs) made the experimental setup more versatile, as shown in Figure 5.6. ROADMs are not yet readily available at the 1310 nm wavelength band, and we simply used a 3-dB splitter to separate the "signal" and "idler" photons, incurring a penalty in the coincidence rate. In the 1310 nm wavelength band, the pump wavelength was positioned at 1316.5 nm and signal and idler photons were detected at 1309.8 nm and 1323.1 nm, respectively, with filter FWHM's of approximately 1.8 nm at both wavelengths. In the 1550 nm wavelength band, the pump wavelength was positioned at 1554.9 nm and signal and idler photons were detected at 1535.5 nm and 1574.7 nm, respectively, with filter FWHM's of approximately 0.6 nm and 0.8 nm, respectively. Next-to-nearest resonances are chosen here for pair generation in 1550 nm band due to the limited wavelength tuning ranges of the filters[a]. Note that the spectral FWHM of the microring resonance was approximately 0.03 nm, much narrower than any of the filter widths. Thus, these filters do not reshape the joint-spectral intensity, as may be a concern with broadband SFWM in waveguides.

Photons were detected using four fiber-coupled SNSPDs. Two detectors were optimized for wavelengths around 1310 nm with a detection efficiency of 90%, and the other two for 1550 nm with 65% detection efficiency. These detectors were not gated and operated in a simple DC-biased mode with an RF-amplified readout. Coincidences were measured using a multi-input TDC instrument, with 0.16 ns bin width used for all coincidence measurements.

5.2.2 Measurement

The silicon microring generated photon pairs at both wavelength bands separately, and also at both bands simultaneously when excited by both pumps. CW pumps were used for all these experiments. Before discussing the quality of the photon pairs, we first discuss the dynamics when the second optical pump is turned on and off, in the presence of the first pump. This is shown in Figure 5.7(b), which recorded the change in single counts of all four channels (1550 nm signal and idler, 1310 nm signal and idler) when the

[a] Tuning ranges are 1528-1562 nm for C-band filters (for signal photons) and 1567-1603 nm for L-band filters (for idler photons).

pumps were turned on and off individually. First, each pump was positioned (i.e., the numerical values of the laser wavelength and power settings were chosen) individually and separately. Next, to create the time-resolved graph shown in Figure 5.7(b), the second pump was simply turned on (at the pre-determined wavelength power settings, with no further adjustment) when the first pump was already active. Next, the first pump was turned off, and then it was turned back on again with no wavelength or power tuning. It mimics the operation of the device in a practical communication network setting, where fine-tuning of the resonance may not be practical. The p-i-n diode fabricated across the waveguide cross-section was used to monitor the resonance of the microring to the laser wavelength(s). Under these conditions, Figure 5.7(b) shows an anti-correlation between the photon pair fluxes generated by the two pumps, i.e., the photon generation rate at 1550 nm drops slightly when the 1310 nm pump is turned on, and the photon generation at 1310 nm rises further when the pump at 1550 nm is turned off etc. Finite numbers of counts were registered on the 1550 nm detectors from the 1310 nm pumps alone, but there was negligible signal-idler cross-correlation in this regime (and no entanglement), so these residual photons are just a noise background from the ASE of the 1310 nm pump laser leaking through the filters, and do not serve any purpose (or leak any information about the 1310 nm correlated-photon pair). The anti-correlation behavior seen in Figure 5.7(b) is more likely to be caused by a minor shifting of ring resonances induced by heating of micro-resonator when a second pump is added, alongside the residual (the p-i-n diode is operated with a reverse bias) FCA and nonlinear TPA, as explained in Section 2.1, rather than pump-pump mixing or depletion. The measured reverse-biased photocurrents across the p-i-n diode in the waveguide cross-section was, in the combined pump case (5.3 μA), approximately equal to the sum of the photocurrents in the individual pump cases (4.6 μA for the 1310 pump of -4 dBm alone and 0.7 μA for the 1550 pump of -6 dBm alone). Future measurements are being planned to investigate the time-constant of the change induced by turning one of the two pumps on and off, but it appears to be relatively slow. The magnitude and sign (i.e., positive or negative change) of the variations shown in the figure depend on the precise tunings of the wavelengths and their positioning on the red or blue side of the ‘cold-cavity’ resonance. Theoretically, the optimal positioning of multiple optical pumps in a semiconductor microring resonator which exhibits thermally-

and carrier-driven bistability is a complex problem to be addressed separately from this experimental paper, which shows that even without careful fine-tuning of the wavelengths and pump powers, the microring can generate entangled photons at both pump wavelengths. To characterize the photon pairs, we examined the conventional pair-wise metrics such as the CAR, which, for high values of CAR, is basically equal to the second-order cross-correlation at zero time difference between the signal and idler photons, and also the two-photon Franson interferometric visibility for energy–time entanglement [33]. Again, pump wavelengths are pre-determined without re-positioning in these measurements. Since there are two pumps, we examine not only the anticipated pairs (e.g., the signal and idler photons at the1550 nm band only, or the signal and idler photons at the 1310 nm band only), but also the cross-correlations across wavelength bands (e.g., selecting a signal photon from the 1310 nm band and the idler photon from the1550 nm band, and vice versa).

5.2.2.1 CAR

Figure 5.8 shows the second-order signal-idler cross-correlation function, $g^2_{SI}(\tau)$, between the signal (S) and idler (I) photons, measured across all the various pair-wise combinations of 'S' and 'I' channels, i.e., selecting an 'S' from either the 1550 nm band (subscript labeled 'a') or the 1310 nm band (labeled 'α'), and similarly for the 'I' photon (labeled 'b' and 'β', respectively). The measurements shown in Figure 5.8 were performed when both pumps are present, with CW power levels of −4 dBm at 1310 nm and −6 dBm at 1550 nm, measured in the optical fiber just before the chip.

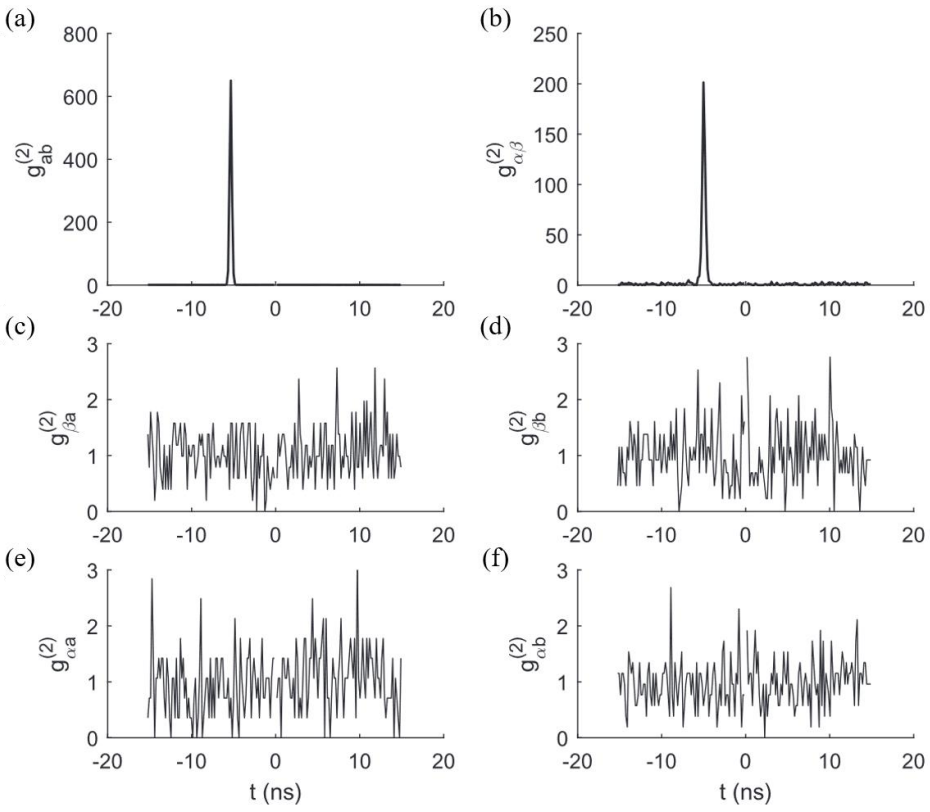

Figure 5.8 (a) Second-order cross-correlation function of 1550 nm signal (subscript "a") and idler (subscript "b") photons. (b) Second-order cross-correlation function of 1310 nm signal (subscript "α") and idler (subscript "β") photons. (c)–(f) Cross-correlations between 1550 and 1310 nm signal-idler photons across the two bands (note the subscripts).

The 'in-band' cross-correlation $g^2_{\mathrm{ab}}(\tau)$ between the 1550 nm signal and idler photons (Figure 5.8(a)), and the 'in-band' cross-correlation $g^2_{\alpha\beta}(\tau)$ between the 1310 nm signal and idler photons (Figure 5.8(b)) each exhibits a clean sharp peak. The value of this peak is approximately equal to 1 + CAR (see explanation in Section 1.1). The figures clearly indicate a strong correlation between signal and idler photons originated from the same pump. Figure 5.8(c) and (d) show no evidence of cross-correlation when the signal and idler photons are selected from among the pairs generated by different pumps, e.g., a signal photon from the 1550 nm SFWM process and an idler photon from the 1310 nm SFWM process. These are indeed the result we expect and desire, and they indicate that, in this device, each SFWM process operates independently and in parallel. Moreover, since the wavelengths of the pumps were not changed when the second pump was added to the first, these results also show that this silicon microring, as designed, was not

too strongly perturbed (e.g., detuned, or its Q-factor degraded) when the second SFWM process was added to the first.

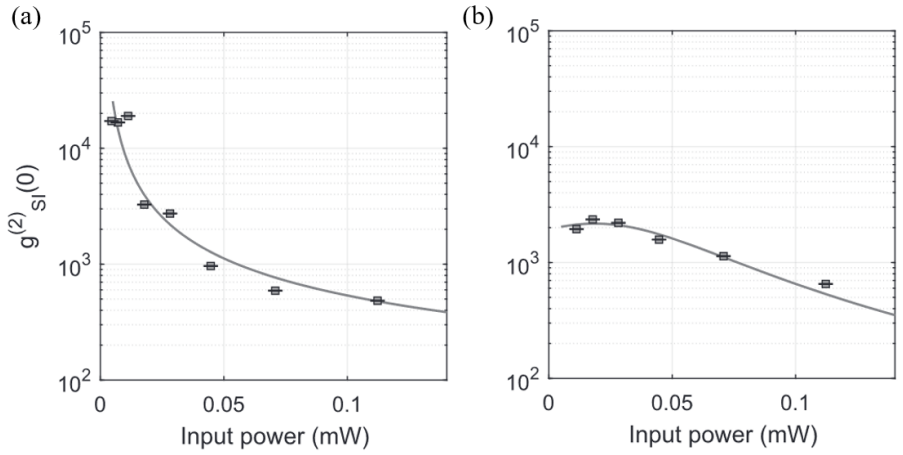

Figure 5.9 Second-order signal-idler cross-correlation at zero time difference (essentially equal to 1 + CAR) as a function of input pump power (at 1550 nm) in the feeder waveguide before the microring when (a) only1550 nm pump is present; (b) both 1550 and 1310 nm pumps are present.

To study this phenomenon in more depth, and explain why the microring works satisfactorily at both wavelength bands, $g^2_{\mathrm{SI}}(\tau)$ was measured for a signal-idler photon pair generated by the 1550 nm pump, at a sequence of pump power levels, and in the presence of a 1310 nm pump with CW power level -4 dBm in the fiber before the chip, also performing its own SFWM process. Each peak was fitted by a Gaussian function, whose FWHM was typically 0.31 ns (which is the expected value for the settings and detectors used in this experiment). The resulting $g^2_{\mathrm{SI}}(0)$ as a function of input pump power at the 1550 nm wavelength band is shown in Figure 5.9. When $g^2_{\mathrm{SI}}(0)$ continues to increase at low pump power regime, as shown by the data points in Figure 5.9(a), a fitted line was used with the functional form aP_0^{-b}, where a and b are constants. When $g^2_{\mathrm{SI}}(0)$ saturates, and then decreases (because of fewer measured true coincidences compared to accidentals) at small values of P_0, as shown by the data points in Figure 5.9(b), a fitted line was used with the functional form $(aP_0^2 + bP_0 + c)^{-1}$, similar to those used in [161,207]. In this case, true coincidences were overwhelmed by the residual pump ASE due to imperfect filter extinction ratio. However, in the earlier reports, the highest values of CAR were much less than 100, whereas the limit here is higher.

Acquisition time for each measurement ranges from a few seconds to a few minutes, depending on the input pump power level, since longer acquisition time is required to obtain a small uncertainty error bar. The uncertainties, too small to see in the figures, are mainly from accidentals (broken pairs from the losses incurred in coupling off the chip and subsequent filtering) and are calculated as one standard deviation in the values of $g^2(\tau)$ in bins away from the peak.

When only the 1550 nm pump was present, we measured a very high $g^2_{SI}(0)$ value, 19,001 ± 144, resulting in a CAR of 19,000 which is the highest CAR value yet reported for silicon photonics pair generation in any device, at any wavelength. As is usual, this occurs at the lower end of the range of pump powers used in the experiment, when the measured (i.e., including the coupling and filtering losses) singles rates were 2 and 1.7 kHz, and loss-scaled (on-chip) photon generation rates were 37 and 56 kHz. At the highest power value used here, with the 1550 nm pump set to CW power level −6 dBm in the fiber before the chip, $g^2_{SI}(0)$ was 484 ± 4, for which case the measured singles rates were 50 and 46 kHz, and the on-chip photon generation rates were 0.93 and 1.5 MHz for the signal and idler photons. In passing, we note that these values are similar to those (CAR of 532 at a PGR of 1.1 MHz) obtained in Chapter 3 focusing on the 1550 nm SFWM process only, in which we further showed a HBT measurement with conditional self-correlation, $g^2_{ss}(0) = 0.098$, i.e., strong anti-bunching of a heralded single-photon source.

The same measurements were performed when the 1310 nm pump (power −4 dBm before the chip) was also present, whose SFWM process resulted in measured singles rates of 48 and 54 kHz, corresponding to on-chip photon generation rates of 1.6 and 2.3 MHz. In this case, $g^2_{SI}(0)$ again increased at lower power levels (of the 1550 nm pump) but saturated at about 1,943 ± 15, while still obtaining a high value of 653 ± 5 at the maximum power value. Thus, the CAR values are similar at the higher power levels (and at megahertz-rates of generated photons), but we were able to reach a higher CAR value at the lower power levels (and few-kilohertz-rates of generated photons) when only the 1550 nm pump was used, rather than both pumps. This is most likely due to a small value of residual pump power from the ASE of the 1310 nm

pump leaking through the finite extinction ratio of the filters, and causing a small number of accidental counts which are more strongly felt when the number of true coincidences is low.

5.2.2.2 Energy–time Entanglement

The generated photon pairs from both pumps are expected to demonstrate energy–time entanglement which can be investigated through the Franson-type two-photon interference experiment. We used the unfolded Franson interferometer configuration as shown in Figure 5.6, in which an electronically-tunable DLI is placed in the pathway of each of the signal and idler photons of the generated pair (after filtering). The two DLIs used in these measurements were fiber-coupled, polarization-maintaining devices, each with an FSR of 2.5 GHz (at 1550 nm) and peak-to-valley extinction ratio approximately 25 dB. Although designed for the 1550 nm wavelength (i.e., the manufacturer-specified FSR and insertion loss is correct at 1550 nm), we verified that they can also be used at 1310 nm with low insertion loss, but a different FSR (which is irrelevant for these measurements). The phase difference in the DLI's was piezo-controlled, and was tuned by voltage from a programmable low-noise power supply. Unlike in other experiments [152,159], no active DLI stabilization was required. Such DLIs are costly, individually-assembled instruments and we have two DLIs available for experiments. Thus, when the Franson measurement was performed at 1550 nm (i.e., photon pairs generated in the 1550 nm band were routed through the DLIs), a CAR measurement was simultaneously performed at 1310 nm, and vice versa.

The visibility fringes were measured by step-scanning the voltage setting on one DLI and holding it constant on the other DLI. A start-stop histogram was recorded for each voltage setting. The fitting uncertainty (one standard deviation) is shown as the error bar in Figure 5.10(a) and (b) and is too small to be visible. Although the signal and idler photons are at different wavelengths, separated by about 40 nm, the differential group delay accumulated over a few meters of fiber is negligible, compared to the timing jitter of the detectors.

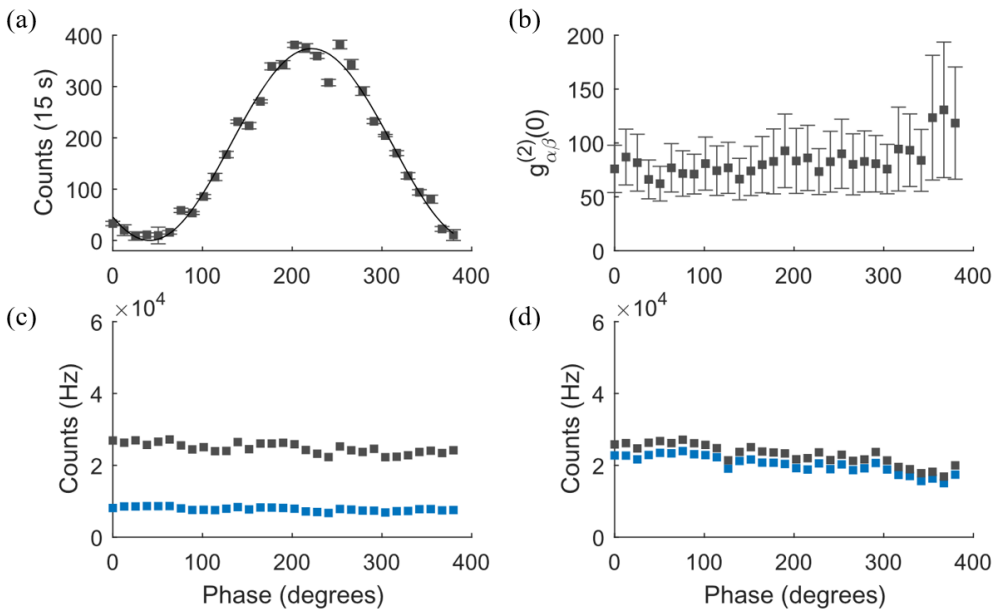

Figure 5.10 Time–energy entanglement measurement of 1550 nm photon pairs at presence of 1310 nm pump.(a) Franson visibility fringe of the "short–short" and "long–long" coincidence interference for photons pairs generated near 1550 nm. The horizontal axis corresponds to a phase setting of the delay-line interferometer, obtained by scaling the step-scanned experimental voltage setting by the voltage required to achieve a 2π phase shift. (b) Second-order cross-correlation function (essentially equal to 1 + CAR) for photon pairs generated near 1310 nm. (c) Measured singles count rates for signal and idler photons near 1550 nm. (d) Measured singles count rates for signal and idler photons near 1310 nm.

The ring was pumped at both 1550 nm and 1310 nm, with power of −6 dBm and −4 dBm before the chip respectively. Measurement results for 1550 nm photons are shown in Figure 5.10. The vertical axis corresponds to the measured number of coincidences in the indicated time interval, without scaling for the losses incurred in off-chip coupling, filtering and the finite detection efficiency. The observed fringe in Figure 5.10(a) shows a fitted visibility of $97.8 \pm 4\%$, which clearly surpasses the 71% threshold as proof of photon pair time-energy entanglement. The uncertainty in the visibility value derives from the goodness-of-fit of the sinusoid function, while those for each data point, too small to be visible here, stem from goodness-of-fit of the fitted parameters of the Gaussian function used to fit the central coincidence peak. Figure 5.10(b) shows the signal-idler cross-correlation at zero time, $g^2_{SI}(0)$, of 1310 nm photon pair as a function of phase tuning on the DLIs, whose lack of variation shows that the correlation in the 1310 nm photon pairs was maintained during the measurements.

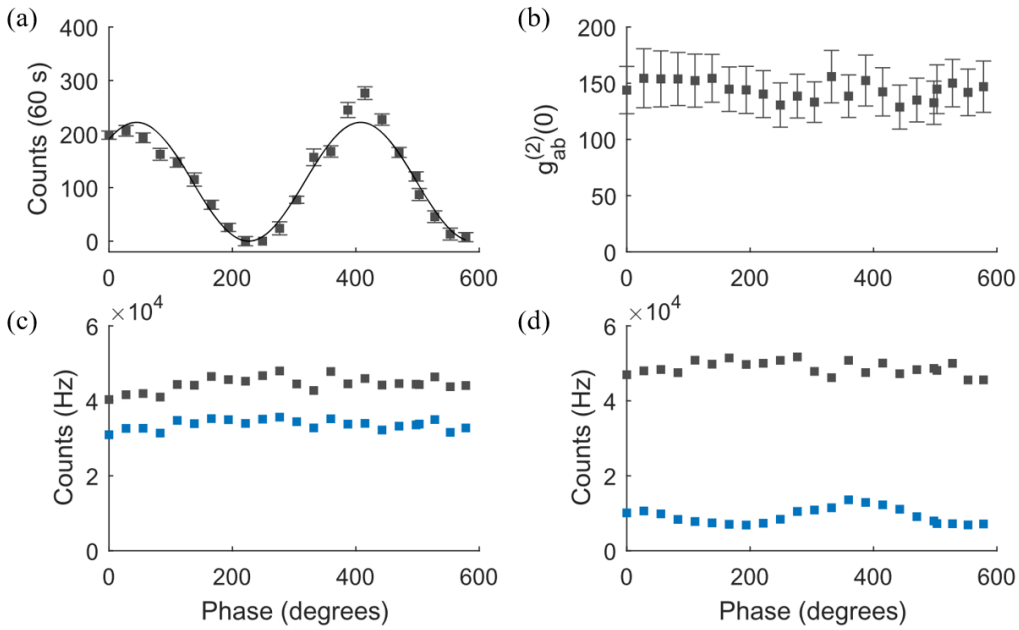

Figure 5.11 Time–energy entanglement measurement of 1310 nm photon pairs at presence of 1550 nm pump. (a) Franson visibility fringe of the "short–short" and "long–long" coincidence interference for photons pairs generated near 1310 nm. (b) Second-order cross-correlation function (essentially equal to 1 + CAR) for photon pairs generated near 1550 nm. (c) Measured singles count rates for signal and idler photons near 1310 nm. (d) Measured singles count rates for signal and idler photons near 1550 nm.

Similarly, the Franson visibility measurement results for 1310 nm photon pairs were shown in Figure 5.11. For the measurement in Figure 5.11(d), one of the fiber connections in the filter assembly broken and was manually spliced, incurring a 5 dB differential transmission loss (of one channel with the respect to the other), which does not affect the interpretation that $g^2(0)$ of the signal-idler photon pair generated at 1550 nm was invariant during the Franson measurement at 1310 nm. The observed fringe in Figure 5.11(a) shows a fitted visibility of 97.4 ± 13.3%, which also evidences time–energy entanglement of the 1310 nm photons. In both cases, the flat singles rates (versus phase), shown in Figure 5.10(c, d) and Figure 5.11(c, d), show the absence of single-photon interference, as desired [54,55]. The high visibilities measured here in the dual-pump case are similar quantitatively to the values we reported previously in Chapter 3 for the single-pump case. Taken together, Figure 5.10 and Figure 5.11 confirm that the energy–time entanglement properties of the pairs were maintained during the presence of the second pump.

5.2.3 Discussion

The measurement results reported here show the feasibility of using an appropriately-designed silicon microring to generate entangled photon pairs at the two optical fiber communication bands (1310 and 1550 nm) simultaneously. The signal-idler cross-correlation and time–energy entanglement of photon pairs generated by individual pumps were maintained during the presence of the second pump. These results lead the way to spectrally-multiplexed time–energy entanglement generation, which is a distinct step beyond multiplexed correlated-photon generation, and pair generation at distinct wavelength bands. Although the photons share the same physical medium (i.e., the silicon microring resonator), and there must be some correlations between the spectral bands (induced, for example, by TPA and its subsequent electronic carrier effects in the semiconductor), we see that they do not destroy entanglement, and there were no measurable cross-correlations between the SFWM process across the bands. These conclusions may be different if the properties of the microring were to be substantially changed. As shown in Chapter 2 , in micro-resonators with significantly higher Q values, the optical pump intensity of the recirculating field is higher. For lower Q values, the PGR may be too small, thus requiring stronger pump powers. In either case, the racetrack and/or directional coupler may be affected more strongly by thermal and free-carrier induced shifts, beyond the scope of mitigation of the reverse-biased diode, and lead to potential impairments, such as cross-pump correlations. In the process of performing these measurements, we also measured a CAR of 19,000 which is the highest CAR value yet reported for pair generation in silicon photonic microrings, at any wavelength.

Section 5.1 of Chapter 5 contains the material as it appears in the following of which the dissertation author was the primary investigator: Chaoxuan Ma, Xiaoxi Wang, and Shayan Mookherjea. "Photon-pair and heralded single photon generation initiated by a fraction of a 10 Gbps data stream." Optics express 26, no. 18 (2018): 22904-22915.

Section 5.2 of Chapter 5 contains the material as it appears in the following of which the dissertation author was the primary investigator: Chaoxuan Ma, and Shayan Mookherjea. "Simultaneous dual-band

entangled photon pair generation using a silicon photonic microring resonator." Quantum Science and Technology 3, no. 3 (2018): 034001.

Chapter 6
Spectrally Filtered Photonic Photon Pair Source

6.1 Introduction

Over the last decade, an integrated photonic approach is becoming increasingly attractive for QIP applications [26,208–211]. Some integrated photonic microchips which generate and use single photons or entangled photons have been demonstrated on SOI platform [210,211] for certain demanding QIP applications. However, progress towards inexpensive and robust integration of quantum optical sources in manufacturable platforms (e.g., wafer-scale foundry-fabricated silicon photonics) for widespread applications, such as quantum communications or key distribution, is still incomplete. There is a growing need for such devices, in order to scale up the development of quantum communication links and repeaters.

Different approaches to on-chip integration of photon sources offer possible solutions at various wavelength ranges. Among the most popular devices are QDs [72,212], devices that generate photons from color centers [68,213] and nonlinear waveguides [214–216]. Of these, the latter are most suitable at the wavelengths near 1550 nm which are compatible with low-loss fiber optics transmission. With a strong third-order nonlinearity, entangled photon pairs can be generated in silicon waveguides and micro-resonators via SFWM. For example, a high quality of photon pair generation has been demonstrated in several silicon photonic microring resonator devices, as reviewed in [25].

Here, progress is demonstrated towards the engineering development of a single-chip, inexpensive and low-cost solution for high-quality and bright generation of entangled photon pairs and heralded single photons at 1550 nm which can be widely used in optical communication systems and networks. The motivation for this research is the observation that if high-quality photon-pair sources are designed as a

standalone device, they either require hybrid integration of a dedicated laser [187] or coupling of laser light from external platforms [140,178,215,217,218] and their practical usefulness can be limited. Technical challenges and additional losses (e.g., from multiple chip-fiber coupling stages) limits the scalability, performance and quality of the generated photon pairs or heralded single photons. However, silicon photonics already has a rapidly-growing device library of integrated device components, and can be fabricated in large volumes using cost-effective wafer-scale processing, and thus possesses the potential to address the needs for a low-cost, yet high-performance photon-pair source microchip at telecommunications wavelengths.

The usual device architecture for photon-pair generation uses a dedicated laser to pump the SFWM process in a waveguide or resonator. The most significant advancement we are pursuing in this research is to eliminate the requirement for a dedicated pump laser, and instead, tap a fraction of the data-modulated light that is already carried in the fibers that constitute an optical network. For example, a fraction of a 10 Gbps NRZ-modulated data stream, with a run-length balanced stream of 1's and 0's in an NRZ or RZ modulated 10 Gbit/s optical communications channel has a large number of pulses whose peak power level ($\leqslant$ 1 mW) and temporal width (50 – 100 ps) can be quite suitable for the purposes of generating entangled photon pairs from certain silicon microring resonators. Such a concept could potentially readily implement quantum communications within the same fiber networks as used in classical communications, using the same lasers which are already present in data transceivers, and thus greatly cutting the cost of adding quantum side-channels to classical links.

However, as discussed here, there are certain tradeoffs incurred in making such a significant simplification. Communications-grade transceiver laser diodes are much noisier, with higher levels of ASE noise than the laboratory-grade, external-feedback lasers or mode-locked lasers used to report the state-of-the-art in photon-pair generation. Here, measurements are reported on an integrated chip that could eventually be used with communications-grade lasers, but are, for the purposes of detailed characterization (including imperfections), still measured using laboratory-grade external-cavity tunable low-noise lasers.

Based on the reported data, progress has been made in meeting some of the challenges, and although complete success has not yet been achieved, we have reason to be optimistic that the remaining challenges can be overcome.

6.2 Overview of the Device Architecture

SFWM relies on the generation of correlated photons at the signal and idler frequencies, spaced symmetrically around the pump frequency by one or more multiples of the resonator FSR [219,220]. Figure 6.1 shows the proposed scheme of using a fraction of a classical data link, rather than a dedicated laser, for pumping the SFWM process in a silicon microring resonator. Unlike a laboratory-grade low noise tunable laser (for example, see [221]), the ASE noise floor of a laser diode used in a typical optical data communications transceiver (e.g., SFP+ module) is so high that photon pairs generated by even the most efficient silicon photonic device pumped by such a laser will be buried far below the ASE floor at the same wavelengths [222,223]. For example, a hypothetical rate of 10 MHz of generated photons (taken, for the sake of illustration to be higher than has been achieved so far in most silicon devices [25,152,162]) would result in an average optical power level of only -80 dBm, which is more than 40 dB below the broad-band noise floor of a typical transceiver-grade laser at 1550 nm.

While the PGR of SFWM increases quadratically with pump power, silicon micro-resonators cannot be pumped with too much optical pump power, since they suffer from TPA and FCA [224–226]. One might, therefore, think that alternative materials are better suited for SFWM [227,228]. However, silicon fabrication is the most practical device technology, and silicon photonics has many other library components already developed which are useful in scaling up integrated circuits. Moreover, as long as a reasonably high quality of the quantum light is desirable, no other integrated photonics technology has gone much beyond about 10 MHz rates of photon pairs anyway. In this work, we focus on improving the silicon photonics approach.

There are four stages of this chip and a summary of the component specifications is listed in Table 6.1, comparing the design intention with the experimentally-measured result on the fabricated chip. A schematic outline of the four stages of the chip, and their purpose is shown in Figure 6.1. The microchip consists of a high-Q microring resonator for optically-pumped photon pair generation using SFWM, and several stages of tunable filters, also using microring resonators. The first filter bank carves stop bands in the broad ASE from the input pump light at the specific wavelengths that will be used for the generation of the signal and idler photon pairs. This means that there has to be a specific relationship between the FSR of the pair-generation microring and that of the ASE filter. The simplest such relationship is FSR(ring) = FSR(filter) / 2, which results in pairs of symmetrically-spaced spectral notches being carved at the signal and idler frequencies (or equivalently, wavelengths), and the pump frequency being allowed through with low insertion loss. Here, we focus on one set of signal-idler frequencies around the pump. The filter stopband width was designed to be about 1 nm, in order to match that of the conventional off-the-shelf telecommunications-grade filters (100 GHz, 0.8 nm) used in front of the single-photon detectors.

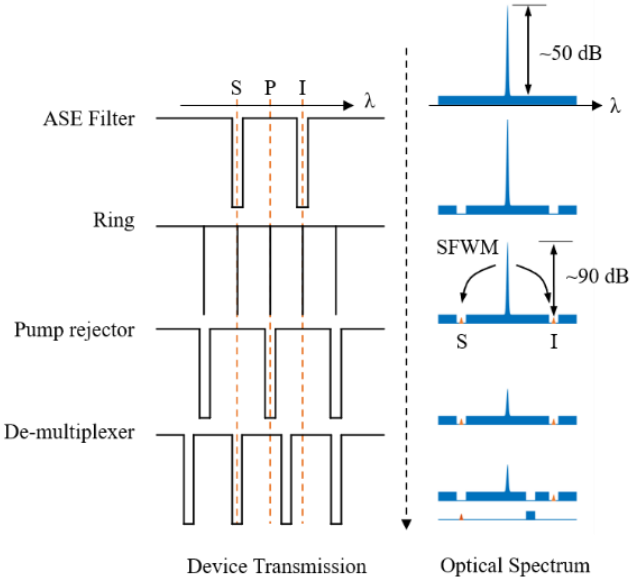

Figure 6.1 The photonic chip consists of a micro-resonator for photon pair generation and several stages of tunable optical filters: ASE filter, pump rejector and signal/idler demux. The ASE filter filters out the ASE from the pump laser. The resonator generates photon pairs through SFWM. The next filter suppresses the pump to avoid subsequent SFWM process in waveguides and the last one demuxes generated photon pairs to separate output waveguides.

The filter which follows the microring suppresses the residual pump light to such an extent that the rate of further SFWM (or spontaneous Raman scattering) in the photonic circuit is negligible. Thus, the photon pairs generated in the microring are not contaminated from added photon noise in the rest of the circuit before the output port. It is not possible yet to fully reject the pump light on a single microchip; the required extinction ratio for high-quality pair generation is typically greater than 120 dB, and only cascaded microchips have demonstrated such performance [111,137]. Our primary goal at the present time is to prevent additional SFWM or scattering processes from corrupting the quantum state after it is prepared by the microring, for which the rate of additive noise photons scales roughly quadratically with the pump power. Thus, an extinction of only 40-50 dB would essentially eliminate such otherwise dominant noise processes in a practical microchip architecture. With a minor modification (running the drop waveguide to an output port), the residual pump light can be utilized for other purposes e.g., classical data communication [229] or clock synchronization [230]. There is another stage of optical filters included in the chip design, which was intended to serve to demultiplex the signal and idler photons. As such, the design FSR was chosen such that 2 x FSR(de-mux) = 3 x FSR(ring). However, fabrication errors resulted in the FSR being similar to that of the other filters, and thus, this filter also served mainly to suppress the pump a bit further.

6.3 Device and Experimental Details

Table 6.1 Summary of Component Specifications

Chip section	FSR		FWHM		Extinction ratio	
	designed	measured	designed	measured	designed	measured
ASE rejection filter	10 nm	11 nm	1 nm	4 nm	>50 dB	19.4 dB
Microring resonator	5 nm	10 nm	0.006 nm	0.011 nm	5 dB	7 dB
Residual pump suppression filter	10 nm	11 nm	1 nm	4 nm	>50 dB	19.4 dB
De-multiplexing filter	7.5 nm	9.3 nm	1 nm	4.7 nm	>50 dB	25.6 dB

The microchip was fabricated by a foundry silicon photonic process on SOI wafers, which has a silicon layer of 230 nm on top of 2 μm-thick buried oxide. The light path from the input to the output of the chip traverses sixteen microring resonators, which serve various functions. Most important is the microring used for pair generation, which was designed as an all-pass resonator, using partially-etched ridge silicon waveguides of width 0.6 μm and slab thickness 70 nm, with a propagation loss (nominal) of 0.7 dB/cm. To comprise this ring resonator, four Bezier quarter-bends were used, each designed with a radius of R = 10 μm. Bezier bends achieve lower bending loss than a simple quarter-circle, leading to a higher Q factor and thus, a higher PGR.

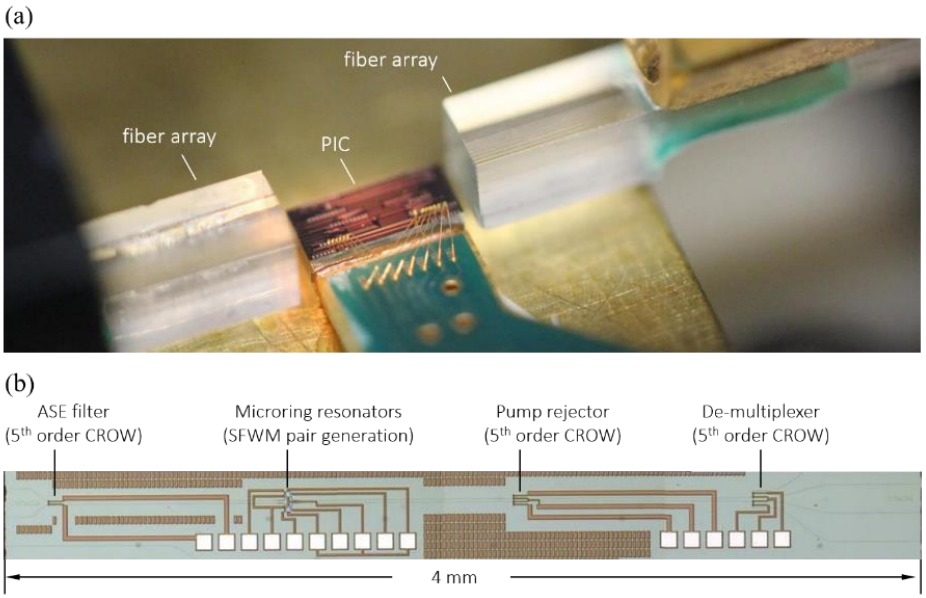

Figure 6.2 (a) Photograph of the wire-bonded chip and the fiber arrays used for edge coupling to tapered waveguides at the edge of the chips, before final alignment of the fiber arrays for measurements. (b) Optical microscope image of the chip, showing the various stages. The electrical wirebonds and wiring traces are also visible. (PIC: Photonic Integrated Circuit. CROW: Coupled Resonator Optical Waveguide optical filter configuration).

However, the optical circulating intensity is also higher, and may cause thermo-topic resonance shifts. Using p and n implants, followed by via formation and metalization (as part of the foundry process) a p-i-n diode was built in the cross-section of the waveguide used for the microring resonator. The dopants were placed far from the middle of the waveguide, in order to minimize the optical loss. When the optical

circulating power is high (i.e., the microring is driven by a pump laser whose wavelength is on resonance), there is a weak, but easily measured photocurrent (see measurements below) which is proportional to the optical power circulating in the microring [130]. The electrical readout of this diode (under a typical bias of -1 V) provides a simple and convenient indicator whether the microring resonance wavelength is aligned to the wavelength of the pump laser, and is particularly helpful when tuning the device or the laser to compensate for thermo-optic resonance shifts.

The optical filters each consist of five coupled-microring resonators using fully-etched strip waveguides. For these microrings as well, four Bezier quarter-bends were used in each "ring", rather than simple quarter bends. The (effective) radii of the ring resonators in each filter were tailored to suit their distinct functions. Since they require the same FSR (10 nm) as the microring used for pair generation, the ASE filter and the residual pump suppressor filters share the same design for their constituent microrings. However, since the Q factor is lower, and therefore, the thermo-optic resonance shift was less of a concern, compared to the pair generation microring, the monitoring diode is not needed. Therefore, the microrings which make up the filters were designed using simple, fully-etched waveguides, without the slab region and the dopants. The de-multiplexer was intended to have an FSR that is in between that of the microring and the other filters, but was experimentally observed to have an FSR comparable to that of the pump suppression filter, and practically had the same effect. Here too, fully-etched waveguides were used.

All filters and the microring used for SFWM have metal heaters above to shift their filter passbands or ring resonances, which are formed with minimum geometry serpentines. The heater efficiencies were measured to be about 0.05 nm/mW for the filters and about 0.08 nm/mW for the ring. The photonic chip was wire-bonded with a PCB board and attached to the center of a brass board together with a thermistor and a heat sink to keep the chip temperature controlled using an external TEC controller. Light was coupled into and out of the chip by on-chip inverse tapers and edge-coupled polarization-maintaining fiber arrays, as shown in Figure 6.2(a). The insertion loss of each fiber-to-waveguide coupler was estimated as ~7 dB averaged over the wavelengths of interest, based on separate measurements at test sites (essentially straight

waveguides with similar taper structures at the edges) on the same chip. Figure 6.2(b) shows a top-down optical microscope image of the chip with the various sections.

Under SFWM, energy-conservation between the pump and the generated Stokes and anti-Stokes photon pair dictates the frequency relationship, $2\omega_{\mathrm{p}} = \omega_{\mathrm{S}} + \omega_{\mathrm{aS}}$, so that all three frequencies (wavelengths) lie within the band used in communication networks near 1550 nm. The microring provided simultaneous resonance for all three frequencies across adjacent free-spectral ranges with a tight constraint on the narrow bandwidth dictated by the high-quality factor resonance. The pump wavelength was positioned at 1553.2 nm and signal and idler photons were detected at 1543.3 nm and 1563.3 nm, respectively.

External tunable filters (benchtop components) were used at these three wavelengths with FWHM's of approximately 1 nm, 0.6 nm and 0.8 nm, respectively. Photons were detected using fiber-coupled superconducting (WSi) SNSPD, cooled to 0.8 K in a closed-cycle Helium-4 cryostat equipped with a sorption stage. The detection efficiencies for the SNSPDs were about 68% as measured using separate calibration measurements. These detectors were not gated and were operated in a simple dc-biased mode with an RF-amplified readout. Coincidences were measured using a multi-input TDC instrument, with 10 ps bin width, in start-stop mode.

6.4 Results

The fabricated microring resonator which is used for photon-pair generation was measured to have a loaded quality factor of 1.4×10^5 at 1550 nm, with a spectral FWHM of 1.4 GHz, as shown in Figure 6.3 (black line). The spectrum was measured by first locating the resonance using a swept-wavelength scan at low power, and then heating the ASE filter and pump rejector to align their passbands with the ring resonance. Searching for the resonance of the high-Q ring was assisted by measuring and monitoring the photocurrent from the reverse-biased p-i-n diode, as shown in Figure 6.3 (red line). The measurement of an improved value of the microring quality factor (Q) suggests that the optical propagation loss in the waveguide was adequately low, compared to our previous work [25].

The next set of reported results is about the monitoring of the microring resonance using the reverse bias diode fabricated across the ridge waveguide. The current, which is proportional to the circulating optical intensity of the pump field, is induced by a photo-transition of an electron from the valence band to a mid-bandgap state, and transitioning to the conduction band assisted by the electric field (see details in [130]). Here, a reverse bias of -1 V resulted in a generated current of about 160 nA at resonance. For off-resonance, the current was significantly less, and we achieved an on-off contrast of more than 30 dB (without requiring a change of the amplifier gain or bias). Such a current is easily measurable by low-noise integrated or off chip electronics and is adequate for monitoring the resonance of the microring. The slight mismatch between the spectral dip and photocurrent peak could be due to imperfect scan synchornization between the instruments or a result of uncontrolled ambient temperature variation in the measurement setup. The value of this monitoring photodiode in a multi-stage photonic circuit, with several tunable stages, is significant. In our experiments, it provides a more useful and more convenient monitoring mechanism for the resonance than, for example, looking at the microring with an infrared camera [231,232].

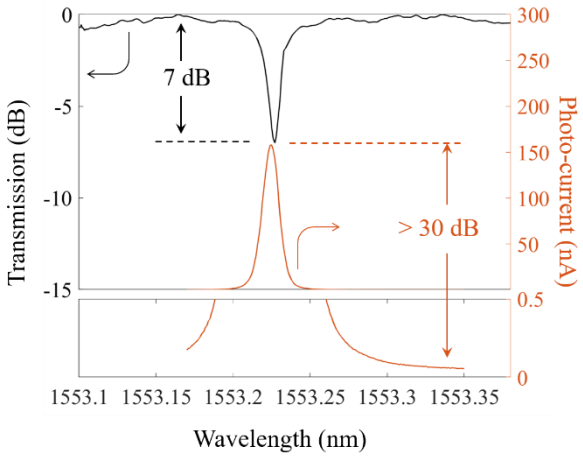

Figure 6.3 The black line (left-hand side vertical axis) shows the ring resonance (transmitted optical power in dB versus wavelenngth in nanometers) measured using a swept-wavelength tunable laser. The red line (right-hand side vertical axis) shows the resonance-monitoring photo-current, which was also measured when sweeping the laser wavelength. The lower panel shows more clearly the (low) noise floor of the photo-current on a separate vertical scale.

The complete chip, despite some fabrication imperfections in the current batch, was able to generate photon pairs when optically pumped with CW light near 1550 nm. Figure 6.4(a) shows the measured off-chip singles rates and coincidence rates as a function of the pump power coupled onto the chip (i.e., at the start of the feeder waveguide), with differences in the values a consequence of the different losses through the filters versus wavelength (3.6 dB and 7.2 dB at the signal and idler wavelengths). The on-chip PGR was calculated by PGR = S1× S2 /C, where S1 and S2 are signal and idler single rates (units: Hz) and C is the coincidence rate (units: Hz). The dependence of PGR on the input pump power is not quadratic, since the input pump power is relatively high and TPA cannot be ignored.

In Figure 6.4(b), the PGR at the ring and measured CAR is shown as a function of the on-chip pump power. From this data, the in-cavity spectral brightness of the ring at the highest pump level was calculated to be 6.5×10^{10} cps/mW^2/nm or 5.2×10^{8} cps/mW^2/GHz. The spectral brightness of this microring device is similar to our previous results [25] which is among the brightest silicon photon pair sources, and is also similar to that achieved using silicon microdisk resonators [112]. However, in the present chip, high filter losses significantly reduces the number of photon pairs that are coupled to fiber at the chip output; the measured coincidence rates are shown along the right-hand side vertical axis in Figure 6.4(a) and are about two orders of magnitude lower than in our previous work using stand-along microring resonators with a similar Q factor.

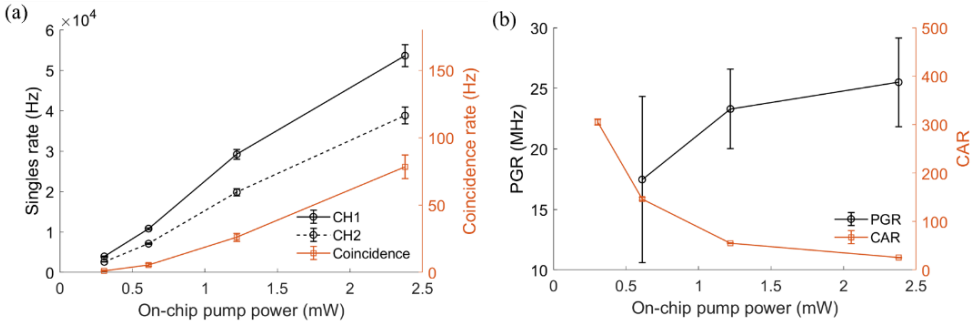

Figure 6.4 (a) Singles rates and coincidences rates. Error bars are one half standard deviation of the measurement. (b) Pair generation rates (PGRs) (off-chip) and CAR of the photon source. Error bars are one half standard deviation of the measurement. The compound standard deviation of PGRs is propagated from singles rates and coincidence rates, which are used to calculate PGR by PGR = S1× S2 /C. The CAR at the lowest and highest power levels are 305 and 25 respectively.

Measurements of CAR versus CW on-chip pump power are shown in Figure 6.4(b). The cross-correlation function of the arrival times of the two photons in a pair was measured for typical acquisition times of 200 to 1,000 seconds (longer acquisition times for lower singles rates). The counts were binned into histograms, one for each input pump power level. Each histogram peak was fitted by a Gaussian function, whose FWHM was about 25 ps, and the one standard deviation values of the fitting generated the error bars shown in the plots.

The highest CAR was 305 ± 6 measured using an integration time of 1,000 seconds. At the highest power values used here, CAR = 25 ± 0.46 with an integration time of 200 seconds, at a pair generation spectral brightness of 6.5×10^{10} cps/mW^2/nm or, equivalently, 5.2×10^{8} cps/mW^2/GHz using a different set of units also widely used. As expected, CAR decreased at higher pump powers, and when the PGR was higher, a shorter integration time was adequate in order to achieve smaller error bars.

6.5 Discussion

In this batch of fabricated microchips, the losses of the filters are well in excess of theory, and were estimated, from separate singulated-chip measurements to be greater than 10 dB for the ASE filter and pump rejector stages, and greater than 3 dB for the photon pair/pump demux stage. In Figure 6.5, we compared the same device (the residual pump suppression filter) on a die selected from a passive wafer (no dopants, no metals), and from a die selected from the active wafer. We observe greater degradation of extinction and higher overall transmission loss especially at longer wavelengths, and broadened passbands. This is most likely the result of increased optical loss from the optical waveguide mode interacting with the metal heaters which were positioned directly above the waveguides in our current design. Indeed, such optical loss would increase at the longer wavelengths, since the optical modes are slightly less confined, and this appears to be the case in the data shown in Figure 6.5. We believe that the higher-than-expected loss and degraded extinction of the filters may have been caused by an error in the deposited oxide thickness between the silicon and metal layers. A future version of the chip can move the metal heaters and feeder

electrical lines further away from the optical structures (although simulations using the nominal layer thicknesses did not suggest this would be necessary). Despite the present setbacks, the opto-electronic integrated chip which we measured was already able to obtain correlated photon pairs.

Looking ahead, it is likely that an off-chip laser diode as pump is the preferred embodiment of a pair source device based on spontaneous nonlinear optical process, since including the laser on the same chip as the pair generation device would inhibit future scalability with detectors, feed-forward logic, scaled-up multiplexing etc. which have a more pressing need for a short distance (time latency) to the source device. A typical transceiver-grade laser diode generates a lot of heat, which is not suitable from the perspective of integrating SPDs or single-photon processing circuitry on the same chip. Thus, the ability to incorporate filters together with the pair-generating microresonator brings us close to the practical limits of integration that is most urgently sought for the source component.

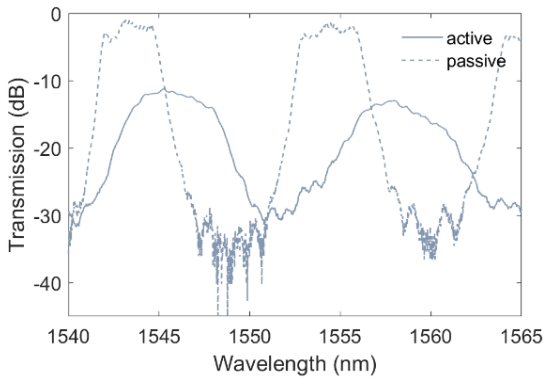

Figure 6.5 The drop port transmission of the ASE filter / pump rejector (they share the same design). A comparison between the same device on a passive and active wafer is presented here, which clearly shows the fast degradation of extinction, bandwidth and overall transmission loss after the deposition of metal above.

There may be another, potentially more important, reason to prefer the use of off-chip pump laser sources: A typical laser diode as used in very large numbers in optical transceivers is much less expensive than a laboratory-grade external cavity tunable laser, or a mode-locked laser, and can generate several milliwatts of power. Only a small fraction of this power is sufficient to generate megahertz rates of photon

pairs [229] if the device is a microring resonator, rather than a waveguide. In fact, this low level of pump power can be obtained as a tap fraction (i.e., a small fraction) of the power from the laser, or in some cases, from the optical power that is already in the fiber links of the network, e.g., a modulated data stream.

6.6 Conclusion

In summary, we have reported progress towards the ultimate goal of a fully-integrated microchip-scale quantum light source that could be used to generate high quality entangled photon pairs at telecommunication wavelengths with inexpensive pump lasers, such as those widely used in optical data communication networks. There has been considerable progress made in understanding and optimizing the photon pair generation process in silicon photonics, using both silicon waveguides and micro-resonators [25,140,152,162,219,220]; however, in most cases, laboratory-grade low-noise lasers have been used for the pump. Once fully realized, such microchips which integrate the pair generation stage with various optical filters which perform several different functions, may be useful for widespread practical usage, and in-network deployment of experiments recently performed in the laboratory using transceiver-pumped photon pair generation [229].

Chapter 6 , in full, has been submitted for publication of the material as it may appear in the following of which the dissertation author was the primary investigator: Chaoxuan Ma, Xiaoxi Wang, Shayan Mookherjea. “Progress towards a widely-usable integrated silicon photonic photon-pair source.”

Bibliography

1. F. Arute, K. Arya, R. Babbush, D. Bacon, J. C. Bardin, R. Barends, R. Biswas, S. Boixo, F. G. S. L. Brandao, D. A. Buell, B. Burkett, Y. Chen, Z. Chen, B. Chiaro, R. Collins, W. Courtney, A. Dunsworth, E. Farhi, B. Foxen, A. Fowler, C. Gidney, M. Giustina, R. Graff, K. Guerin, S. Habegger, M. P. Harrigan, M. J. Hartmann, A. Ho, M. Hoffmann, T. Huang, T. S. Humble, S. V. Isakov, E. Jeffrey, Z. Jiang, D. Kafri, K. Kechedzhi, J. Kelly, P. V. Klimov, S. Knysh, A. Korotkov, F. Kostritsa, D. Landhuis, M. Lindmark, E. Lucero, D. Lyakh, S. Mandrà, J. R. McClean, M. McEwen, A. Megrant, X. Mi, K. Michielsen, M. Mohseni, J. Mutus, O. Naaman, M. Neeley, C. Neill, M. Y. Niu, E. Ostby, A. Petukhov, J. C. Platt, C. Quintana, E. G. Rieffel, P. Roushan, N. C. Rubin, D. Sank, K. J. Satzinger, V. Smelyanskiy, K. J. Sung, M. D. Trevithick, A. Vainsencher, B. Villalonga, T. White, Z. J. Yao, P. Yeh, A. Zalcman, H. Neven, and J. M. Martinis, "Quantum supremacy using a programmable superconducting processor," Nature **574**, 505–510 (2019).
2. E. Pednault, J. Gunnels, D. Maslov, and J. Gambetta, "On “Quantum Supremacy,”" https://www.ibm.com/blogs/research/2019/10/on-quantum-supremacy/.
3. Q. Zhang, F. Xu, L. Li, N.-L. Liu, and J.-W. Pan, "Quantum information research in China," Quantum Sci. Technol. **4**, 040503 (2019).
4. L. Smith, "H.R.6227 - 115th Congress (2017-2018): National Quantum Initiative Act," https://www.congress.gov/bill/115th-congress/house-bill/6227/text.
5. "MEXT - Quantum Leap Flagship Program (MEXT Q-LEAP)," https://www.jst.go.jp/stpp/q-leap/en/index.html.
6. marqube, "Quantum Technologies Flagship," https://ec.europa.eu/digital-single-market/en/quantum-technologies.
7. "List of companies involved in quantum computing or communication," Wikipedia (2020).
8. B. P. Lanyon, P. Jurcevic, M. Zwerger, C. Hempel, E. A. Martinez, W. Dür, H. J. Briegel, R. Blatt, and C. F. Roos, "Measurement-Based Quantum Computation with Trapped Ions," Phys. Rev. Lett. **111**, 210501 (2013).
9. "Scaling the Ion Trap Quantum Processor | Science," https://science.sciencemag.org/content/339/6124/1164.
10. J. T. Barreiro, M. Müller, P. Schindler, D. Nigg, T. Monz, M. Chwalla, M. Hennrich, C. F. Roos, P. Zoller, and R. Blatt, "An open-system quantum simulator with trapped ions," Nature **470**, 486–491 (2011).
11. B. P. Lanyon, C. Hempel, D. Nigg, M. Müller, R. Gerritsma, F. Zähringer, P. Schindler, J. T. Barreiro, M. Rambach, G. Kirchmair, M. Hennrich, P. Zoller, R. Blatt, and C. F. Roos, "Universal Digital Quantum Simulation with Trapped Ions," Science **334**, 57–61 (2011).
12. I. Buluta, S. Ashhab, and F. Nori, "Natural and artificial atoms for quantum computation," Rep. Prog. Phys. **74**, 104401 (2011).
13. A. Reiserer, N. Kalb, G. Rempe, and S. Ritter, "A quantum gate between a flying optical photon and a single trapped atom," Nature **508**, 237–240 (2014).
14. M. Fuechsle, J. A. Miwa, S. Mahapatra, H. Ryu, S. Lee, O. Warschkow, L. C. L. Hollenberg, G. Klimeck, and M. Y. Simmons, "A single-atom transistor," Nat. Nanotechnol. **7**, 242–246 (2012).

15. T. Keating, K. Goyal, Y.-Y. Jau, G. W. Biedermann, A. J. Landahl, and I. H. Deutsch, "Adiabatic quantum computation with Rydberg-dressed atoms," Phys. Rev. A **87**, 052314 (2013).

16. D. Culcer, A. L. Saraiva, B. Koiller, X. Hu, and S. Das Sarma, "Valley-Based Noise-Resistant Quantum Computation Using Si Quantum Dots," Phys. Rev. Lett. **108**, 126804 (2012).

17. B.-C. Ren and F.-G. Deng, "Hyper-parallel photonic quantum computation with coupled quantum dots," Sci. Rep. **4**, 1–7 (2014).

18. M. Veldhorst, J. C. C. Hwang, C. H. Yang, A. W. Leenstra, B. de Ronde, J. P. Dehollain, J. T. Muhonen, F. E. Hudson, K. M. Itoh, A. Morello, and A. S. Dzurak, "An addressable quantum dot qubit with fault-tolerant control-fidelity," Nat. Nanotechnol. **9**, 981–985 (2014).

19. R. Barends, A. Shabani, L. Lamata, J. Kelly, A. Mezzacapo, U. L. Heras, R. Babbush, A. G. Fowler, B. Campbell, Y. Chen, Z. Chen, B. Chiaro, A. Dunsworth, E. Jeffrey, E. Lucero, A. Megrant, J. Y. Mutus, M. Neeley, C. Neill, P. J. J. O'Malley, C. Quintana, P. Roushan, D. Sank, A. Vainsencher, J. Wenner, T. C. White, E. Solano, H. Neven, and J. M. Martinis, "Digitized adiabatic quantum computing with a superconducting circuit," Nature **534**, 222–226 (2016).

20. J. M. Gambetta, J. M. Chow, and M. Steffen, "Building logical qubits in a superconducting quantum computing system," Npj Quantum Inf. **3**, 1–7 (2017).

21. J. R. Weber, W. F. Koehl, J. B. Varley, A. Janotti, B. B. Buckley, C. G. Van de Walle, and D. D. Awschalom, "Quantum computing with defects," Proc. Natl. Acad. Sci. **107**, 8513–8518 (2010).

22. A. Peruzzo, M. Lobino, J. C. F. Matthews, N. Matsuda, A. Politi, K. Poulios, X.-Q. Zhou, Y. Lahini, N. Ismail, K. Wörhoff, Y. Bromberg, Y. Silberberg, M. G. Thompson, and J. L. OBrien, "Quantum Walks of Correlated Photons," Science **329**, 1500–1503 (2010).

23. H. Zheng, D. J. Gauthier, and H. U. Baranger, "Waveguide-QED-Based Photonic Quantum Computation," Phys. Rev. Lett. **111**, 090502 (2013).

24. M. Gimeno-Segovia, P. Shadbolt, D. E. Browne, and T. Rudolph, "From Three-Photon Greenberger-Horne-Zeilinger States to Ballistic Universal Quantum Computation," Phys. Rev. Lett. **115**, 020502 (2015).

25. C. Ma, X. Wang, V. Anant, A. D. Beyer, M. D. Shaw, and S. Mookherjea, "Silicon photonic entangled photon-pair and heralded single photon generation with CAR > 12,000 and g^(2)(0) < 0006," Opt. Express **25**, 32995 (2017).

26. X. Qiang, X. Zhou, J. Wang, C. M. Wilkes, T. Loke, S. O'Gara, L. Kling, G. D. Marshall, R. Santagati, T. C. Ralph, J. B. Wang, J. L. O'Brien, M. G. Thompson, and J. C. F. Matthews, "Large-scale silicon quantum photonics implementing arbitrary two-qubit processing," Nat. Photonics **12**, 534–539 (2018).

27. J. Wang, D. Bonneau, M. Villa, J. W. Silverstone, R. Santagati, S. Miki, T. Yamashita, M. Fujiwara, M. Sasaki, H. Terai, M. G. Tanner, C. M. Natarajan, R. H. Hadfield, J. L. O'Brien, and M. G. Thompson, "Chip-to-chip quantum photonic interconnect by path-polarization interconversion," Optica **3**, 407–413 (2016).

28. K. Harada, H. Takesue, H. Fukuda, T. Tsuchizawa, T. Watanabe, K. Yamada, Y. Tokura, and S. Itabashi, "Generation of high-purity entangled photon pairs using silicon wire waveguide," Opt. Express **16**, 20368 (2008).

29. J. Zhao, C. Ma, M. Ruesing, and S. Mookherjea, "High-quality photon-pair and heralded single-photon generation using periodically-poled thin-film lithium niobate," in *Frontiers in Optics + Laser Science APS/DLS (2019), Paper FTu6A.3* (Optical Society of America, 2019), p. FTu6A.3.

30. J. Carolan, C. Harrold, C. Sparrow, E. Martín-López, N. J. Russell, J. W. Silverstone, P. J. Shadbolt, N. Matsuda, M. Oguma, M. Itoh, G. D. Marshall, M. G. Thompson, J. C. F. Matthews, T. Hashimoto, J. L. O'Brien, and A. Laing, "Universal linear optics," Science **349**, 711–716 (2015).

31. A. I. Lvovsky, B. C. Sanders, and W. Tittel, "Optical quantum memory," Nat. Photonics **3**, 706–714 (2009).

32. R. H. Brown and R. Q. Twiss, "A test of a new type of steller interferometer on Sirius," Nature **178**, 1046–1048 (1956).

33. A. Migdall, S. Polyakov, J. Fan, and J. Bienfang, *Single-Photon Generation and Detection: Physics and Applications* (Academic Press, 2013), Vol. 45.

34. D. Bouwmeester, J.-W. Pan, K. Mattle, M. Eibl, H. Weinfurter, and A. Zeilinger, "Experimental quantum teleportation," **390**, 5 (1997).

35. L.-K. Chen, H.-L. Yong, P. Xu, X.-C. Yao, T. Xiang, Z.-D. Li, C. Liu, H. Lu, N.-L. Liu, L. Li, T. Yang, C.-Z. Peng, B. Zhao, Y.-A. Chen, and J.-W. Pan, "Experimental nested purification for a linear optical quantum repeater," Nat. Photonics **11**, 695–699 (2017).

36. H. Semenenko, P. Sibson, A. Hart, M. G. Thompson, J. G. Rarity, and C. Erven, "Chip-based measurement-device-independent quantum key distribution," ArXiv190808745 Quant-Ph (2019).

37. P. J. Mosley, J. S. Lundeen, B. J. Smith, P. Wasylczyk, A. B. U'Ren, C. Silberhorn, and I. A. Walmsley, "Heralded Generation of Ultrafast Single Photons in Pure Quantum States," Phys. Rev. Lett. **100**, 133601 (2008).

38. J. Lee, M. S. Kim, and Č. Brukner, "Operationally Invariant Measure of the Distance between Quantum States by Complementary Measurements," Phys. Rev. Lett. **91**, 087902 (2003).

39. C. K. Hong, Z. Y. Ou, and L. Mandel, "Measurement of subpicosecond time intervals between two photons by interference," Phys. Rev. Lett. **59**, 2044–2046 (1987).

40. O. Gazzano, S. Michaelis de Vasconcellos, C. Arnold, A. Nowak, E. Galopin, I. Sagnes, L. Lanco, A. Lemaître, and P. Senellart, "Bright solid-state sources of indistinguishable single photons," Nat. Commun. **4**, 1425 (2013).

41. C. Santori, D. Fattal, and Y. Yamamoto, "Indistinguishable photons from a single-photon device," **419**, 4 (2002).

42. M. Halder, A. Beveratos, R. T. Thew, C. Jorel, H. Zbinden, and N. Gisin, "High coherence photon pair source for quantum communication," New J. Phys. **10**, 023027 (2008).

43. W. Tittel, J. Brendel, H. Zbinden, and N. Gisin, "Quantum Cryptography Using Entangled Photons in Energy-Time Bell States," Phys. Rev. Lett. **84**, 4737–4740 (2000).

44. K. Mattle, H. Weinfurter, P. G. Kwiat, and A. Zeilinger, "Dense Coding in Experimental Quantum Communication," Phys. Rev. Lett. **76**, 4656–4659 (1996).

45. Z. Zhang and Z. Man, "Multiparty quantum secret sharing of classical messages based on entanglement swapping," Phys. Rev. A **72**, 022303 (2005).

46. C. H. Bennett, G. Brassard, C. Crépeau, R. Jozsa, A. Peres, and W. K. Wootters, "Teleporting an unknown quantum state via dual classical and Einstein-Podolsky-Rosen channels," Phys. Rev. Lett. **70**, 1895–1899 (1993).

47. D. Llewellyn, Y. Ding, I. I. Faruque, S. Paesani, D. Bacco, R. Santagati, Y.-J. Qian, Y. Li, Y.-F. Xiao, M. Huber, M. Malik, G. F. Sinclair, X. Zhou, K. Rottwitt, J. L. O'Brien, J. G. Rarity, Q. Gong, L. K. Oxenlowe, J. Wang, and M. G. Thompson, "Chip-to-chip quantum teleportation and multi-photon entanglement in silicon," Nat. Phys. 1–6 (2019).

48. E. Saglamyurek, N. Sinclair, J. Jin, J. A. Slater, D. Oblak, F. Bussières, M. George, R. Ricken, W. Sohler, and W. Tittel, "Broadband waveguide quantum memory for entangled photons," Nature **469**, 512–515 (2011).

49. K. S. Choi, H. Deng, J. Laurat, and H. J. Kimble, "Mapping photonic entanglement into and out of a quantum memory," Nature **452**, 67–71 (2008).

50. S.-B. Zheng and G.-C. Guo, "Efficient Scheme for Two-Atom Entanglement and Quantum Information Processing in Cavity QED," Phys. Rev. Lett. **85**, 2392–2395 (2000).

51. A. Serafini, S. Mancini, and S. Bose, "Distributed Quantum Computation via Optical Fibers," Phys. Rev. Lett. **96**, 010503 (2006).

52. R. Raussendorf and H. J. Briegel, "A One-Way Quantum Computer," Phys. Rev. Lett. **86**, 5188–5191 (2001).

53. M. J. Bremner, C. M. Dawson, J. L. Dodd, A. Gilchrist, A. W. Harrow, D. Mortimer, M. A. Nielsen, and T. J. Osborne, "Practical Scheme for Quantum Computation with Any Two-Qubit Entangling Gate," Phys. Rev. Lett. **89**, 247902 (2002).

54. J. D. Franson, "Bell inequality for position and time," Phys. Rev. Lett. **62**, 2205–2208 (1989).

55. P. G. Kwiat, A. M. Steinberg, and R. Y. Chiao, "High-visibility interference in a Bell-inequality experiment for energy and time," Phys. Rev. A **47**, R2472–R2475 (1993).

56. P. Sibson, J. E. Kennard, S. Stanisic, C. Erven, J. L. O'Brien, and M. G. Thompson, "Integrated silicon photonics for high-speed quantum key distribution," Optica **4**, 172 (2017).

57. ID Quantique, "Quantum-safe security," https://www.idquantique.com/quantum-safe-security/overview/.

58. Toshiba, "Toshiba QKD system," https://www.toshiba.eu/eu/Cambridge-Research-Laboratory/Quantum-Information/Quantum-Key-Distribution/Toshiba-QKD-system/.

59. M. Hijlkema, B. Weber, H. P. Specht, S. C. Webster, A. Kuhn, and G. Rempe, "A single-photon server with just one atom," Nat. Phys. **3**, 253–255 (2007).

60. M. Mücke, J. Bochmann, C. Hahn, A. Neuzner, C. Nölleke, A. Reiserer, G. Rempe, and S. Ritter, "Generation of single photons from an atom-cavity system," Phys. Rev. A **87**, 063805 (2013).

61. J. McKeever, A. Boca, A. D. Boozer, R. Miller, J. R. Buck, A. Kuzmich, and H. J. Kimble, "Deterministic Generation of Single Photons from One Atom Trapped in a Cavity," Science **303**, 1992–1994 (2004).

62. D. B. Higginbottom, L. Slodička, G. Araneda, L. Lachman, R. Filip, M. Hennrich, and R. Blatt, "Pure single photons from a trapped atom source," New J. Phys. **18**, 093038 (2016).

63. H. G. Barros, A. Stute, T. E. Northup, C. Russo, P. O. Schmidt, and R. Blatt, "Deterministic single-photon source from a single ion," New J. Phys. **11**, 103004 (2009).

64. M. Keller, B. Lange, K. Hayasaka, W. Lange, and H. Walther, "Continuous generation of single photons with controlled waveform in an ion-trap cavity system," Nature **431**, 1075–1078 (2004).

65. P. Lombardi, M. Trapuzzano, M. Colautti, G. Margheri, I. P. Degiovanni, M. López, S. Kück, and C. Toninelli, "A Molecule-Based Single-Photon Source Applied in Quantum Radiometry," Adv. Quantum Technol. **n/a**, 1900083 (n.d.).

66. L. Zhang, Y.-J. Yu, L.-G. Chen, Y. Luo, B. Yang, F.-F. Kong, G. Chen, Y. Zhang, Q. Zhang, Y. Luo, J.-L. Yang, Z.-C. Dong, and J. G. Hou, "Electrically driven single-photon emission from an isolated single molecule," Nat. Commun. **8**, 580 (2017).

67. D. Riedel, I. Söllner, B. J. Shields, S. Starosielec, P. Appel, E. Neu, P. Maletinsky, and R. J. Warburton, "Deterministic Enhancement of Coherent Photon Generation from a Nitrogen-Vacancy Center in Ultrapure Diamond," Phys. Rev. X **7**, 031040 (2017).

68. T. Iwasaki, F. Ishibashi, Y. Miyamoto, Y. Doi, S. Kobayashi, T. Miyazaki, K. Tahara, K. D. Jahnke, L. J. Rogers, B. Naydenov, F. Jelezko, S. Yamasaki, S. Nagamachi, T. Inubushi, N. Mizuochi, and M. Hatano, "Germanium-Vacancy Single Color Centers in Diamond," Sci. Rep. **5**, 1–7 (2015).

69. B. Rodiek, M. Lopez, H. Hofer, G. Porrovecchio, M. Smid, X.-L. Chu, S. Gotzinger, V. Sandoghdar, S. Lindner, C. Becher, and S. Kuck, "Experimental realization of an absolute single-photon source based on a single nitrogen vacancy center in a nanodiamond," Optica **4**, 71 (2017).

70. C. Wang, C. Kurtsiefer, H. Weinfurter, and B. Burchard, "Single photon emission from SiV centres in diamond produced by ion implantation," J. Phys. B At. Mol. Opt. Phys. **39**, 37–41 (2006).

71. N. Somaschi, V. Giesz, L. D. Santis, J. C. Loredo, M. P. Almeida, G. Hornecker, S. L. Portalupi, T. Grange, C. Antón, J. Demory, C. Gómez, I. Sagnes, N. D. Lanzillotti-Kimura, A. Lemaítre, A. Auffeves, A. G. White, L. Lanco, and P. Senellart, "Near-optimal single-photon sources in the solid state," Nat. Photonics **10**, 340–345 (2016).

72. J. Claudon, J. Bleuse, N. S. Malik, M. Bazin, P. Jaffrennou, N. Gregersen, C. Sauvan, P. Lalanne, and J.-M. Gérard, "A highly efficient single-photon source based on a quantum dot in a photonic nanowire," Nat. Photonics **4**, 174–177 (2010).

73. M. J. Holmes, K. Choi, S. Kako, M. Arita, and Y. Arakawa, "Room-Temperature Triggered Single Photon Emission from a III-Nitride Site-Controlled Nanowire Quantum Dot," Nano Lett. **14**, 982–986 (2014).

74. L.-M. Duan, A. Kuzmich, and H. J. Kimble, "Cavity QED and quantum-information processing with ``hot'' trapped atoms," Phys. Rev. A **67**, 032305 (2003).

75. F. Ripka, H. Kübler, R. Löw, and T. Pfau, "A room-temperature single-photon source based on strongly interacting Rydberg atoms," Science **362**, 446–449 (2018).

76. Q. Wang, W. Chen, G. Xavier, M. Swillo, S. Sauge, M. Tengner, T. Zhang, Z. F. Han, G. C. Guo, and A. Karlsson, "Robust decoy-state quantum key distribution with heralded single photon source," in *2008 Conference on Lasers and Electro-Optics and 2008 Conference on Quantum Electronics and Laser Science* (2008), pp. 1–2.

77. T. Chanelière, D. N. Matsukevich, S. D. Jenkins, T. A. B. Kennedy, M. S. Chapman, and A. Kuzmich, "Quantum Telecommunication Based on Atomic Cascade Transitions," Phys. Rev. Lett. **96**, 093604 (2006).

78. A. Martin, A. Issautier, H. Herrmann, W. Sohler, D. B. Ostrowsky, O. Alibart, and S. Tanzilli, "Polarization entangled photon-pair source based on a type-II PPLN waveguide emitting at a telecom wavelength," New J. Phys. **12**, 103005 (2010).

79. X. Guo, C. Zou, C. Schuck, H. Jung, R. Cheng, and H. X. Tang, "Parametric down-conversion photon-pair source on a nanophotonic chip," Light Sci. Appl. **6**, e16249–e16249 (2017).

80. F. Kaneda, B. G. Christensen, J. J. Wong, H. S. Park, K. T. McCusker, and P. G. Kwiat, "Time-multiplexed heralded single-photon source," Optica **2**, 1010–1013 (2015).

81. P. G. Kwiat, E. Waks, A. G. White, I. Appelbaum, and P. H. Eberhard, "Ultrabright source of polarization-entangled photons," Phys. Rev. A **60**, R773–R776 (1999).

82. F. Samara, A. Martin, C. Autebert, M. Karpov, T. J. Kippenberg, H. Zbinden, and R. Thew, "High-rate photon pairs and sequential Time-Bin entanglement with Si_3N_4 microring resonators," Opt. Express **27**, 19309 (2019).

83. X. Lu, S. Rogers, T. Gerrits, W. C. Jiang, S. W. Nam, and Q. Lin, "Heralding single photons from a high-Q silicon microdisk," Optica **3**, 1331–1338 (2016).

84. B. Srivathsan, G. K. Gulati, B. Chng, G. Maslennikov, D. Matsukevich, and C. Kurtsiefer, "Narrow Band Source of Transform-Limited Photon Pairs via Four-Wave Mixing in a Cold Atomic Ensemble," Phys. Rev. Lett. **111**, 123602 (2013).

85. E. Moreau, I. Robert, L. Manin, V. Thierry-Mieg, J. M. Gérard, and I. Abram, "Quantum Cascade of Photons in Semiconductor Quantum Dots," Phys. Rev. Lett. **87**, 183601 (2001).

86. F. Troiani, J. I. Perea, and C. Tejedor, "Cavity-assisted generation of entangled photon pairs by a quantum-dot cascade decay," Phys. Rev. B **74**, 235310 (2006).

87. P. K. Pathak and S. Hughes, "Coherent generation of time-bin entangled photon pairs using the biexciton cascade and cavity-assisted piecewise adiabatic passage," Phys. Rev. B **83**, 245301 (2011).

88. R.-B. Jin, J. Zhang, R. Shimizu, N. Matsuda, Y. Mitsumori, H. Kosaka, and K. Edamatsu, "High-visibility nonclassical interference between intrinsically pure heralded single photons and photons from a weak coherent field," Phys. Rev. A **83**, 031805 (2011).

89. T. Yamamoto, M. Koashi, Ş. K. Özdemir, and N. Imoto, "Experimental extraction of an entangled photon pair from two identically decohered pairs," Nature **421**, 343–346 (2003).

90. C. Kurtsiefer, M. Oberparleiter, and H. Weinfurter, "High-efficiency entangled photon pair collection in type-II parametric fluorescence," Phys. Rev. A **64**, 023802 (2001).

91. G. Brida, I. P. Degiovanni, M. Genovese, F. Piacentini, P. Traina, A. Della Frera, A. Tosi, A. Bahgat Shehata, C. Scarcella, A. Gulinatti, M. Ghioni, S. V. Polyakov, A. Migdall, and A. Giudice, "An extremely low-noise heralded single-photon source: A breakthrough for quantum technologies," Appl. Phys. Lett. **101**, 221112 (2012).

92. T. Inagaki, N. Matsuda, O. Tadanaga, M. Asobe, and H. Takesue, "Entanglement distribution over 300 km of fiber," Opt. Express **21**, 23241–23249 (2013).

93. M. Houe and P. D. Townsend, "An introduction to methods of periodic poling for second-harmonic generation," J. Phys. Appl. Phys. **28**, 1747–1763 (1995).

94. M. Fiorentino, P. L. Voss, J. E. Sharping, and P. Kumar, "All-fiber photon-pair source for quantum communications," IEEE Photonics Technol. Lett. **14**, 983–985 (2002).

95. J. G. Rarity, J. Fulconis, J. Duligall, W. J. Wadsworth, and P. S. J. Russell, "Photonic crystal fiber source of correlated photon pairs," Opt. Express **13**, 534–544 (2005).

96. A. V. Velasco, P. Cheben, P. J. Bock, A. Delâge, J. H. Schmid, J. Lapointe, S. Janz, M. L. Calvo, D.-X. Xu, M. Florjańczyk, and M. Vachon, "High-resolution Fourier-transform spectrometer chip with microphotonic silicon spiral waveguides," Opt. Lett. **38**, 706–708 (2013).

97. P. Dong, W. Qian, S. Liao, H. Liang, C.-C. Kung, N.-N. Feng, R. Shafiiha, J. Fong, D. Feng, A. V. Krishnamoorthy, and M. Asghari, "Low loss shallow-ridge silicon waveguides," Opt. Express **18**, 14474–14479 (2010).

98. X. Wang, C. Ma, R. Kumar, P. Doussiere, R. Jones, H. Rong, and S. Mookherjea, "Photon Pair Generation Using Silicon Photonic Microring and Hybrid Laser," in *Conference on Lasers and Electro-Optics (2017), Paper JTh5C.6* (Optical Society of America, 2017), p. JTh5C.6.

99. C. Schuck, W. H. P. Pernice, and H. X. Tang, "NbTiN superconducting nanowire detectors for visible and telecom wavelengths single photon counting on Si3N4 photonic circuits," Appl. Phys. Lett. **102**, 051101 (2013).

100. L. Caspani, C. Xiong, B. J. Eggleton, D. Bajoni, M. Liscidini, M. Galli, R. Morandotti, and D. J. Moss, "Integrated sources of photon quantum states based on nonlinear optics," Light Sci. Appl. **6**, e17100–e17100 (2017).

101. C. M. Gentry, J. M. Shainline, M. T. Wade, M. J. Stevens, S. D. Dyer, X. Zeng, F. Pavanello, T. Gerrits, S. W. Nam, R. P. Mirin, and M. A. Popović, "Quantum-correlated photon pairs generated in a commercial 45 nm complementary metal-oxide semiconductor microelectronic chip," Optica **2**, 1065–1071 (2015).

102. L.-T. Feng, G.-C. Guo, and X.-F. Ren, "Progress on Integrated Quantum Photonic Sources with Silicon," Adv. Quantum Technol. **n/a**, 1900058 (n.d.).

103. A. Liu, H. Rong, R. Jones, O. Cohen, D. Hak, and M. Paniccia, "Optical Amplification and Lasing by Stimulated Raman Scattering in Silicon Waveguides," J. Light. Technol. **24**, 1440 (2006).

104. K. K. Tsia, S. Fathpour, and B. Jalali, "Energy harvesting in silicon wavelength converters," Opt. Express **14**, 12327–12333 (2006).

105. M. Dinu, F. Quochi, and H. Garcia, "Third-order nonlinearities in silicon at telecom wavelengths," Appl. Phys. Lett. **82**, 2954–2956 (2003).

106. R. L. Espinola, J. I. Dadap, R. M. Osgood, S. J. McNab, and Y. A. Vlasov, "C-band wavelength conversion in silicon photonic wire waveguides," Opt. Express **13**, 4341–4349 (2005).

107. K. Yamada, H. Fukuda, T. Tsuchizawa, T. Watanabe, T. Shoji, and S. Itabashi, "All-optical efficient wavelength conversion using silicon photonic wire waveguide," IEEE Photonics Technol. Lett. **18**, 1046–1048 (2006).

108. Q. Lin and G. P. Agrawal, "Silicon waveguides for creating quantum-correlated photon pairs," Opt. Lett. **31**, 3140–3142 (2006).

109. J. E. Sharping, K. F. Lee, M. A. Foster, A. C. Turner, B. S. Schmidt, M. Lipson, A. L. Gaeta, and P. Kumar, "Generation of correlated photons in nanoscale silicon waveguides," Opt. Express **14**, 12388–12393 (2006).

110. J. R. Ong, R. Kumar, and S. Mookherjea, "Ultra-High-Contrast and Tunable-Bandwidth Filter Using Cascaded High-Order Silicon Microring Filters," IEEE Photonics Technol. Lett. **25**, 1543–1546 (2013).

111. M. Piekarek, D. Bonneau, S. Miki, T. Yamashita, M. Fujiwara, M. Sasaki, H. Terai, M. G. Tanner, C. M. Natarajan, R. H. Hadfield, J. L. O'Brien, and M. G. Thompson, "High-extinction ratio integrated photonic filters for silicon quantum photonics," Opt. Lett. **42**, 815 (2017).

112. W. C. Jiang, X. Lu, J. Zhang, O. Painter, and Q. Lin, "Silicon-chip source of bright photon pairs," Opt. Express **23**, 20884–20904 (2015).

113. M. Savanier, R. Kumar, and S. Mookherjea, "Photon pair generation from compact silicon microring resonators using microwatt-level pump powers," Opt. Express **24**, 3313–3328 (2016).

114. Y. Guo, W. Zhang, N. Lv, Q. Zhou, Y. Huang, and J. Peng, "The impact of nonlinear losses in the silicon micro-ring cavities on CW pumping correlated photon pair generation," Opt. Express **22**, 2620–2631 (2014).

115. X. Shi, K. Guo, J. B. Christensen, M. A. U. Castaneda, X. Liu, H. Ou, and K. Rottwitt, "Multichannel Photon-Pair Generation with Strong and Uniform Spectral Correlation in a Silicon Microring Resonator," Phys. Rev. Appl. **12**, 034053 (2019).

116. R. R. Kumar, X. Wu, and H. K. Tsang, "Compact high-extinction tunable CROW filters for integrated quantum photonic circuits," Opt. Lett. **45**, 1289–1292 (2020).

117. C. Wu, Y. Liu, X. Gu, X. Yu, Y. Kong, Y. Wang, X. Qiang, J. Wu, Z. Zhu, X. Yang, and P. Xu, "Bright photon-pair source based on a silicon dual-Mach-Zehnder microring," Sci. China Phys. Mech. Astron. **63**, 220362 (2019).

118. J. A. Steidle, C. C. Tison, M. L. Fanto, M. L. Fanto, S. F. Preble, and P. M. Alsing, "Highly Directional Silicon Microring Photon Pair Source," in *Conference on Lasers and Electro-Optics (2019), Paper FTh1D.4* (Optical Society of America, 2019), p. FTh1D.4.

119. F. A. Sabattoli, H. E. Dirani, F. Garrisi, S. Sam, C. Petit-Etienne, J. M. Hartmann, E. Pargon, C. Monat, M. Liscidini, C. Sciancalepore, M. Galli, and D. Bajoni, "A Source of Heralded Single Photon Using High Quality Factor Silicon Ring Resonators," in *2019 21st International Conference on Transparent Optical Networks (ICTON)* (2019), pp. 1–4.

120. J. W. Silverstone, R. Santagati, D. Bonneau, M. J. Strain, M. Sorel, J. L. O'Brien, and M. G. Thompson, "Qubit entanglement between ring-resonator photon-pair sources on a silicon chip," Nat. Commun. **6**, 1–7 (2015).

121. V. R. Almeida, C. A. Barrios, R. R. Panepucci, and M. Lipson, "All-optical control of light on a silicon chip," Nature **431**, 1081–1084 (2004).

122. X. Sang, E.-K. Tien, and O. Boyraz, "Applications of two-photon absorption in silicon," J. Optoelectron. Adv. Mater. **11**, 15–25 (2008).

123. J. R. Ong, R. Kumar, R. Aguinaldo, and S. Mookherjea, "Efficient CW Four-Wave Mixing in Silicon-on-Insulator Micro-Rings With Active Carrier Removal," IEEE Photonics Technol. Lett. **25**, 1699–1702 (2013).

124. C. A. Husko, A. S. Clark, M. J. Collins, A. D. Rossi, S. Combrié, G. Lehoucq, I. Rey, T. F. Krauss, C. Xiong, and B. J. Eggleton, "Cross-absorption as a limit to heralded silicon photon pair sources," in *Nonlinear Optics and Its Applications VIII; and Quantum Optics III* (International Society for Optics and Photonics, 2014), Vol. 9136, p. 91361O.

125. R. Soref and B. Bennett, "Electrooptical effects in silicon," IEEE J. Quantum Electron. **23**, 123–129 (1987).

126. A. J. Sabbah and D. M. Riffe, "Femtosecond pump-probe reflectivity study of silicon carrier dynamics," Phys. Rev. B **66**, 165217 (2002).

127. Y. Liu and H. K. Tsang, "Time dependent density of free carriers generated by two photon absorption in silicon waveguides," Appl. Phys. Lett. **90**, 211105 (2007).

128. G. T. Reed, *Silicon Photonics: The State of the Art* (John Wiley & Sons, 2008).

129. X. Wang and S. Mookherjea, "Fast circuit modeling of heat transfer in photonic integrated circuits," in *2017 Conference on Lasers and Electro-Optics (CLEO)* (2017), pp. 1–2.

130. M. Savanier, R. Kumar, and S. Mookherjea, "Optimizing photon-pair generation electronically using a p-i-n diode incorporated in a silicon microring resonator," Appl. Phys. Lett. **107**, 131101 (2015).

131. K. Guo, L. Yang, X. Shi, X. Liu, Y. Cao, J. Zhang, X. Wang, J. Yang, H. Ou, and Y. Zhao, "Nonclassical Optical Bistability and Resonance-Locked Regime of Photon-Pair Sources Using Silicon Microring Resonator," Phys. Rev. Appl. **11**, 034007 (2019).

132. N. Eid, R. Boeck, H. Jayatilleka, L. Chrostowski, W. Shi, and N. A. F. Jaeger, "FSR-free silicon-on-insulator microring resonator based filter with bent contra-directional couplers," Opt. Express **24**, 29009–29021 (2016).

133. P. P. Absil, J. V. Hryniewicz, B. E. Little, F. G. Johnson, K. J. Ritter, and P.-T. Ho, "Vertically coupled microring resonators using polymer wafer bonding," IEEE Photonics Technol. Lett. **13**, 49–51 (2001).

134. D. V. Tishinin, P. D. Dapkus, A. E. Bond, I. Kim, C. K. Lin, and J. O'Brien, "Vertical resonant couplers with precise coupling efficiency control fabricated by wafer bonding," IEEE Photonics Technol. Lett. **11**, 1003–1005 (1999).

135. S. Clemmen, K. P. Huy, W. Bogaerts, R. G. Baets, P. Emplit, and S. Massar, "Continuous wave photon pair generation in silicon-on-insulator waveguides and ring resonators," Opt. Express **17**, 16558–16570 (2009).

136. S. Azzini, D. Grassani, M. Galli, L. C. Andreani, M. Sorel, M. J. Strain, L. G. Helt, J. E. Sipe, M. Liscidini, and D. Bajoni, "From classical four-wave mixing to parametric fluorescence in silicon microring resonators," Opt. Lett. **37**, 3807–3809 (2012).

137. N. C. Harris, D. Grassani, A. Simbula, M. Pant, M. Galli, T. Baehr-Jones, M. Hochberg, D. Englund, D. Bajoni, and C. Galland, "Integrated Source of Spectrally Filtered Correlated Photons for Large-Scale Quantum Photonic Systems," Phys. Rev. X **4**, 041047 (2014).

138. S. Khasminskaya, F. Pyatkov, K. Słowik, S. Ferrari, O. Kahl, V. Kovalyuk, P. Rath, A. Vetter, F. Hennrich, M. M. Kappes, G. Gol'tsman, A. Korneev, C. Rockstuhl, R. Krupke, and W. H. P. Pernice, "Fully integrated quantum photonic circuit with an electrically driven light source," Nat. Photonics **10**, 727–732 (2016).

139. G. E. Digeronimo, M. Petruzzella, S. Birindelli, R. Gaudio, S. Fattah Poor, F. W. M. Van Otten, and A. Fiore, "Integration of Single-Photon Sources and Detectors on GaAs," Photonics **3**, 55 (2016).

140. N. Matsuda, P. Karkus, H. Nishi, T. Tsuchizawa, W. J. Munro, H. Takesue, and K. Yamada, "On-chip generation and demultiplexing of quantum correlated photons using a silicon-silica monolithic photonic integration platform," Opt. Express **22**, 22831 (2014).

141. J.-M. Lee, W.-J. Lee, M.-S. Kim, and J. J. Ju, "Noise Filtering for Highly Correlated Photon Pairs From Silicon Waveguides," J. Light. Technol. **37**, 5428–5434 (2019).

142. C. M. Gentry, O. S. Magaña-Loaiza, M. T. Wade, F. Pavanello, T. Gerrits, S. Lin, J. M. Shainline, S. D. Dyer, S. W. Nam, R. P. Mirin, M. A. Popović, and M. A. Popović, "Monolithic Source of Entangled Photons with Integrated Pump Rejection," in *Conference on Lasers and Electro-Optics (2018), Paper JTh4C.3* (Optical Society of America, 2018), p. JTh4C.3.

143. R. R. Kumar, X. Wu, and H. Tsang, "Compact High-Extinction Tunable CROW filters for Integrated Quantum Photonic Circuits," Opt. Lett. (2020).

144. M. W. Geis, S. J. Spector, M. E. Grein, R. T. Schulein, J. U. Yoon, D. M. Lennon, S. Deneault, F. Gan, F. X. Kaertner, and T. M. Lyszczarz, "CMOS-Compatible All-Si High-Speed Waveguide Photodiodes With High Responsivity in Near-Infrared Communication Band," IEEE Photonics Technol. Lett. **19**, 152–154 (2007).

145. H. Chen, X. Luo, and A. W. Poon, "Cavity-enhanced photocurrent generation by 1.55 μm wavelengths linear absorption in a p-i-n diode embedded silicon microring resonator," Appl. Phys. Lett. **95**, 171111 (2009).

146. I. W. Hsieh, H. Rong, and M. Paniccia, "Two-photon-absorption-based optical power monitor in silicon rib waveguides," in *7th IEEE International Conference on Group IV Photonics* (2010), pp. 326–328.

147. H. Chen and A. W. Poon, "Two-photon absorption photocurrent in p-i-n diode embedded silicon microdisk resonators," Appl. Phys. Lett. **96**, 191106 (2010).

148. E. Engin, D. Bonneau, C. M. Natarajan, A. S. Clark, M. G. Tanner, R. H. Hadfield, S. N. Dorenbos, V. Zwiller, K. Ohira, N. Suzuki, H. Yoshida, N. Iizuka, M. Ezaki, J. L. O'Brien, and M. G. Thompson, "Photon pair generation in a silicon micro-ring resonator with reverse bias enhancement," Opt. Express **21**, 27826–27834 (2013).

149. G. Harder, V. Ansari, B. Brecht, T. Dirmeier, C. Marquardt, and C. Silberhorn, "An optimized photon pair source for quantum circuits," Opt. Express **21**, 13975–13985 (2013).

150. M. Bock, A. Lenhard, C. Chunnilall, and C. Becher, "Highly efficient heralded single-photon source for telecom wavelengths based on a PPLN waveguide," Opt. Express **24**, 23992–24001 (2016).

151. H. Jin, F. M. Liu, P. Xu, J. L. Xia, M. L. Zhong, Y. Yuan, J. W. Zhou, Y. X. Gong, W. Wang, and S. N. Zhu, "On-Chip Generation and Manipulation of Entangled Photons Based on Reconfigurable Lithium-Niobate Waveguide Circuits," Phys. Rev. Lett. **113**, 103601 (2014).

152. F. Mazeas, M. Traetta, M. Bentivegna, F. Kaiser, D. Aktas, W. Zhang, C. A. Ramos, L. A. Ngah, T. Lunghi, É. Picholle, N. Belabas-Plougonven, X. L. Roux, É. Cassan, D. Marris-Morini, L. Vivien, G. Sauder, L. Labonté, and S. Tanzilli, "High-quality photonic entanglement for wavelength-multiplexed quantum communication based on a silicon chip," Opt. Express **24**, 28731–28738 (2016).

153. J. A. Steidle, M. L. Fanto, C. C. Tison, Z. Wang, S. F. Preble, and P. M. Alsing, "High spectral purity silicon ring resonator photon-pair source," Quantum Inf. Comput. XIII **9500**, 950015 (2015).

154. M. Bashkansky, I. Vurgaftman, A. C. R. Pipino, and J. Reintjes, "Significance of heralding in spontaneous parametric down-conversion," Phys. Rev. A **90**, 053825 (2014).

155. J. B. Spring, P. S. Salter, B. J. Metcalf, P. C. Humphreys, M. Moore, N. Thomas-Peter, M. Barbieri, X.-M. Jin, N. K. Langford, W. S. Kolthammer, M. J. Booth, and I. A. Walmsley, "On-chip low loss heralded source of pure single photons," Opt. Express **21**, 13522–13532 (2013).

156. D. Grassani, S. Azzini, M. Liscidini, M. Galli, M. J. Strain, M. Sorel, J. E. Sipe, and D. Bajoni, "Micrometer-scale integrated silicon source of time-energy entangled photons," Optica **2**, 88–94 (2015).

157. R. Wakabayashi, M. Fujiwara, K. Yoshino, Y. Nambu, M. Sasaki, and T. Aoki, "Time-bin entangled photon pair generation from Si micro-ring resonator," Opt. Express **23**, 1103 (2015).

158. J. Suo, S. Dong, W. Zhang, Y. Huang, and J. Peng, "Generation of hyper-entanglement on polarization and energy-time based on a silicon micro-ring cavity," Opt. Express **23**, 3985–3995 (2015).

159. R. Kumar, M. Savanier, J. R. Ong, and S. Mookherjea, "Entanglement measurement of a coupled silicon microring photon pair source," Opt. Express **23**, 19318–19327 (2015).

160. R. T. Thew, S. Tanzilli, W. Tittel, H. Zbinden, and N. Gisin, "Experimental investigation of the robustness of partially entangled qubits over 11 km," Phys. Rev. A **66**, 062304 (2002).

161. M. Davanço, J. R. Ong, A. B. Shehata, A. Tosi, I. Agha, S. Assefa, F. Xia, W. M. J. Green, S. Mookherjea, and K. Srinivasan, "Telecommunications-band heralded single photons from a silicon nanophotonic chip," Appl. Phys. Lett. **100**, 261104 (2012).

162. M. Fujiwara, R. Wakabayashi, M. Sasaki, and M. Takeoka, "Wavelength division multiplexed and double-port pumped time-bin entangled photon pair generation using Si ring resonator," Opt. Express **25**, 3445–3453 (2017).

163. S. F. Preble, M. L. Fanto, J. A. Steidle, C. C. Tison, G. A. Howland, Z. Wang, and P. M. Alsing, "On-Chip Quantum Interference from a Single Silicon Ring-Resonator Source," Phys. Rev. Appl. **4**, 021001 (2015).

164. J. W. Silverstone, J. Wang, D. Bonneau, P. Sibson, R. Santagati, C. Erven, J. L. O'Brien, and M. G. Thompson, "Silicon quantum photonics," in *2016 International Conference on Optical MEMS and Nanophotonics (OMN)* (2016), pp. 1–2.

165. T. Rudolph, "Why I am optimistic about the silicon-photonic route to quantum computing," APL Photonics **2**, 030901 (2017).

166. T. Suhara, "Generation of quantum-entangled twin photons by waveguide nonlinear-optic devices," Laser Photonics Rev. **3**, 370–393 (2009).

167. O. Alibart, V. D'Auria, M. D. Micheli, F. Doutre, F. Kaiser, L. Labonté, T. Lunghi, É. Picholle, and S. Tanzilli, "Quantum photonics at telecom wavelengths based on lithium niobate waveguides," J. Opt. **18**, 104001 (2016).

168. M. Smit, X. Leijtens, H. Ambrosius, E. Bente, J. van der Tol, B. Smalbrugge, T. de Vries, E.-J. Geluk, J. Bolk, R. van Veldhoven, L. Augustin, P. Thijs, D. D'Agostino, H. Rabbani, K. Lawniczuk, S. Stopinski, S. Tahvili, A. Corradi, E. Kleijn, D. Dzibrou, M. Felicetti, E. Bitincka, V. Moskalenko, J. Zhao, R. Santos, G. Gilardi, W. Yao, K. Williams, P. Stabile, P. Kuindersma, J. Pello, S. Bhat, Y. Jiao, D. Heiss, G. Roelkens, M. Wale, P. Firth, F. Soares, N. Grote, M. Schell, H. Debregeas, M. Achouche, J.-L. Gentner, A. Bakker, T. Korthorst, D. Gallagher, A. Dabbs, A. Melloni, F. Morichetti, D. Melati, A. Wonfor, R. Penty, R. Broeke, B. Musk, and D. Robbins, "An introduction to InP-based generic integration technology," Semicond. Sci. Technol. **29**, 083001 (2014).

169. F. Boitier, A. Orieux, C. Autebert, A. Lemaître, E. Galopin, C. Manquest, C. Sirtori, I. Favero, G. Leo, and S. Ducci, "Electrically Injected Photon-Pair Source at Room Temperature," Phys. Rev. Lett. **112**, 183901 (2014).

170. A. S. Clark, C. Husko, M. J. Collins, G. Lehoucq, S. Xavier, A. D. Rossi, S. Combrié, C. Xiong, and B. J. Eggleton, "Heralded single-photon source in a III-V photonic crystal," Opt. Lett. **38**, 649–651 (2013).

171. P. Sibson, C. Erven, M. Godfrey, S. Miki, T. Yamashita, M. Fujiwara, M. Sasaki, H. Terai, M. G. Tanner, C. M. Natarajan, R. H. Hadfield, J. L. O'Brien, and M. G. Thompson, "Chip-based quantum key distribution," Nat. Commun. **8**, 1–6 (2017).

172. R. Jones, M. N. Sysak, H. Park, A. W. Fang, H.-H. Chang, Y. H. Kuo, J. E. Bowers, O. Raday, and O. Cohen, "Integrated Hybrid Lasers and Amplifiers on a Silicon Platform," in *Optical Fiber Communication Conference/National Fiber Optic Engineers Conference (2008), Paper OWM1* (Optical Society of America, 2008), p. OWM1.

173. A. Alduino, L. Liao, R. Jones, M. Morse, B. Kim, W.-Z. Lo, J. Basak, B. Koch, H.-F. Liu, H. Rong, M. Sysak, C. Krause, R. Saba, R. Saba, D. Lazar, D. Lazar, L. Horwitz, L. Horwitz, R. Bar, R. Bar, S. Litski, S. Litski, A. Liu, K. Sullivan, O. Dosunmu, N. Na, T. Yin, F. Haubensack, I. -wei Hsieh, J. Heck, R. Beatty, H. Park, J. Bovington, S. Lee, H. Nguyen, H. Au, K. Nguyen, P. Merani, M. Hakami, and M. Paniccia, "Demonstration of a High Speed 4-Channel Integrated Silicon Photonics WDM Link with Hybrid Silicon Lasers," in *Integrated Photonics Research, Silicon and Nanophotonics and Photonics in Switching (2010), Paper PDIWI5* (Optical Society of America, 2010), p. PDIWI5.

174. D. Liang and J. E. Bowers, "Hybrid silicon lasers," in *Semiconductor Lasers: Fundamentals and Applications* (Woodhead Publishing, 2013), pp. 394–437.

175. M. Savanier and S. Mookherjea, "Generating photon pairs from a silicon microring resonator using an electronic step recovery diode for pump pulse generation," Appl. Phys. Lett. **108**, 251102 (2016).

176. D. Höckel, L. Koch, and O. Benson, "Direct measurement of heralded single-photon statistics from a parametric down-conversion source," Phys. Rev. A **83**, 013802 (2011).

177. S. Bettelli, "Comment on ``Coherence measures for heralded single-photon sources’’," Phys. Rev. A **81**, 037801 (2010).

178. M. J. Collins, C. Xiong, I. H. Rey, T. D. Vo, J. He, S. Shahnia, C. Reardon, T. F. Krauss, M. J. Steel, A. S. Clark, and B. J. Eggleton, "Integrated spatial multiplexing of heralded single-photon sources," Nat. Commun. **4**, 2582 (2013).

179. C. Xiong, T. D. Vo, M. J. Collins, J. Li, T. F. Krauss, M. J. Steel, A. S. Clark, and B. J. Eggleton, "Bidirectional multiplexing of heralded single photons from a silicon chip," Opt. Lett. **38**, 5176–5179 (2013).

180. C. Xiong, X. Zhang, Z. Liu, M. J. Collins, A. Mahendra, L. G. Helt, M. J. Steel, D.-Y. Choi, C. J. Chae, P. H. W. Leong, and B. J. Eggleton, "Active temporal multiplexing of indistinguishable heralded single photons," Nat. Commun. **7**, 1–6 (2016).

181. G. J. Mendoza, R. Santagati, J. Munns, E. Hemsley, M. Piekarek, E. Martín-López, G. D. Marshall, D. Bonneau, M. G. Thompson, and J. L. O’Brien, "Active temporal and spatial multiplexing of photons," Optica **3**, 127–132 (2016).

182. M. Pant, H. Krovi, D. Englund, and S. Guha, "Rate-distance tradeoff and resource costs for all-optical quantum repeaters," Phys. Rev. A **95**, 012304 (2017).

183. C. Ma, W. D. Sacher, Z. Tang, J. C. Mikkelsen, Y. Yang, F. Xu, T. Thiessen, H.-K. Lo, and J. K. S. Poon, "Silicon photonic transmitter for polarization-encoded quantum key distribution," Optica **3**, 1274–1278 (2016).

184. H. Cai, C. M. Long, C. T. DeRose, N. Boynton, J. Urayama, R. Camacho, A. Pomerene, A. L. Starbuck, D. C. Trotter, P. S. Davids, and A. L. Lentine, "Silicon photonic transceiver circuit for high-speed polarization-based discrete variable quantum key distribution," Opt. Express **25**, 12282–12294 (2017).

185. Y. Ding, D. Bacco, K. Dalgaard, X. Cai, X. Zhou, K. Rottwitt, and L. K. Oxenløwe, "High-dimensional quantum key distribution based on multicore fiber using silicon photonic integrated circuits," Npj Quantum Inf. **3**, 1–7 (2017).

186. D. Bunandar, A. Lentine, C. Lee, H. Cai, C. M. Long, N. Boynton, N. Martinez, C. DeRose, C. Chen, M. Grein, D. Trotter, A. Starbuck, A. Pomerene, S. Hamilton, F. N. C. Wong, R. Camacho, P. Davids, J. Urayama, and D. Englund, "Metropolitan Quantum Key Distribution with Silicon Photonics," Phys. Rev. X **8**, 021009 (2018).

187. X. Wang, C. Ma, R. Kumar, P. Doussiere, R. Jones, H. Rong, and S. Mookherjea, "Photon pair generation using a silicon photonic hybrid laser," APL Photonics **3**, 106104 (2018).

188. P. D. Dobbelaere, A. Ayazi, Y. Chi, A. Dahl, S. Denton, S. Gloeckner, K.-Y. Hon, S. Hovey, Y. Liang, M. Mack, G. Masini, A. Mekis, M. Peterson, T. Pinguet, J. Schramm, M. Sharp, C. Sohn, K. Stechschulte, P. Sun, G. Vastola, L. Verslegers, and R. Zhou, "Packaging of Silicon Photonics Systems," in *Optical Fiber Communication Conference (2014), Paper W3I.2* (Optical Society of America, 2014), p. W3I.2.

189. C. Ma and S. Mookherjea, "Simultaneous dual-band entangled photon pair generation using a silicon photonic microring resonator," Quantum Sci. Technol. **3**, 034001 (2018).

190. A. Christ, K. Laiho, A. Eckstein, K. N. Cassemiro, and C. Silberhorn, "Probing multimode squeezing with correlation functions," New J. Phys. **13**, 033027 (2011).

191. X. Lu, W. C. Jiang, J. Zhang, and Q. Lin, "Biphoton Statistics of Quantum Light Generated on a Silicon Chip," ACS Photonics **3**, 1626–1636 (2016).

192. Y. Zhou, F. Li, B. Bai, H. Chen, J. Liu, Z. Xu, and H. Zheng, "Superbunching pseudothermal light," Phys. Rev. A **95**, 053809 (2017).

193. V. Zwiller, I. E. Zadeh, J. W. N. Los, R. B. M. Gourgues, V. Steinmetz, S. M. Dobrovolskiy, and S. N. Dorenbos, "Single-photon detection with near unity efficiency, ultrahigh detection-rates, and ultra-high time resolution," in *Conference on Lasers and Electro-Optics (2017), Paper FF1E.1* (Optical Society of America, 2017), p. FF1E.1.

194. J. P. Allmaras, A. G. Kozorezov, B. A. Korzh, K. K. Berggren, and M. D. Shaw, "Intrinsic Timing Jitter and Latency in Superconducting Nanowire Single-photon Detectors," Phys. Rev. Appl. **11**, 034062 (2019).

195. M. A. Hall, J. B. Altepeter, and P. Kumar, "Drop-in compatible entanglement for optical-fiber networks," Opt. Express **17**, 14558–14566 (2009).

196. M. A. Hall, J. B. Altepeter, and P. Kumar, "All-optical switching of photonic entanglement," New J. Phys. **13**, 105004 (2011).

197. M. Lobino, G. D. Marshall, C. Xiong, A. S. Clark, D. Bonneau, C. M. Natarajan, M. G. Tanner, R. H. Hadfield, S. N. Dorenbos, T. Zijlstra, V. Zwiller, M. Marangoni, R. Ramponi, M. G. Thompson, B. J. Eggleton, and J. L. O'Brien, "Correlated photon-pair generation in a periodically poled MgO doped stoichiometric lithium tantalate reverse proton exchanged waveguide," Appl. Phys. Lett. **99**, 081110 (2011).

198. I. Choi, R. J. Young, and P. D. Townsend, "Quantum information to the home," New J. Phys. **13**, 063039 (2011).

199. P. Eraerds, N. Walenta, M. Legré, N. Gisin, and H. Zbinden, "Quantum key distribution and 1 Gbps data encryption over a single fibre," New J. Phys. **12**, 063027 (2010).

200. X. Li, P. L. Voss, J. E. Sharping, and P. Kumar, "Optical-Fiber Source of Polarization-Entangled Photons in the 1550 nm Telecom Band," Phys. Rev. Lett. **94**, 053601 (2005).

201. M. T. Liu and H. C. Lim, "Transmission of O-band wavelength-division-multiplexed heralded photons over a noise-corrupted optical fiber channel," Opt. Express **21**, 30358–30369 (2013).

202. H. de Riedmatten, I. Marcikic, W. Tittel, H. Zbinden, and N. Gisin, "Quantum interference with photon pairs created in spatially separated sources," Phys. Rev. A **67**, 022301 (2003).

203. O. Alibart, D. B. Ostrowsky, P. Baldi, and S. Tanzilli, "High-performance guided-wave asynchronous heralded single-photon source," Opt. Lett. **30**, 1539–1541 (2005).

204. T. Meany, L. A. Ngah, M. J. Collins, A. S. Clark, R. J. Williams, B. J. Eggleton, M. J. Steel, M. J. Withford, O. Alibart, and S. Tanzilli, "Hybrid photonic circuit for multiplexed heralded single photons," Laser Photonics Rev. **8**, L42–L46 (2014).

205. R. Aguinaldo, Y. Shen, and S. Mookherjea, "Large Dispersion of Silicon Directional Couplers Obtained via Wideband Microring Parametric Characterization," IEEE Photonics Technol. Lett. **24**, 1242–1244 (2012).

206. M. Savanier, C. Ozanam, L. Lanco, X. Lafosse, A. Andronico, I. Favero, S. Ducci, and G. Leo, "Near-infrared optical parametric oscillator in a III-V semiconductor waveguide," Appl. Phys. Lett. **103**, 261105 (2013).

207. C. Xiong, L. G. Helt, A. C. Judge, G. D. Marshall, M. J. Steel, J. E. Sipe, and B. J. Eggleton, "Quantum-correlated photon pair generation in chalcogenide As_2S_3 waveguides," Opt. Express **18**, 16206–16216 (2010).

208. P. Kok, W. J. Munro, K. Nemoto, T. C. Ralph, J. P. Dowling, and G. J. Milburn, "Linear optical quantum computing with photonic qubits," Rev. Mod. Phys. **79**, 135–174 (2007).

209. A. W. Elshaari, I. E. Zadeh, A. Fognini, M. E. Reimer, D. Dalacu, P. J. Poole, V. Zwiller, and K. D. Jöns, "On-chip single photon filtering and multiplexing in hybrid quantum photonic circuits," Nat. Commun. **8**, 1–8 (2017).

210. S. Paesani, Y. Ding, R. Santagati, L. Chakhmakhchyan, C. Vigliar, K. Rottwitt, L. K. Oxenløwe, J. Wang, M. G. Thompson, and A. Laing, "Generation and sampling of quantum states of light in a silicon chip," Nat. Phys. **15**, 925–929 (2019).

211. N. C. Harris, G. R. Steinbrecher, M. Prabhu, Y. Lahini, J. Mower, D. Bunandar, C. Chen, F. N. C. Wong, T. Baehr-Jones, M. Hochberg, S. Lloyd, and D. Englund, "Quantum transport simulations in a programmable nanophotonic processor," Nat. Photonics **11**, 447–452 (2017).

212. Y. Chen, J. Zhang, M. Zopf, K. Jung, Y. Zhang, R. Keil, F. Ding, and O. G. Schmidt, "Wavelength-tunable entangled photons from silicon-integrated III–V quantum dots," Nat. Commun. **7**, 1–7 (2016).

213. I. Aharonovich, C. Zhou, A. Stacey, J. Orwa, S. Castelletto, D. Simpson, A. D. Greentree, F. Treussart, J.-F. Roch, and S. Prawer, "Enhanced single-photon emission in the near infrared from a diamond color center," Phys. Rev. B **79**, 235316 (2009).

214. T. Horikiri and T. Kobayashi, "Decoy state quantum key distribution with a photon number resolved heralded single photon source," Phys. Rev. A **73**, 032331 (2006).

215. N. Montaut, L. Sansoni, E. Meyer-Scott, R. Ricken, V. Quiring, H. Herrmann, and C. Silberhorn, "High-Efficiency Plug-and-Play Source of Heralded Single Photons," Phys. Rev. Appl. **8**, (2017).

216. A. Yoshizawa, R. Kaji, and H. Tsuchida, "Generation of polarisation-entangled photon pairs at 1550 nm using two PPLN waveguides," Electron. Lett. **39**, 621–622 (2003).

217. P. Lodahl, "Quantum-dot based photonic quantum networks," Quantum Sci. Technol. **3**, 013001 (2018).

218. A. S. Rab, E. Polino, M. Valeri, P. Mataloni, N. Spagnolo, F. Sciarrino, S. Atzeni, S. Atzeni, G. Corrielli, G. Corrielli, A. Crespi, A. Crespi, R. Osellame, and R. Osellame, "Integrated source of entangled photon pair at telecom wavelength," in *Quantum Information and Measurement (QIM) V: Quantum Technologies (2019), Paper T5A.8* (Optical Society of America, 2019), p. T5A.8.

219. J. Chen, Z. H. Levine, J. Fan, and A. L. Migdall, "Frequency-bin entangled comb of photon pairs from a Silicon-on-Insulator micro-resonator," Opt. Express **19**, 1470–1483 (2011).

220. R. Kumar, J. R. Ong, J. Recchio, K. Srinivasan, and S. Mookherjea, "Spectrally multiplexed and tunable-wavelength photon pairs at 1.55 μm from a silicon coupled-resonator optical waveguide," Opt. Lett. **38**, 2969–2971 (2013).

221. Keysight, "Agilent 81480A, and Agilent 81680A, 81640A, 81682A, 81642A and 81689A User's Guide," https://www.keysight.com/upload/cmc_upload/All/tlsm0101.pdf.

222. Finisar, "Finisar Product Specification," https://www.finisar.com/sites/default/files/downloads/finisar_ftlx1672d3btl_10gbase-er_40km_sfp_optical_transceiver_product_specb1.pdf.

223. T. Hirooka, K. Kasai, Y. Wang, M. Nakazawa, M. Shiraiwa, Y. Awaji, and N. Wada, "First demonstration of digital coherent transmission in a deployed ROADM network with a 120 Gbit/s polarization-multiplexed 64 QAM signal," IEICE Electron. Express **12**, 20150884–20150884 (2015).

224. Q. Xu and M. Lipson, "Carrier-induced optical bistability in silicon ring resonators," Opt. Lett. **31**, 341–343 (2006).

225. S. Abdollahi and M. K. Moravvej-Farshi, "Effects of heat induced by two-photon absorption and free-carrier absorption in silicon-on-insulator nanowaveguides operating as all-optical wavelength converters," Appl. Opt. **48**, 2505–2514 (2009).

226. H. K. Tsang, C. S. Wong, T. K. Liang, I. E. Day, S. W. Roberts, A. Harpin, J. Drake, and M. Asghari, "Optical dispersion, two-photon absorption and self-phase modulation in silicon waveguides at 1.5 μm wavelength," Appl. Phys. Lett. **80**, 416–418 (2002).

227. X. Lu, Q. Li, D. A. Westly, G. Moille, A. Singh, V. Anant, and K. Srinivasan, "Chip-integrated visible–telecom entangled photon pair source for quantum communication," Nat. Phys. **15**, 373–381 (2019).

228. R. R. Kumar, M. Raevskaia, V. Pogoretskii, Y. Jiao, and H. K. Tsang, "Entangled photon pair generation from an InP membrane micro-ring resonator," Appl. Phys. Lett. **114**, 021104 (2019).

229. C. Ma, X. Wang, and S. Mookherjea, "Photon-pair and heralded single photon generation initiated by a fraction of a 10 Gbps data stream," Opt. Express **26**, 22904–22915 (2018).

230. A. Tanaka, M. Fujiwara, S. W. Nam, Y. Nambu, S. Takahashi, W. Maeda, K. Yoshino, S. Miki, B. Baek, Z. Wang, A. Tajima, M. Sasaki, and A. Tomita, "Ultra fast quantum key distribution over a 97 km installed telecom fiber with wavelength division multiplexing clock synchronization," Opt. Express **16**, 11354–11360 (2008).

231. S. Mookherjea and H. R. Grant, "High dynamic range microscope infrared imaging of silicon nanophotonic devices," Opt. Lett. **37**, 4705–4707 (2012).

232. J. Wang, Z. Yao, T. Lei, and A. W. Poon, "Silicon coupled-resonator optical-waveguide-based biosensors using light-scattering pattern recognition with pixelized mode-field-intensity distributions," Sci. Rep. **4**, 1–9 (2014).